Novel Astrophysical Constraints on Black Holes

Novel Astrophysical Constraints on Black Holes

A dissertation presented
by
Pierre Christian
to
The Department of Astronomy

in partial fulfillment of the requirements
for the degree of
Doctor of Philosophy
in the subject of
Astronomy and Astrophysics

Harvard University
Cambridge, Massachusetts
May 2018

Dissertation Advisor: Abraham Loeb Pierre Christian

Novel Astrophysical Constraints on Black Holes

Abstract

While black holes have captured both the public and scientific interest, they are still counted amongst the most mysterious objects in the Universe. In this dissertation, we study these objects from an astrophysical perspective. Black holes are active players in the astrophysical stage. They reshape their environments through the strength of their gravity, and their immense radiation is important even at cosmological distances. The first part of this dissertation is a study of the interplay between the supermassive black hole at the center of the Milky Way Galaxy and matter at the Galactic Center. We propose several astronomical observations that could detect the effects of this central black hole on its surrounding. As black holes are remarkable natural laboratories for gravitational physics, the second part of this dissertation focuses on leveraging astrophysical observables to test the validity of our current understanding of gravity. We study the repercussions of modifying general relativity on the astrophysical signals of both the plasma in the black hole accretion disk and stars in orbit around the black hole. The results of such tests will help determine the next steps in our pursuit for a theory of quantum gravity. Finally, the nascent field of

gravitational waves astrophysics allows black holes to be studied in a novel way. The last part of this dissertation is concerned with using gravitational wave observables to study the population distribution of black holes. By utilizing data collected by gravitational wave observatories instead of conventional telescopes, we show that questions on the formation and evolution of black holes that were previously untenable can now be addressed. At the end of this dissertation, we will also discuss the possibility of observing the gravitational lensing of gravitational waves.

Contents

To those who look to the skies

Listing of figures

Acknowledgments

I would like to thank...

My advisor, Avi Loeb, from whom I learned a great deal about science and life. Of all his lessons, Avi taught me two that I consider most important: to question everything and to stand up for what I believe, even if it goes against conventional wisdom.

My other collaborators: Philip Mocz, Dimitrios Psaltis, and Salvatore Vitale, without whom this thesis would be impossible to write.

Josh Grindlay, for serving as the chair of my thesis committee and for the various conversations (scientific or otherwise) that we have shared throughout my years as a graduate student.

The other members of said committee: Shep Doeleman, Mark Reid, and before his sabbatical, Ramesh Narayan. A special thanks is reserved for my external committee member, Salvatore Vitale, who made the arduous trek from the Massachusetts Institute of Technology to attend my thesis defense at Harvard.

Ramesh Narayan for the many interesting conversations on black holes and relativity, as well as for the wonderful experience of being his teaching assistant for his class on radiative processes.

Karin Oberg, with whom I have enjoyed two semesters of teaching at Harvard.

My friends and classmates, especially the entering class of 2012 at the Harvard Astronomy Department. Many laughs and not as many tears were shared between us. A special mention goes to Philip Mocz, whom I first met when we were undergrads at prospective visits. We were classmates for 5 years, housemates for 4 of those years, and finally collaborate on a paper together.

And my family, who made me who I am, and to whom I owe everything.

The following authors contributed to Chapter 2: Abraham Loeb

The following authors contributed to Chapter 3: Abraham Loeb

The following authors contributed to Chapter 4: Abraham Loeb

The following authors contributed to Chapter 6: Dimitrios Psaltis, Abraham Loeb

The following authors contributed to Chapter 8: Abraham Loeb

The following authors contributed to Chapter 9: Philip Mocz, Abraham Loeb

The following authors contributed to Chapter 10: Salvatore Vitale, Abraham Loeb

1

Introduction

While black holes have captured both the public and scientific interest, they are still counted amongst the most mysterious objects in the Universe. In this dissertation, we seek to study these objects from an astrophysical perspective.

First, black holes are active players in the astrophysical stage. They reshape their environments through the strength of their gravity, and their immense radiation is

important even at cosmological distances.The first part of this dissertation is a study of the interplay between the supermassive black hole at the center of the Milky Way Galaxy and matter at the Galactic Center. We propose several astronomical observations that could detect the effects of this central black hole on its surrounding.

As black holes are remarkable natural laboratories for gravitational physics, the second part of this dissertation focuses on leveraging astrophysical observables to test the validity of our current understanding of gravity. We study the repercussions of modifying General Relativity on the astrophysical signals of both the plasma in the black hole accretion disk and stars in orbit around the black hole. The results of such tests will help determine the next steps in our pursuit for a theory of quantum gravity.

Finally, the nascent field of gravitational waves astrophysics allows black holes to be studied in a novel way. The last part of this dissertation is concerned with using gravitational wave observables to study the population distribution of black holes. By utilizing data collected by gravitational wave observatories instead of conventional telescopes, we show that questions on the formation and evolution of black holes that were previously untenable can now be addressed. Further, we discuss the possibility of observing the gravitational lensing of gravitational radiation.

In this chapter, we introduce black holes as they are understood in astrophysics. First, we present the Kerr spacetime of General Relativity (GR), and summarize its most relevant features. We then proceed with an outline for the rest of this disser-

tation. In this chapter we use geometrized units where $G = c = 1$, and our metric signature is $(-,+,+,+)$.

1.1 Introduction to astrophysical black holes

Black holes are solutions to the equations of a theory of gravitation endowed with an event horizon. Currently, the most successful theory of gravitation is the Einstein Field Equations* of GR,

$$G_{\mu\nu} = 8\pi T_{\mu\nu} \,, \tag{1.1}$$

where $G_{\mu\nu}$ is the Einstein tensor and $T_{\mu\nu}$ is the stress energy tensor. The Einstein tensor is defined as

$$G_{\mu\nu} \equiv R_{\mu\nu} - \frac{1}{2} g_{\mu\nu} R \,, \tag{1.2}$$

where the Ricci tensor $R_{\mu\nu}$ is defined as a particular contraction of the Riemann curvature tensor $R^{\alpha}{}_{\beta\gamma\delta}$ given by

$$R_{\mu\nu} \equiv R^{\alpha}{}_{\mu\alpha\nu} \,, \tag{1.3}$$

$g_{\mu\nu}$ the metric tensor, and $R \equiv g^{\mu\nu} R_{\mu\nu}$ is the Ricci scalar. While the most famous black hole solution of the Einstein Field Equation is the spherically symmetric vacuum solution known as the Schwarzschild metric, whose line element in Schwarzschild

*Throughout this dissertation, we will suppress the existence of the cosmological constant.

coordinates (t, r, θ, ϕ) is given by (Schwarzschild 1916)

$$ds^2 = -(1-2M)dt^2 + (1-2M)^{-1}dr^2 + r^2 d\Omega \,, \tag{1.4}$$

where M is the mass of the black hole, and $d\Omega$ is the round metric on S^2, the Schwarzschild metric is woefully inadequate to model astrophysical black holes.

Astrophysical black holes, formed either through the natural progression of the life cycle of massive stars (Oppenheimer & Snyder 1939) or through a direct collapse of dense gas (Haehnelt & Rees 1993; Umemura et al. 1993; Loeb & Rasio 1994; Eisenstein & Loeb 1995; Bromm & Loeb 2003; Begelman et al. 2006), would naturally possess angular momentum as a result of their formation mechanisms. Further, black holes in binaries or at the center of galaxies could obtain angular momentum through mergers or accretion of gaseous materials. Because the Schwarzschild black hole is a static solution possessing no angular momentum, it is incapable of capturing the astrophysics of realistic black holes.

The next section of this chapter introduces the Kerr metric (Kerr 1963), which is a vacuum solution of the Einstein Field Equations describing a rotating black hole. Due to its angular momentum parameter, the Kerr metric can more accurately capture the physics of an astrophysical black hole than the Schwarzschild metric. The Kerr metric is at the heart of a variety of astrophysical models, including models of emissions around galactic centers (Yuan & Narayan 2014), tidal disruption flares (e.g. Leloudas

et al. 2016), and X-ray binaries (Shakura & Sunyaev 1973; Davis et al. 2006). Recently, the Kerr black hole has also been shown to accurately model the end result of binary black hole mergers (Pretorius 2005).

A generalization of the Kerr metric allowing the presence of nonzero electric or magnetic charge is known as the Kerr-Newman metric (Newman & Janis 1965; Newman et al. 1965). While the physical properties of the Kerr-Newman metric is interesting in its own right, the electromagnetic charge of an astrophysical black hole is expected to be miniscule. This is because an astrophysical black hole is expected to be surrounded by ionized gas. If the black hole develops a nonzero charge, it will quickly neutralize itself by accreting the opposite charge from its surrounding.

1.2 The Kerr metric

The Kerr metric for an uncharged, rotating black hole, given in Boyer-Lindquist coordinates (t, r, θ, ϕ) as (Kerr 1963; Chandrasekhar 1983)

$$ds^2 = -\left(1 - \frac{2Mr}{\Sigma}\right) dt^2 - \frac{4Mar\sin^2\theta}{\Sigma} dt d\phi + \frac{\Sigma}{\Delta} dr^2 + \Sigma d\theta^2 + \left(r^2 + a^2 + \frac{2Ma^2 r \sin^2\theta}{\Sigma}\right) \sin^2\theta d\phi^2 \,, \tag{1.5}$$

where $G = c = 1$, $a = J/M$, $\Sigma = r^2 + a^2\cos^2\theta$, $\Delta = r^2 - 2Mr + a^2$, and we have taken the $(-,+,+,+)$ as the metric signature. M is the mass of the black hole, and a is the

spin of the black hole defined as

$$a = \frac{J}{M} \,, \tag{1.6}$$

where J is the angular momentum of the black hole. In the units where $G = c = 1$, a has the dimensions of mass. Note that when $a = 0$, equation (1.5) reduces to the line element for a Schwarzschild black hole.

1.3 Asymptotic flatness and symmetries of the Kerr black hole

The Kerr black hole is an asymptotically flat, stationary, axisymmetric solution of the Einstein Field Equations (Chandrasekhar 1983). Asymptotic flatness means that far from the black hole, the Kerr geometry approaches the geometry of Minkowski spacetime. To demonstrate this property of the Kerr metric, we make an expansion of equation (1.5) with r/M and r/a as a small parameter,

$$ds^2 = -\left(1 - \frac{2M}{r}\right) dt^2 + \left(1 + \frac{2M}{r}\right) dr^2 + r^2 d\Omega - \frac{4Ma}{r^2} \sin^2\theta (r d\phi) dt + \dots \,, \tag{1.7}$$

where $d\Omega$ is the round metric on S^2. From this form, it is easily seen that as $r \to \infty$, the Kerr metric reduces to flat spacetime.

A metric is stationary if it possesses an asymptotically timelike Killing vector. For

the Kerr metric in Boyer-Lindquist coordinates, it is obvious that

$$\xi^{\nu} = (1, 0, 0, 0) \ , \tag{1.8}$$

is a Killing vector, as the metric is independent of t. Similarly, the existence of the axisymmetric spacelike Killing vector

$$\eta^{\nu} = (0, 0, 0, 1) \ , \tag{1.9}$$

is obvious in Boyer-Lindquist coordinates. These two Killing vectors generate conserved quantities in the orbits of test particles in the Kerr spacetime. For a particle with four-velocity u^{ν}, the stationary nature of the Kerr metric enforced the conservation of energy,

$$e \equiv -\xi^{\nu} u_{\nu} \quad \text{(Conservation of Energy)} \ , \tag{1.10}$$

while the axisymmetric property generates the conservation of angular momentum,

$$l \equiv \eta^{\nu} u_{\nu} \quad \text{(Conservation of Angular Momentum)} \ , \tag{1.11}$$

The Kerr metric possesses another symmetry generated by the Killing tensor

$$K^{\mu\nu} = 2\Sigma l^{(\mu} n^{\nu)} + r^2 g^{\mu\nu} \ , \tag{1.12}$$

where the brackets $(\ldots)$ in the indices indicate symmetrization, and l^ν and n^ν are the principal null vectors

$$l^\nu = \left(\frac{r^2+a^2}{\Delta}, 1, 0, \frac{a}{\Delta}\right) , \tag{1.13}$$

$$n^\nu = \left(\frac{r^2+a^2}{2\Sigma}, -\frac{\Delta}{2\Sigma}, 0, \frac{a}{2\Sigma}\right) . \tag{1.14}$$

With these definitions, one could verify that $K^{\mu\nu}$ satisfies $\nabla_{(\alpha}K_{\beta\gamma)} = 0$, and thus is a Killing tensor. Projecting the Killing tensor to the four-velocity of a test particle produces the conserved quantity,

$$C = K^{\mu\nu}u_\mu u_\nu , \tag{1.15}$$

known as the Carter's constant (Carter 1968).

Aside from the symmetries associated with ξ^ν (stationary), η^ν (axisymmetry), and $K^{\mu\nu}$ (the 'hidden' symmetry generating the Carter's constant), the last important symmetry in the Kerr metric is the discrete reflection symmetry in the equatorial plane $\theta = \pi/2$. This last symmetry can be easily deduced through an inspection of the line element, equation (1.5).

1.4 Important surfaces and regions of the Kerr black hole

The Kerr metric in Boyer-Lindquist coordinates is endowed with two coordinate singularities, known as the outer and inner horizons at

$$r_{\pm} = M \pm \sqrt{M^2 - a^2} \, . \tag{1.16}$$

As one approaches these surfaces, $\Delta \to 0$, and the metric components in Boyer-Lindquist coordinates becomes singular. However, at these surfaces, the contraction of the Riemann curvature tensor, $R_{\alpha\beta\gamma\delta}R^{\alpha\beta\gamma\delta}$ remains finite[†]. The outer event horizon, r_+ is the event horizon, defined as the boundary of the causal past of future null infinity. Setting $a = 0$, one recovers the Schwarzschild event horizon $r_+(a = 0) = R_S = 2M$. The inner horizon is also the Cauchy horizon for the Kerr metric, and thus initial data cannot be evolved past it (Hawking & Ellis 1973).

At $r = 0$, $\theta = \pi/2$, the quantity ρ becomes zero, and there is another singularity in the Kerr metric. This ring singularity is a curvature singularity in the sense that $R_{\alpha\beta\gamma\delta}R^{\alpha\beta\gamma\delta} \to \infty$. Unlike the coordinate singularities at $r_{\pm}$, it is impossible to remove this singularity through a change of coordinates.

Due to the rotation of the black hole, there are locations in the spacetime in which it is impossible to be unmoving. That is, there are locations in the Kerr spacetime in

[†]This quantity is known as the Kretschmann scalar.

which the trajectory given by

$$q^{\nu}(\tau) = (t(\tau), r(\tau), \theta(\tau), \phi(\tau)) = (\tau, r_0, \theta_0, \phi_0) \ , \tag{1.17}$$

where (r_0, θ_0, ϕ_0) are constants is impossible. This is because the four-velocity vector of such trajectories, given by $dq^{\nu}(t)/d\tau = (1, 0, 0, 0)$ must satisfy the timelike condition,

$$g_{\mu\nu} \frac{\mathrm{d}q^{\nu}(\tau)}{\mathrm{d}\tau} \frac{\mathrm{d}q^{\nu}(\tau)}{\mathrm{d}\tau} = g_{tt} < 0 \ . \tag{1.18}$$

However, solving the equation

$$g_{tt} = -\left(1 - \frac{2Mr}{\Sigma}\right) = 0 \ , \tag{1.19}$$

one can show that g_{tt} actually becomes positive when

$$r_E^- < r < r_E^+ \ , \tag{1.20}$$

where

$$r_E^{\pm} \equiv m \pm \sqrt{m^2 - a^2 \cos^2 \theta} \ . \tag{1.21}$$

In this region, the trajectory given by equation (1.17) is not timelike, and is thus impossible. Crucially,

$$r_+ \leq r_E^+ \ , \tag{1.22}$$

and thus the region where one cannot be unmoving extends beyond the event horizon. The region $r_+ \leq r \leq r_E^+$ is known as the ergosphere, and from these regions energy could be extracted from the black hole to power astrophysical processes (Penrose 1969; Blandford & Znajek 1977).

1.5 Black holes and their interactions with their environments

Black holes do not exist in vacuo. They are embedded in astrophysical environments resulting from both their formation processes and subsequent migrations. Further, as exemplified by the energy extraction from a black hole through its ergosphere, black holes and their environments interact with each other. The first part of this dissertation is concerned with the study of black holes within this astrophysical context.

Chapter 2 is focused on the effect of Sgr A* on the phase-space distribution of stars around it, and how this effect can be detected in signals from Galactic Center (GC) pulsars. The gravitational field of Sgr A* affects a pulsar's signal directly due to the Doppler shifts induced by its orbital motion. It also affects the pulsar indirectly, through perturbing the motion of stars in the the star cluster at the GC. We computed that by monitoring a ∼few millisecond pulsars at the GC, one can constraint the total mass enclosed in the pulsars' orbits. If ∼tens of millisecond pulsars are found, one can also constraint the GC mass function.

Chapter 3 proposed that a disk of neutral gas might exist around the supermassive

black hole, and that they could produce absorption features in the black hole's emission spectrum. We showed that this disk can be detected as absorption features in 21-cm spectroscopic observations of the GC, even if it is spatially unresolved. Further, these observations will be able to discern the disk's parameters, such as inclination angle, optical depth, temperature, and existence of gaps in the disk.

1.6 Astrophysical constraints on strong gravity and black hole spacetime parameters

The second part of this dissertation is concerned with astrophysical constraints that could be placed close to a black hole. In Chapter 4 we studied how one can leverage the orbits and expansions of plasma ejectas from black holes to map spacetime parameters. We computed the orbital velocities and expansion rates of ejected plasma blobs close to Sgr A* and M87, which could be compared with observations from the Event Horizon Telescope (EHT). If the alignment of the ejected blob is favorable, one could even use them to probe beyond-GR strong gravity effects.

The next couple of chapters is on testing the no-hair theorem of GR in an astrophysical context. The no-hair theorem states that isolated, stationary black holes in GR are described by only three parameters: M, the mass of the black hole; J, the spin of the black hole; and Q, the charge of the black hole (Israel 1967, 1968; Carter 1971; Hawking 1972; Robinson 1975). In addition to GR, in the derivation of this theorem,

it is necessary to also add the conditions that singularities are hidden beneath the black hole horizon and that closed time-like loops allowing time travel into the past are non-existent (Johannsen 2013). If an astrophysical black hole is observed to violate the no-hair theorem, it will imply that either GR or the other two assumptions are incorrect. The violation of any of these assumptions carry weighty repercussion to both fundamental physics and philosophy, and as such testing these assumptions are both important and of wide interest.

Chapter 5 focused on testing GR by studying the magnetic field configuration around black holes that violate the no-hair theorem. A Kerr black hole can be turned into a no-hair violating black hole by adding an extra quadrupole moment on the spacetime (Johannsen 2013), and in this chapter we computed the effect of this modification on magnetic fields around the black hole. We showed that the magnetic field is distorted in such a way that they also exhibit an extra quadrupolar pattern, and that the distortion could be large close to the black hole horizon.

Chapter 6 is concerned with computing the signal of pulsars orbiting a no-hair theorem violating black hole. This chapter showed that an extra time delay analogous to the classical Shapiro delay is imposed on the pulsar signal due to this modification. For pulsars orbiting Sgr A*, this signal is at the level of ~ 0.01 seconds, which is detectable if the pulsar is of the millisecond variety.

1.7 Studying black holes through gravitational waves

The nascent field of gravitational wave physics allows a new avenue for the study of black holes. In addition to various tests of GR, gravitational wave observables could also be used to study the formation and population of black holes. This is because gravitational wave observatories allow for the detection of binary black holes. While a significant amount of black holes are thought to be in such systems, they are impossible to detect using conventional telescopes because they produce little to no electromagnetic radiation. The final part of this dissertation is on utilizing gravitational waves to study the black holes that produce them and the cosmos that they traverse.

The biggest puzzle of the recent Laser Interferometer Gravitational-Wave Observatory (LIGO) detections are the extreme masses of the detected black holes. While previously known stellar mass black holes possess masses of at most 10 Solar Masses, some of the black holes in the LIGO binaries exceed that by a factor of 3 (Abbott et al. 2016b,a, 2017b,d,c). This tension generated a large amount of interest as most binary black hole formation scenarios would require these black holes to be born out of stars with masses in excess of 100 Solar Masses. If conventional stellar mass distributions are assumed, these supermassive stars should be exceedingly rare. This is compounded with the fact that there are multiple competing formation mechanisms.

In Chapter 8, we used the LIGO detections to constrain the population of stellar mass binary black holes in the Milky Way Galaxy that can potentially be LISA

sources. Assuming that binary black holes possess orbits that continually harden due to emission of gravitational radiation, we computed the number of Galactic binary black holes as a function of semimajor axis. This calculation allows a constraint of the total number of binary black holes and gravitational wave rate that is independent of population synthesis models to be formulated. Our calculation predicted that there is ~ 1 Galactic binary black hole in the LISA range.

In Chapter 9 we calculated the impact of BH mergers on the BH mass function. In particular, supernova theory predicts the existence of a mass gap in the BH mass function between masses of $M \sim 50M_{\odot}$ to $M \sim 130M_{\odot}$[‡] because the would-be stellar progenitors undergo pair-instability supernovae (Woosley 2017). We investigated how this gap could be filled by mergers of BHs in dynamical star clusters.

Finally, Chapter 10 is on the gravitational lensing of gravitational waves. In this chapter, we showed that the modification to a gravitational radiation waveform as it travels through a gravitational potential is potentially observable by ground-based observatories. The gravitational lensing of light has seen widespread use in astronomy, and the detection of the analogous phenomena for gravitational radiation will open a new way to observe the cosmos.

[‡]These numbers are for stars in close binaries. For stars in globular clusters, the lower bound of the gap might increase by a few tenths of Solar masses.

2

Pulsar timing constraints on masses in the Galactic Center

We consider the time derivatives of the period P of pulsars at the Galactic Center due to variations in their orbital Doppler shifts. We show that in conjunction with a measurement of a pulsar's proper motion and its projected separation from the super-

massive black hole, Sgr A*, measuring two of the three derivatives $\dot{P}$, $\ddot{P}$, or $\dddot{P}$ sets a constraint that allows for the recovery of the complete six phase space coordinates of the pulsar's orbit, as well as the enclosed mass within the orbit. Thus, one can use multiple pulsars at different distances from Sgr A* to determine the radial mass distribution of stars and stellar remnants at the Galactic center. Furthermore, we consider the effect of passing stars on the pulsar's period derivatives and show how it can be exploited to measure the characteristic stellar mass in the Galactic Center.

2.1 Introduction

The recent discovery of J1745-2900, a magnetar orbiting the supermassive black hole Sgr A* at a projected separation of 0.09 pc (Mori et al. 2013; Rea et al. 2013; Kennea et al. 2013) stimulated much interest in its timing and astrometry. Pulsars close to Sgr A* could allow for a precise measurement of the black hole's mass and spin, in addition to a host of relativistic effects (Pfahl & Loeb 2004; Cordes et al. 2004; Kramer et al. 2004; Psaltis & Johannsen 2011; Liu et al. 2012).

Unfortunately, the timing of the magnetar J1745-2900 is not sufficiently stable for dynamical measurements (Kaspi et al. 2014). Furthermore, it is located too far from Sgr A* (with a Keplerian orbital period of $\sim$ 500 years) for it to be useful as a probe of strong field gravity. Calculations imply that there could be $\sim$ 200 pulsars within a parsec from Sgr A* (Chennamangalam & Lorimer 2014), although perhaps only $\sim$ 20

of them being bright enough to be detected (Dexter & O'Leary 2014). Most of these pulsars might also be located too far from Sgr A* for testing strong field gravity.

Nevertheless, one can still use pulsars at these larger distances to probe the astrophysical environment of the Galactic Center. In particular, the orbital dynamics of a pulsar is determined by the mass distribution within its orbit. Therefore, by measuring the imprint of the orbital Doppler effect on the pulsar's period, P, one should be able to constrain the radial mass profile of stars and stellar remnants around Sgr A*. A previous study (Chanamé & Gould 2002) considered this possibility, but neglected the contributions of closely passing stars. In this letter, we evaluate the limitations of this technique due to this extra source of uncertainty, and also show that one can constrain the characteristic stellar mass in this environment by measuring the third time derivative of the pulsar's period, $\dddot{P}$.

This paper is organized as follows. In §2.2 we discuss the orbital contribution to the first, second, and third period derivatives $\dot{P}$, $\ddot{P}$, and $\dddot{P}$ by the mean field, and discuss how it can be used to measure the mass enclosed within the pulsar's orbit. In §2.3 we calculate the effects of passing stars on the period derivatives, and how it could be used to constrain the characteristic stellar mass in the Galactic Center. Finally in §2.4 we offer some concluding remarks.

2.2 Measuring the enclosed mass via the mean field contribution to period derivatives

We begin with the equation for classical Doppler shift relating the observed period P_O to the intrinsic (rest frame) period P_i:

$$P_O = P_i(1 - \vec{\beta} \cdot \vec{n}) \ , \tag{2.1}$$

where $\vec{\beta}$ is the velocity of the pulsar in units of c, and $\hat{n}$ is the unit vector pointing from the pulsar to the observer (see Figure 2.1 for geometry). In general, pulsar timing measurements are done with respect to the solar system barycenter. However, since the motion of the solar system barycenter is well constrained (Reid et al. 1999), in writing equation (2.1) we shifted to the frame where the observer is at rest with respect to the black hole. This could be done by the substitution $P \rightarrow P(1 - \vec{\beta}_{ss} \cdot \hat{n})$, where $\vec{\beta}_{ss}$ is the velocity of the solar system barycenter in units of c. Since both $\vec{\beta}$ and $\hat{n}$ changes with time, the orbit of the pulsar induces nonzero time derivatives on P_O. Since the orbital time is much longer than the observation time, we can use a Taylor expansion in time t to write,

$$P_O(t) = P_O(0) + \dot{P}_O(0)t + \frac{1}{2}\ddot{P}_O(0)t^2 + \frac{1}{6}\dddot{P}_O(0)t^3 + ... \ . \tag{2.2}$$

The first two derivatives have been previously studied in the context of globular clusters (Phinney 1993). In this section we provide a treatment of $\dot{P}$, $\ddot{P}$, and $\dddot{P}$ for pulsars at the Galactic Center. In general, these time derivatives depend on the pulsar's 6 position and velocity phase space coordinates, as well as the enclosed mass. While throughout this paper we focus on the period derivatives themselves, we note that they are not the observables in pulsar timing measurements. Rather, timing measurements measure the frequency, $\nu = 1/P$, and its derivatives (Lorimer & Kramer 2004). The period derivatives depend not only on the frequency derivative of the same order, but on all successive frequency derivatives up to that order.

Direct imaging (e.g. Rea et al. 2013) yields the projected separation of the pulsar from Sgr A*. The proper motions of pulsars have been measured previously both in the context of quantifying the pulsar's natal kick (e.g. Kaplan et al. 2008) and for astrometric purposes (e.g. Du et al. 2014). In particular, the proper motion of J1745-2900 is currently being measured (Bower et al. 2014a).

Line of sight distances to pulsars can be obtained via parallax (see Du et al. 2014 for an example of the technique applied to a millisecond pulsar not at the Galactic Center), and progress has been made to measure the parallaxes of pulsars at large distances (up to 7.2 kpc) using very-long-baseline interferometers (Chatterjee et al. 2009). The recently launched GAIA satellite* is also expected to further improve the prospect of measuring pulsar parallaxes for pulsars with sufficiently bright optical

*http://sci.esa.int/gaia/

companions. Further, for millisecond pulsars with high timing precision, timing analysis can also determine line of sight distances (Verbiest et al. 2008).

In addition, the distance to pulsars can be estimated from their pulse dispersion measure. The delay in pulse arrival time as a function of frequency, along with a model of the free electron distribution (e.g. the NE2001 model of Cordes & Lazio 2002, 2003), can be used to estimate distances. This method was recently applied to the Galactic Center for the magnetar J1745-2900 (Eatough et al. 2013a; Shannon & Johnston 2013). However, we note that the accuracy of the pulse dispersion measure distances depends strongly on knowledge of the free electron distribution. The electron distribution at the Galactic center is highly unconstrained, and thus the distance measured might not be reliable enough for our purposes.

Based on the above measurements, one can determine 5 out of 6 of the pulsar's phase space coordinates. Another constraint can be placed via a measurement of one of the period derivatives, thereby constituting a full determination of its 6 phase space coordinates. Furthermore, we will show that with the measurement of another period derivative, one could directly measure the mass enclosed.

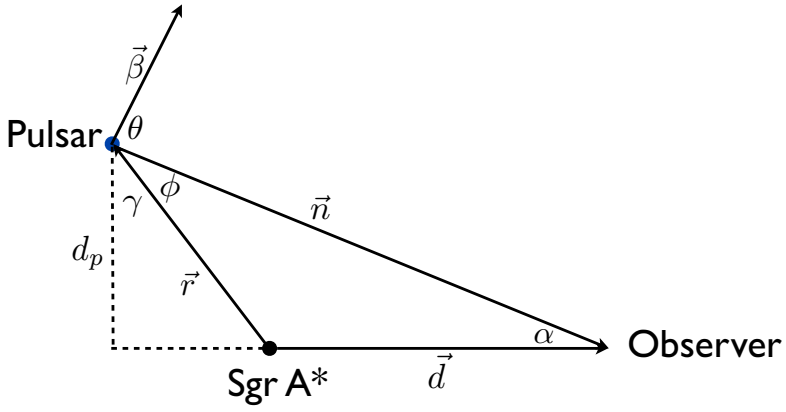

Figure 2.1: The geometry under consideration. Note that the pulsar's velocity vector (in units of c), $\vec{\beta}$, is not constrained to lie in the pulsar-Sgr A*-observer plane.

2.2.1 The first period derivative

The first time derivative of the pulsar's period P is given by:

$$\dot{P}_O = -P_i \frac{\partial \vec{\beta} \cdot \vec{n}}{\partial t} = P_i \left(\beta \sin\theta \frac{\partial \theta}{\partial t} - \vec{n} \cdot \frac{\partial \vec{\beta}}{\partial t} \right) , \tag{2.3}$$

where $\beta \equiv |\vec{\beta}|$ the subscript O denotes the orbital contribution to $\dot{P}$, in difference from the intrinsic pulsar spindown, $\dot{P}_i$. The acceleration of the pulsar is given by:

$$\frac{\partial \vec{\beta}}{\partial t} = -\frac{GM}{r^2 c} \hat{r} , \tag{2.4}$$

where $M(r) \equiv M_{BH} + M_\star(r)$ is the total mass, namely the mass of the supermassive black hole Sgr A*, $M_{BH} = (4.31 \pm 0.36) \times 10^6 M_\odot$ (Gillessen et al. 2009; Ghez

et al. 2008), plus the mass of the stars within the pulsar's orbit. Substituting this into equation (2.3) gives:

$$\frac{\dot{P}_O}{P_i} = \beta \sin\theta \frac{\partial\theta}{\partial t} + \frac{GM}{r^2 c}(\vec{n}\cdot\hat{r}) = \beta \sin\theta \frac{\partial\theta}{\partial t} - \frac{GM}{r^2 c}\cos\phi \ , \tag{2.5}$$

where ϕ is the angle between the pulsar's radius vector $\vec{r}$ and $\vec{n}$. The negative sign arises from the direction of $\hat{r}$. Noting that

$$\frac{\partial\theta}{\partial t} = \frac{c\beta}{d}\sin\theta \ , \tag{2.6}$$

where $\vec{d}$ is the displacement of the solar system barycenter from the supermassive black hole Sgr A*, we obtain

$$\frac{\dot{P}_O}{P_i} = \frac{c\beta_\perp^2}{d} - \frac{GM}{r^2 c}\cos\phi = \frac{c\beta_\perp^2}{d} - \frac{GM}{d_p^2 c}\sin^2\phi\cos\phi \ , \tag{2.7}$$

where $\beta_\perp$ is the transverse component of β and we have used the definition of the projected distance: $d_p \equiv r\cos\gamma \approx r\sin\phi$ in the second equality. Solving for ϕ, we obtain:

$$\frac{\sin^2\phi}{d_p^2}\cos\phi = \frac{c}{GM}\left[\frac{c\beta_\perp^2}{d} - \frac{\dot{P}_O}{P_i}\right] \ . \tag{2.8}$$

Defining r_l as the component of $\vec{r}$ in the line of sight direction:

$$\frac{r_l}{r^3} = \frac{c}{GM}\left[\frac{c\beta_\perp^2}{d} - \frac{\dot{P}_O}{P_i}\right] . \tag{2.9}$$

Note that in addition to the spindown rate due to the orbital Doppler effect, a portion of the observed $\dot{P}$ is due to intrinsic radiative losses. The overall spindown rate is the sum of the intrinsic $\dot{P}_i$ and the orbital $\dot{P}_O$ components. Given this perspective, we view equation (2.9) as providing $\dot{P}_O$ as a function of $M(r)$ and the pulsar's phase space position: $\dot{P}_O(r, d_p, \beta, M)$. For a specific $\beta_\perp$, the value of $\dot{P}_O$ is bounded from above. For example, consider the magnetar J1745-2900 with an observed spindown rate of $\dot{P}_{obs}/P_i = 1.73 \times 10^{-12}$ s^{-1} and $d_p = 0.09$ pc (Mori et al. 2013). Approximating $M \approx M_{BH}$ and $c\beta_\perp \sim 150$ km s^{-1}, we find that equation (2.9) obtains a maximum at $\dot{P}_O/P_i \sim 10^{-13}$ s^{-1}. This means that the orbital contribution to $\dot{P}$ can account for at most $\sim 17\%$ of the observed $\dot{P}$ (assuming the observed $\dot{P}_{obs}$ value of Mori et al. 2013). In this context, we can therefore be certain that measurements of the magnetar's magnetic field strength is not contaminated significantly by the orbital component $\dot{P}_O$.

If there is a way to measure $\dot{P}_O$ on its own (e.g. if the magnetic field of the pulsar is small, and the orbital contribution dominates), or in the case of millisecond pulsars, where $\dot{P}_O$ dominates $\dot{P}_{obs}$, equation (2.9) provides a new constraint to the pulsar's

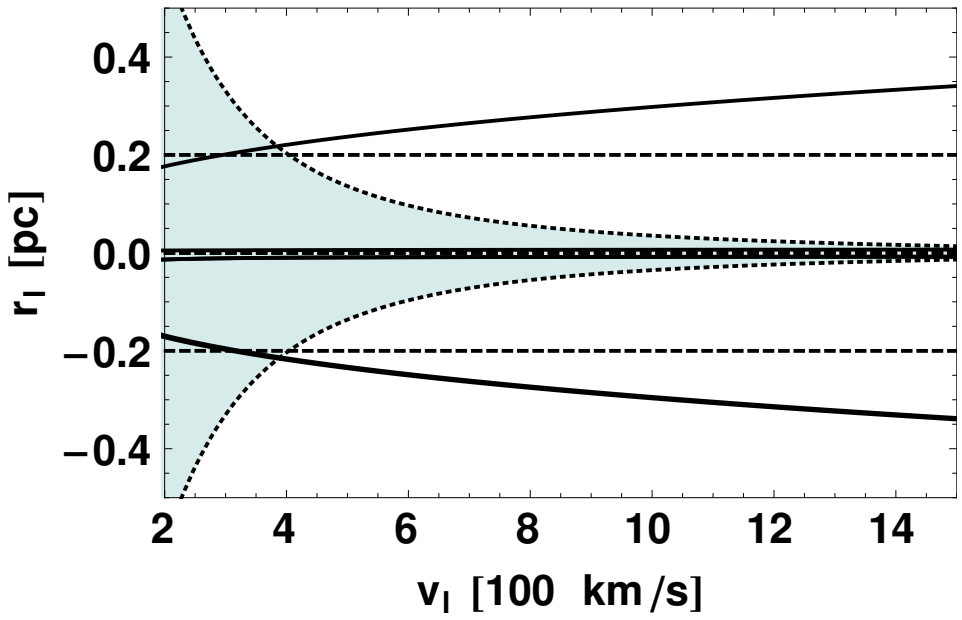

Figure 2.2: Constraints on the line-of-sight componet of the pulsar's orbital radius r_l and velocity v_l based on $\dot{P}$ (dashed lines) and $\ddot{P}$ (solid lines) for a case where the pulsar is orbiting in the Sgr A*-observer plane with $\dot{P} = 5 \times 10^{-15}$, $\ddot{P} = 10^{-24}$ s^{-1}, $d_p = 0.01$ pc, and $v_\perp = 150$ km s^{-1}. Orbits in the shaded region are gravitationally bound to Sgr A*. The pulsar's period P_O is taken to be 1 second.

phase space position. For example, if it is observed that:

$$\frac{\dot{P}_O}{P_i} = \frac{c\beta_\perp^2}{d} \,, \tag{2.10}$$

then

$$r = d_p \,. \tag{2.11}$$

Another case where the pulsar is orbiting in the Sgr A*-observer plane with $\dot{P} = 5 \times 10^{-15}$ and $M \approx M_{BH}$ is presented in Figure 2.2.

2.2.2 The second period derivative

If $\dot{P}_O$ is measured, equation (2.9) constitutes a new constraint on the pulsar's phase space coordinates, allowing all 6 components to be determined. This last constraint is a function of the enclosed mass, M, which can be solved via a measurement of another period derivative. Taking the derivative of equation (2.3) and noting that $r \ll d$ we find:

$$\frac{\ddot{P}_O}{P_i} = -\frac{GM}{c}\frac{\partial}{\partial t}\left[\frac{\cos\phi}{r^2}\right] \tag{2.12}$$

$$= \frac{GM}{c}\left[\frac{\sin\phi}{r^2}\frac{\partial\phi}{\partial t} + \frac{2}{r^3}\cos\phi\frac{\partial r}{\partial t}\right] \,. \tag{2.13}$$

A pulsar on a purely circular orbit with an orbital frequency $\Omega = \beta c/r$ orbiting in the pulsar-Sgr A*-observer plane, has

$$\frac{\partial r}{\partial t} = 0 \qquad ; \qquad \frac{\partial \phi}{\partial t} = -\Omega = -\beta \frac{c}{r} \, , \tag{2.14}$$

implying

$$\frac{\ddot{P}_O}{P_i} = -\frac{GM}{c} \frac{\sin \phi}{r^2} \Omega = -GM \frac{d_p}{r^4} \beta \, , \tag{2.15}$$

which can be solved trivially for either $M(r)$ or $r(M)$ given β (or limits of the quantity given the proper motion, $\beta_\perp \leq \beta$) and the projected separation d_p. For a pulsar with $P_O = 1$ s at the projected separation of J1745-2900 ($d_p = 0.09$ pc), that is currently at a phase of its orbit where $r \sim d_p$ and $\beta \sim 0.3 \times 10^{-3}$, we find that:

$$|\ddot{P}| \approx 5 \times 10^{-23} \text{ s}^{-1} \, . \tag{2.16}$$

Within 1 year, the drift in $\dot{P}$ is:

$$|\Delta \dot{P}| \approx 1.5 \times 10^{-15} \, , \tag{2.17}$$

which is within the precision attainable in pulsar measurements (Taylor et al. 1993; Manchester et al. 2005). If a millisecond pulsar is found at the Galactic Center, then $\dot{P}$ could be measured to a precision of 10^{-20} (e.g. Champion et al. 2005). In general,

$r^2 = (d_p^2 + r_l^2)$, therefore:

$$\frac{\partial r}{\partial t} = \frac{1}{2r}\frac{\partial r^2}{\partial t} \tag{2.18}$$

$$= \frac{1}{\pm 2\sqrt{d_p^2 + r_l^2}}\frac{\partial}{\partial t}(d_p^2 + r_l^2) \tag{2.19}$$

$$= \pm\frac{1}{r}\left(d_p v_\perp \frac{\vec{v}_\perp \cdot \vec{d}_p}{d_p v_\perp} + r_l v_l\right) , \tag{2.20}$$

where $\vec{v}_\perp$ is the proper velocity and v_l is the velocity in the line of sight direction. Furthermore we note that:

$$-\frac{\sin\phi}{r^2}\frac{\partial\phi}{\partial t} = \frac{d_p}{r^4} v \cos i , \tag{2.21}$$

where i is the inclination of the pulsar's orbit. This factor of $\cos i$ can be written as:

$$\cos i = \pm\frac{\sqrt{v^2 - v_{oop}^2}}{v} = \pm\frac{\sqrt{v_\perp^2 + v_l^2 - v_{oop}^2}}{v} , \tag{2.22}$$

where,

$$v_{oop} = \frac{|\vec{v}_\perp \times \vec{d}_p|}{d_p} \tag{2.23}$$

is the component of the proper velocity $v_\perp$ that is off the pulsar-Sgr A*-observer plane. This quantity can be obtained directly from the proper velocity by a projec-

tion to the pulsar-Sgr A*-observer plane. Combining, we obtain,

$$\frac{\ddot{P}_O}{P_i} = \frac{GM}{c(d_p^2 + r_l^2)^2} \left[\pm 2 \frac{r_l}{\sqrt{d_p^2 + r_l^2}} \left(\vec{v}_\perp \cdot \vec{d}_p + r_l v_l \right) \pm d_p \sqrt{v_\perp^2 + v_l^2 - v_{oop}^2} \right] . \quad (2.24)$$

Measuring $\ddot{P}_O/P_i$ provides another constraint on the orbital phase space coordinates and the enclosed mass of the pulsar's orbit. An example of constraining $r_l(v_l)$ where the pulsar is orbiting in the pulsar-Sgr A*-observer plane with $\ddot{P} = 10^{-24}$ s^{-1} and $M \approx M_{BH}$ is plotted in Figure 2.2.

If we instead assume that r_l is known (e.g. from parallax), the constraints from $\ddot{P}_O$ and $\dot{P}_O$ can be used to solve simultaneously for v_l and the mass enclosed within the orbital radius. This corresponds to the intersection of the two constraints in Figure 2.3.

The intrinsic $\ddot{P}$

While the observed $\ddot{P}$ of a young pulsar is typically dominated by its intrinsic timing noise, the intrinsic $\ddot{P}$ for old or millisecond pulsars can be dominated instead by radiation losses (Lorimer 2008). Assuming the vacuum dipole model, we can estimate the intrinsic contribution, $\ddot{P}_i$. If we assume that $B \sin\alpha$ does not change significantly with time (i.e. that magnetic field decay timescales are long), the quantity $(P\dot{P})_i$ is constant:

$$(P\dot{P})_i = \frac{8\pi^2 R^6 (B \sin\alpha)^2}{3c^3 I} = \text{constant} , \quad (2.25)$$

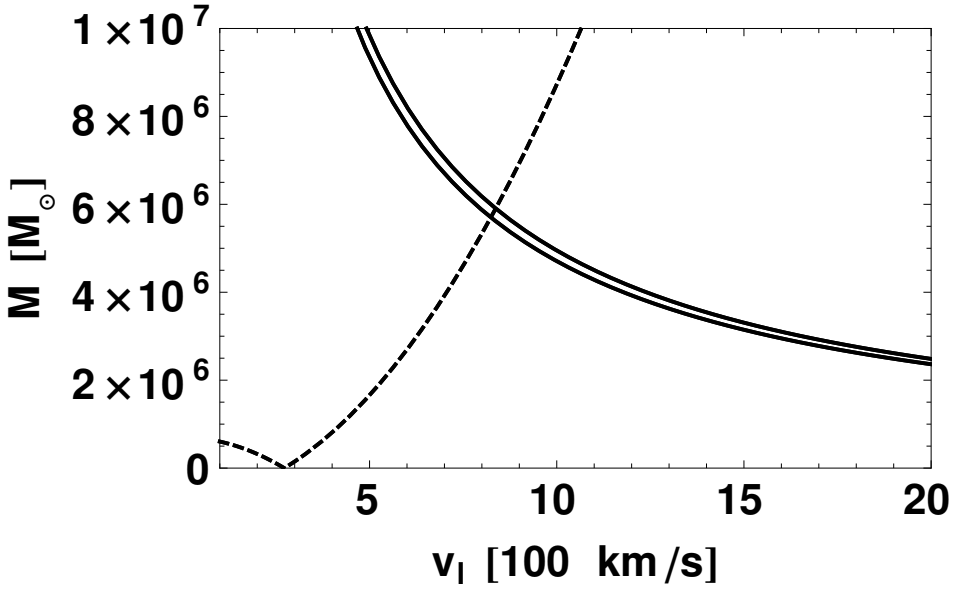

Figure 2.3: Constraints on the mass distribution based on $\ddot{P}_O$ and $\dot{P}_O$. Supposing that the other 5 phase space coordinates are known, the constraints from $\ddot{P}_O$ (solid line) and $\dot{P}_O$ (dashed line) can be solved simultaneously for v_l and M, corresponding to the intersection of the two constraints. In this case, the pulsar is orbiting in the pulsar-Sgr A*-observer plane with $\dot{P} = 10^{-14}$, $\ddot{P} = 10^{-23}$ s^{-1}, $d_p = 0.01$ pc, $v_\perp = 150$ km s^{-1}, and $r_l = 0.2$ pc. Due to the sign degeneracy, the $\ddot{P}$ constraint in this case corresponds to two solid lines in the M versus v_l plane. This degeneracy can be resolved by fixing v_l, for example, through the third derivative constraint. Note that enclosed masses below the mass of Sgr A*, $M_{BH} = (4.31 \pm 0.36) \times 10^6 M_\odot$ (Ghez et al. 2008) should be excluded from the analysis.

where α is the magnetic axis inclination angle, B the magnetic field strength, I the moment of inertia, and R the neutron star radius. Taking another time derivative, we obtain:

$$\ddot{P}_i = -\frac{64\pi^4 R^{12} (B \sin\alpha)^4}{9c^9 I^2 P_i} \ . \tag{2.26}$$

Considering $P \approx P_i \approx 1$ s, a magnetic field $B = 10^{12}$ G, and the typical radius, $R = 10$ km, and mass, $M = 1.4 M_\odot$, for a neutron star, and adopting $\sin\alpha = 1$, we obtain the maximum $\ddot{P}_i$ to be:

$$\ddot{P}_{i,\,\mathrm{max}} = 7.6 \times 10^{-31}\ \mathrm{s}^{-1} \ , \tag{2.27}$$

which is very small compared to the orbital contribution. This suggests that unlike $\dot{P}$, $\ddot{P}$ is much less contaminated by the intrinsic contribution, allowing a clean measurement of $\ddot{P}_O$. In general, the inclination angle α can be inferred by various methods (Taylor et al. 1993; Lyne & Manchester 1988; Rankin 1990; Miller & Hamilton 1993).

2.2.3 The Third period Derivative

We now supply the third period derivative. This third timing constrain can be used in lieu of the $\dot{P}$ constraint in cases where $\dot{P}_{obs}$ is too contaminated by $\dot{P}_i$. In addition, all three timing constraints can be used in cases where only 4 phase space coordinates are measured (e.g. for pulsars with no measured parallax). We also note that

the third derivative $\dddot{P}$ is even less affected by its intrinsic contribution than $\ddot{P}$, since $\dddot{P}_i \propto B^6/P_i^3$. The derivative of equation (2.13) is:

$$\frac{\dddot{P}_O}{P_i} = \frac{GM}{c}\left[\frac{2}{r^3}\cos\phi\frac{\partial^2 r}{\partial t^2} + \frac{1}{r^2}\sin\phi\frac{\partial^2\phi}{\partial t^2} - \frac{6}{r^4}\cos\phi\left(\frac{\partial r}{\partial t}\right)^2 + \frac{1}{r^2}\cos\phi\left(\frac{\partial\phi}{\partial t}\right)^2 - \frac{4}{r^3}\sin\phi\frac{\partial r}{\partial t}\frac{\partial\phi}{\partial t}\right] , \tag{2.28}$$

with the following equalities:

$$\frac{\partial^2 r}{\partial t^2} = -\frac{2}{r^2}(\vec{d}_p\cdot\vec{v}_\perp + r_l v_l)\frac{\partial r}{\partial t} + \frac{1}{r}\left[v_\perp^2 + \vec{d}_p\cdot\vec{a}_\perp + v_l^2 + r_l a\cos\phi\right] , \tag{2.29}$$

$$\frac{\partial^2\phi}{\partial t^2} = \frac{\partial}{\partial t}\left(-\frac{v}{r}\cos i\right) = \cos i\left[\frac{v}{r^2}\frac{\partial r}{\partial t} - \frac{1}{r}\frac{\partial v}{\partial t}\right] , \tag{2.30}$$

and

$$\frac{\partial v}{\partial t} = \frac{1}{v}\left[v_l a\cos\phi - a\sin\phi\frac{\vec{d}_p\cdot\vec{v}_\perp}{d_p}\right] , \tag{2.31}$$

where $a = GM/r^2$ and $\vec{a}_\perp$ is its components perpendicular to the line of sight. The magnitude of this orbital contribution can be estimated as (Phinney 1993):

$$\left|\frac{\dddot{P}_O}{P_i}\right| \approx 2\left[\frac{GM}{r^4}\right]\frac{v^2}{c} \approx 3.1\times10^{-33}\ \mathrm{s}^{-3}, \tag{2.32}$$

where for the second equality we plugged in numbers for a pulsar at 0.1 pc from the

black hole moving at $v \sim 200$ km s^{-1}. If the pulsar has period $P_O = 1$ s, in a year this induces a drift on $\ddot{P}_O$ of magnitude $\dddot{P}_O \times (1 \text{ year}) \approx 9.4 \times 10^{-26}$ s^{-1}, which is comparable in magnitude to the measured $\ddot{P}$'s of many observed pulsars (Manchester et al. 2005).

For a well studied pulsar with both a measured $\ddot{P}$ and $\dddot{P}$, we get two timing constraints on the phase space coordinates. If the pulsar has a low magnetic field strength or if $\dot{P}_O$ dominates, there will be a third timing constraint. Treating $M(r)$ as an unknown function, these extra constraints can be used to directly measure the mass enclosed within the pulsar's orbit. The method is analogous to that presented in §2.3.

2.3 Contributions by stellar kicks and measuring the characteristic stellar mass at the Galactic Center

As pointed out in Phinney (1993), stars passing close to the pulsar can gravitationally kick the pulsar, adding another contribution to the time derivatives of the pulsar's period. In this section we quantify the probability for these stochastic effects to significantly affect the mean field contribution. The probability of a star being a distance $< b$ away from the pulsar located a distance r away from Sgr A* is:

$$Pr(r) = 1 - \exp[-(4\pi/3)n_* \pi b^3] \,, \tag{2.33}$$

where n_* is the number density of stars. Using a density profile for stars around Sgr A* $n_* = n_0(r/r_0)^{-1.8}$, and the fact that the total stellar mass at 1 pc is measured to be $M_{1pc} \sim 2 \times 10^6\ M_\odot$ (Genzel et al. 2010), the probability represented in equation (2.33) becomes:

$$Pr(r) = 1 - \exp\left[-\frac{4\pi}{3} b^3 \left(\frac{1.2 M_{1pc}}{4\pi m_* (1\text{ pc})^{1.2}}\right) r^{-1.8}\right] . \tag{2.34}$$

The contribution of the nearest neighboring star to $\dot{P}$ equals the mean field contribution at a distance that satisfies,

$$b^2 = \frac{m_*}{M_*(r) + M_{BH}} r^2 , \tag{2.35}$$

where $M_*(r)$ is the total stellar mass within the orbit. The probability for this separation is,

$$Pr(r) = 1 - \exp\left[-\frac{1.2}{3} \frac{M_{1pc}\sqrt{m_*}}{(M_{1pc}(r/1\text{ pc})^{1.2} + \mathrm{M_{BH}})^{3/2}} \left(\frac{r}{1\text{ pc}}\right)^{1.2}\right] . \tag{2.36}$$

For all reasonable values for m_*, this probability is negligibly small at all radii, showing that the first derivative is uncontaminated by stellar kicks. We corroborated this analytical analysis with a numerical N-body simulation utilizing the Salpeter mass function for stars. The initial conditions for this simulation were generated using the star cluster integrator, bhint (Löckmann & Baumgardt 2008) with density profile

$\rho \propto r^{-1.8}$ and a supermassive black hole of mass $4.3 \times 10^6 M_\odot$ located at the center of the cluster.

However, the contributions of stellar kicks to the higher derivatives is larger. The nearest neighbor contribution to $\ddot{P}/P$ is (Phinney 1993):

$$\left[\frac{\ddot{P}}{P}\right]_{nn} \approx \frac{G m_*}{b^3}\frac{v_*}{c}\,, \tag{2.37}$$

where v_* is the relative velocity between the star and the pulsar. Similarly, the mean field contribution is:

$$\left[\frac{\ddot{P}}{P}\right]_{mf} \approx \frac{G(M_*(r) + M_{BH})}{r^3}\frac{v}{c}\,, \tag{2.38}$$

where v is the pulsar's orbital speed relative to Sgr A*. Equating the two contributions, we find that the nearest neighbor contribution equals the mean field at,

$$b^3 = \frac{m_*}{M_*(r) + M_{BH}}\frac{v_*}{v} r^3\,. \tag{2.39}$$

The probability for this separation is again obtained from equation (2.34):

$$Pr(r) = 1 - \exp\left[-\frac{1.2}{3}\frac{v_*}{v}\frac{M_{1pc}}{M_{1pc}(r/1\text{ pc})^{1.2} + \mathrm{M_{BH}}}\left(\frac{r}{1\text{ pc}}\right)^{1.2}\right]\,. \tag{2.40}$$

The probability decreases with r, so that pulsars closer to Sgr A* are less disturbed by perturbing stars. At a distance of 0.01 pc, the probability for the associated jerks

is less than 0.1%. To corroborate this result, we performed a numerical simulation utilizing the Salpeter mass function as displayed in Figure 2.4. This simulation shows that passing stars scatter $\ddot{P}$ about its mean field value, and its contribution is large at distances larger than ~ 0.03 pc.

While the analysis of §2 is largely unaffected at small r, the contribution of passing stars adds a significant source of uncertainty to the interpretation of measured period derivatives at large r. Due to the stochastic nature of this contribution, measuring $M(r)$ at large distances necessitates the use of multiple pulsars, whose average $\ddot{P}$ should reveal the mean field.

2.3.1 Effect of changing m_* on $\dddot{P}$

Although the probability for $\ddot{P}$ to be significantly contaminated by perturbing stars is independent of the characteristic stellar mass, m_*, this is not true for all time derivatives. Here we show that the third period derivative is sensitive to changes in m_*, and that this dependence can be used to probe the characteristic stellar mass at the Galactic Center. The nearest neighbor contribution to $\dddot{P}/P$ is (Phinney 1993):

$$\left[\frac{\dddot{P}}{P}\right]_{nn} \approx 2\frac{Gm_*}{b^4}\frac{v_*^2}{c} \ . \tag{2.41}$$

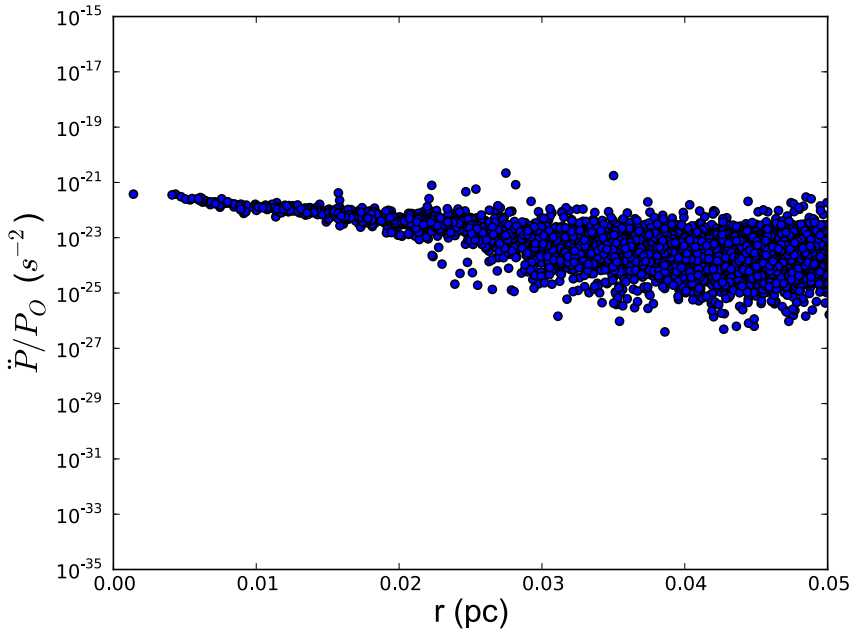

Figure 2.4: Numerical simulation of $\ddot{P}/P_O$. The Galactic Center was modeled as a star cluster generated by the post-Newtonian integrator bhint (Löckmann & Baumgardt 2008) with density profile $\rho \propto r^{-1.8}$ and a central supermassive black hole of mass $4.3 \times 10^6 M_\odot$.

The mean field contribution is:

$$\left[\frac{\dddot{P}}{P}\right]_{mf} \approx 2\left[\frac{G(M_*(r)+M_{BH})}{r^4}\right]\frac{v^2}{c}\ . \tag{2.42}$$

The nearest neighbor and the mean field contributions are equal when,

$$b^3 = \left[\frac{m_*}{M_*(r)+M_{BH}}\left(\frac{v_*}{v}\right)^2 r^4\right]^{3/4}\ . \tag{2.43}$$

In this case, the probability for a star to pass at distance $< b$ from the pulsar is:

$$Pr(r) = 1 - \exp\left[-\frac{1.2}{3m_*^{1/4}}\left(\frac{v_*}{v}\right)^{3/2}\frac{M_{1pc}}{(M_{1pc}(r/1\text{ pc})^{1.2} + \mathrm{M_{BH}})^{3/4}}\left(\frac{r}{1\text{ pc}}\right)^{1.2}\right] . \quad (2.44)$$

Figure 2.5 shows this probability as a function of pulsar-Galactic Center distance for $m_* = 1,\ 5,\ \&\ 10M_\odot$. The differences between cases of different m_*'s maxes out at around $r \approx 2$ pc, thus making this the optimal location to perform this study. We note that the difference between $Pr(0.2\text{ pc})$ with $m_* = 1M_\odot$ and $m_* = 10M_\odot$ is $\sim 20\%$, and so with Poisson statistic one needs tens of pulsars to distinguish between the two cases.

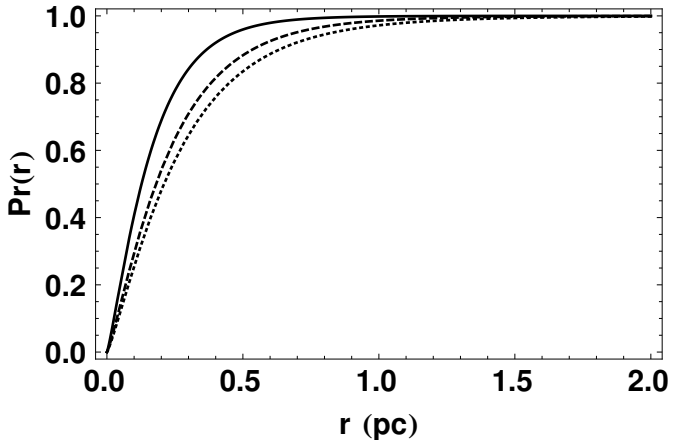

Figure 2.5: The probability for a large nearest neighbor contribution to $\dddot{P}/P$ versus pulsar's orbital radius r for characteristic stellar masses of $m_* = 1,\ 5,\ \&\ 10M_\odot$ in solid, dashed, and dotted lines, respectively.

2.4 Summary and Implications

If the pulsar's projected separation from Sgr A*, proper velocity, and line of sight distance are measured, then 5 of the 6 pulsar's phase space coordinates are known. One of the period derivative constraints represented by equations (2.9), (2.24), or (2.28) can then be used to derive a final constraint on the pulsar's phase space coordinates. Another constraint can be used to limit the mass enclosed within the pulsar's orbit. In this case, the line of sight velocity $v_l = v_l(M)$ depends on M itself. As such, $M(\vec{r}, \vec{v}) = M(\vec{r}, \vec{v}_\perp, v_l(M, \vec{r}, \vec{v}_\perp)) = M(\vec{r}, \vec{v}_\perp)$. Due to this complicated dependence, an analytic solution is not feasible and the related analysis has to be done numerically.

The mass distribution itself can be determined if the above measurements are performed at multiple times for a pulsar on a plunging orbit. However, unless the pulsar is located very close to Sgr A*, the orbital timescale is too long for such a study. Nevertheless, by performing this measurement on multiple pulsars, one would still be able to probe the radial mass distribution. In particular, the difference in the measured $M(r)$'s of two pulsars located at two radial distances determines the mass enclosed in the spherical shell between these radii. This can be used to constrain the distribution of low-mass stars or stellar remnants (black holes, white dwarfs, and neutron stars) that are too faint to be detected directly.

An extra source of uncertainty in measuring $M(r)$ comes from the effects of passing stars. These scatter $\ddot{P}$ about the mean field value, and the contribution is large

for r greater than ~ 0.03 pc. As such, measurements should be taken close to Sgr A*, where they can constrain cumulative mass of stars and stellar remnants surrounding the black hole. Measuring $M(r)$ further away from Sgr A* will require multiple pulsars, and thus be a challenging task.

Finally, we note that the scatter of $\dddot{P}$ about the mean field value due to passing stars is affected by the characteristic stelar mass, m_*. As such, measurements of $\dddot{P}$ of multiple pulsars at the Galactic Center will allow us to probe the charasteristic mass of stars and remnants in this extreme environment. Such measurements can also place exquisite constraints on the existence of intermediate-mass black holes in the vicinity of Sgr A*.

2.5 Acknowledgment

We thank Vicky Kaspi and Sterl Phinney for helpful comments on the manuscript. This work was supported in part by NSF grant AST-1312034.

3

Mapping the dynamics of cold gas around Sgr A* through 21 cm absorption

The presence of a circumnuclear stellar disk around Sgr A* and megamaser systems near other black holes indicates that dense neutral disks can be found in galactic nuclei. We show that depending on their inclination angle, optical depth, and spin tem-

perature, these disks could be observed spectroscopically through 21 cm absorption. Related spectroscopic observations of Sgr A* can determine its HI disk parameters and the possible presence of gaps in the disk. Clumps of dense gas similar to the G2 could could also be detected in 21 cm absorption against Sgr A* radio emission.

3.1 Introduction

The presence of a disk of massive young stars around the Galactic Centre (Levin & Beloborodov 2003) and various megamaser systems (Miyoshi et al. 1995; Moran et al. 2007; Herrnstein et al. 2005; Kuo et al. 2011) indicates that dense neutral disks can be found in galactic nuclei. These disks could be produced by the tidal disruption of molecular clouds passing close to the central supermassive black hole (Yusef-Zadeh & Wardle 2012). The disk could be an outer extension of the hot accretion disk closer to the black hole, and possess a large amount of neutral hydrogen. Indeed, a significant portion of the H_2O megamasers show X-ray absorption with large column densities of $10^{24} - 10^{25}$ cm^{-2}(Loeb 2008). Further, the discovery of the G2 cloud (Gillessen 2014) indicates that dense clouds of self-shielded neutral hydrogen may exist around Sgr A*.

Here we present a method to observe HI disks in the intermediate region of $10^3 - 10^4$ Schwarzschild radii around nuclear black holes through their 21 cm absorption. The inherent brightness of such a disk is too weak to be detectable, however the black hole's inner accretion flow emits synchrotron radiation (Bower et al. 2014b) that acts

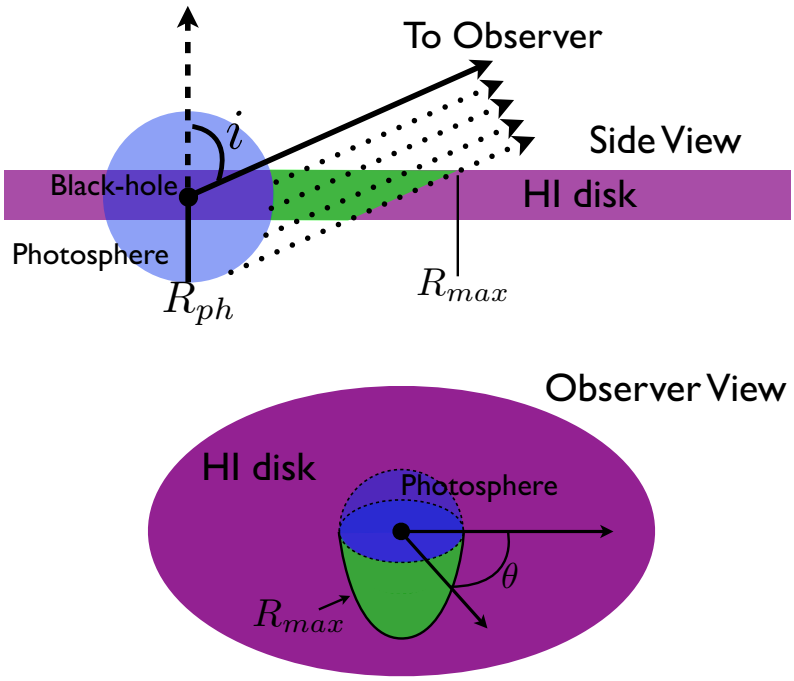

Figure 3.1: A sketch of the geometry from the side (top image) and as seen by the observer (bottom image). The black hole is surrounded by an optically thick photosphere with a radius R_{ph} and an HI disk. The solid arrow in the top image indicates the direction towards the observer. The inclination angle i is the angle between the observer and the normal to the disk. The dotted arrows in the top image depict photons leaving the photosphere in the direction of the observer. In their path towards the observer, these photons encounter the HI disk and their intensity is reduced by absorption. The region of the HI disk that is illuminated by these photons is shaded green in both images. The outer radius of this region, as seen from the observer's point of view (bottom image), is referred to as R_{max}.

as a background source upon which the neutral systems can be seen in absorption.

We examine how observations of the absorption spectrum allows one to determine the parameters of the HI absorber without the need to spatially resolve the system.

3.2 21 cm absorption profile

The accretion flow near Sgr A* is optically-thick to synchrotron self-absorption at a wavelength of 21 cm, and this photosphere illuminates the outer HI disk. At a distance D, the photosphere intensity $I_{\nu 0}$ yields a flux of

$$\begin{aligned} F_\nu &= \int_{\mathrm{A}} \frac{r d\theta dr}{D^2} I_{\nu 0} e^{-\tau_\nu} \\ &\approx \int_{\mathrm{A}} \frac{r d\theta dr}{D^2} I_{\nu 0}(1-\tau_\nu) \ , \end{aligned}$$

where $I_{\nu 0}$ is the photospheric specific intensity, (r, θ) are coordinates on the disk plane centered on Sgr A*, and the integral is over the area A of the disk that is illuminated by Sgr A*'s photosphere. The frequency dependent optical depth is given by (Loeb 2008),

$$\tau_\nu(r,\theta) = \frac{3}{32\pi} \frac{h^3 c^2 A_{21}}{E^2} \frac{N_H}{k T_s} \nu \phi \left[\nu - \frac{1}{c} \sqrt{\frac{GM}{r}} \sin i \cos\theta \right] \ , \tag{3.1}$$

where M is the black hole mass, i the disk inclination defined as the angle between the observer and the normal to the disk (refer to Figure 3.1), $A_{21} = 2.85 \times 10^{-25}$ s^{-1} is the Einstein coefficient of the 21 cm transition, $E/k = 0.068$ K is the 21 cm transition energy, N_H is the HI column density in the disk, ν is the frequency, and T_S is the gas

spin temperature. For our calculations, the line function ϕ is a gaussian,

$$\phi\left[\nu - \frac{1}{c}\sqrt{\frac{GM}{r}}\sin i\cos\theta\right] \equiv \tag{3.2}$$

$$\frac{1}{\sqrt{2\pi}\sigma}\exp - \left\{\frac{\left[\nu - \nu_{21}\left(1 - \frac{1}{c}\sqrt{\frac{GM}{r}}\sin i\cos\theta\right)\right]^2}{2\sigma^2}\right\}, \tag{3.3}$$

with $\sigma \ll \nu_{21} \equiv 1.4 \times 10^9$ Hz. For a black hole with a photosphere radius R_{ph}, the area A can be evaluated geometrically. Assuming that the disk is larger than the photosphere, the amount of disk that is illuminated by the photosphere is the half-circular area spanned by the photosphere projected onto the disk. Only half a circle is required because the other half the disk is positioned behind the photosphere. For a disk with an inclination i, the projection gives

$$F_\nu = \int_{\theta=0}^{\theta=\pi}\int_{r=R_{ph}}^{r=R_{max}} \frac{r d\theta dr}{D^2} I_{\nu_0}(1-\tau_\nu)\,, \tag{3.4}$$

where

$$R_{max} \equiv R_{ph}\sqrt{\sin^2\theta\tan^2 i + 1}\,, \tag{3.5}$$

is the outer radius of the region in the disk that participates in absorption (see Figure 3.1). The absolute value of the term proportional to τ_ν can be written as

$$\begin{aligned}\delta F_\nu &\equiv \int_{\theta=0}^{\theta=\pi}\int_{r=R_{ph}}^{r=R_{max}} \frac{r d\theta dr}{D^2} I_{\nu_0}\tau_\nu \\ &= \int_{\theta=0}^{\theta=\pi}\int_{r=R_{ph}}^{r=R_{max}} \frac{r d\theta dr}{D^2} I_{\nu_0} \\ &\quad \times \left[\frac{3}{32\pi}\frac{h^3c^2A_{21}}{E^2}\frac{N_H}{kT_s}\nu\phi\left(\nu - \frac{1}{c}\sqrt{\frac{GM}{r}\sin i\cos\theta}\right)\right] . \end{aligned} \tag{3.6}$$

In general, N_H and T_S may depend on the radial coordinate r. In addition, I_{ν_0} also depends on both r and θ due to limb darkening.

3.2.1 Homogeneous disk with no limb darkening

For simplicity, we focus our attention to a homogeneous disk where N_H, T_S, and I_{ν_0} are constants. From equation (3.6),

$$\begin{aligned}\delta F_\nu &= \frac{3}{32\pi}\frac{h^3c^2A_{21}}{E^2}\frac{N_H}{kT_s}\nu\left(\frac{I_{\nu_0}}{D^2}\right)\int_{\theta=0}^{\theta=\pi} d\theta \\ &\quad \times \int_{r=R_{ph}}^{r=R_{max}} dr\; r\phi\left(\nu - \frac{1}{c}\sqrt{\frac{GM}{r}\sin i\cos\theta}\right) . \end{aligned} \tag{3.7}$$

Besides the multiplicative factor $\frac{N_H I_{\nu_0}}{T_S D^2}$, the problem possesses only two free parameters: the disk inclination angle, i, and the radius of the photosphere, R_{ph}. Although the intrinsic size of of Sgr A* was never measured at a wavelength as long as 21 cm,

we extrapolate from the results of Bower et al. (2014b) and find $R_{ph} \sim 10^{15}$ cm. The depth of the line profile relative to the continuum, $\delta F_\nu / F_{\nu_0}$, is shown in Figure 3.3 for $N_H = 10^{21}$ cm^{-2} and $T_S = 8 \times 10^3$ K. Note that $\delta F_\nu \propto N_H / T_S$ more generally. The distance to the Galactic center is taken as $D = 8$ kpc. A physical understanding of the absorption profiles can be obtained by looking at the line of sight velocity structure of the disk as shown in Figure 3.2. Due to the Doppler shift, an observer would detect a line of sight velocity that varies like a dipole on the disk (contours of $\sim \cos\theta/\sqrt{r}$). The portion of the disk that is illuminated by the photosphere, i.e. between $0 \leq \theta \leq \pi$ and $R_{ph} \leq r \leq R_{max}$, is seen in absorption. At every point in the illuminated disk (parameterized by the disk coordinates r and θ), there is a corresponding drop of flux in the frequency profile at $\nu = \sqrt{GM \sin i \cos\theta / rc^2}$ due to the absorption at that point.

The change in the shape of the absorption profile when one changes R_{ph} and i can be explained by the shape of $R_{max}(R_{ph}, i)$ on the neutral disk. As Figure 3.2 shows, the outer bounds of the illuminated disk increases with increasing R_{ph}. This increases the area of the illuminated disk, generating a deeper absorption profile. However, as R_{ph} increases, a larger portion of the inner disk is hidden behind the photosphere. This removes high velocity components from the integral, causing a thinner spectral profile. Indeed, Figure 3.3 demonstrates that increasing R_{ph} produces a deeper and thinner absorption profile. A more edge-on (higher i) disk also possesses a larger illuminated disk. In this case, the inner bound is not changing, thus the wider illumi-

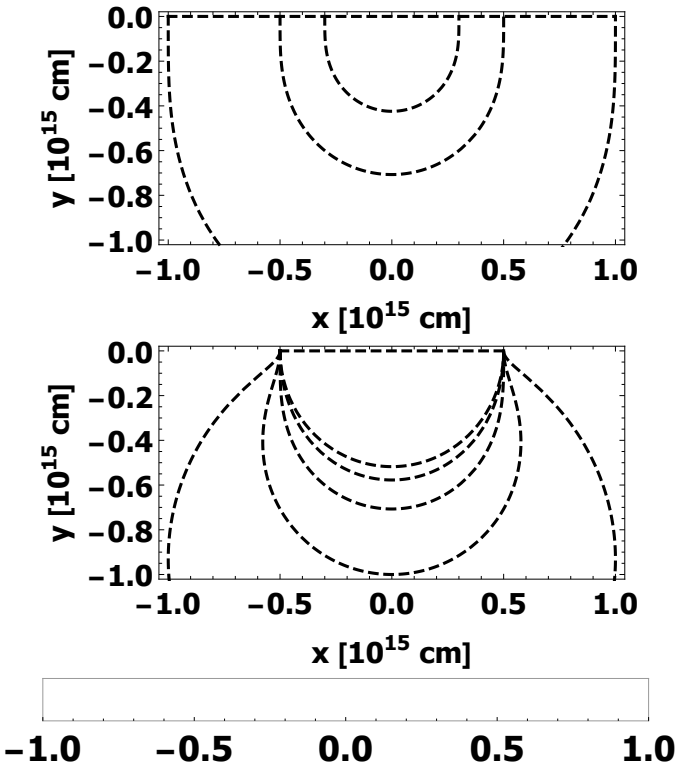

Figure 3.2: The neutral disk as seen by the observer. Due to the Doppler shift, an observer sees a line of sight velocity profile that traces a dipole on the neutral disk (The black hole is located at $x, y = 0$). The color describes the magnitude of the line of sight velocity; areas with larger (lower) redshifts are redder (bluer). The value in the color bar is normalized to $\sqrt{GM \sin i/r}$. The boundary of the disk that is illuminated by the photosphere, R_{max}, is plotted in dashed lines for a variety of photosphere radii, R_{ph} (top) and a variety of inclinations, i (bottom). The outermost R_{max} in the top panel corresponds to $R_{ph} = 10^{15}$ cm, and the successively smaller contours are for $R_{ph} = 5 \times 10^{14}$ cm and $R_{ph} = 3 \times 10^{14}$ cm. The outermost R_{max} in the bottom panel corresponds to $i = 15°$, and the successively smaller contours corresponds to $i = 30°,\ 45°,\ 60°,\ \&\ 75°$. The x and y axes are Cartesian coordinates on the disk, in units of 10^{15} cm. The portion of the disk that is seen in absorption is within $0 \leq \theta \leq \pi$ and $R_{ph} \leq r \leq R_{max}$. Increasing R_{ph} samples a wider region of the disk, but a larger part of the high velocity portion of the disk close to the black hole is hidden behind the photosphere. This results in an absorption profile that is deeper and thinner. A more edge-on (higher i) disk samples a wider region of the disk. Furthermore, the shape of the illuminated portion of a more edge-on disk covers higher velocity features, generating a deeper and wider absorption profile (see Figure 3.3).

nated disk also contains more high velocity portions. This generates a deeper and wider profile, as seen in Figure 3.3.

3.2.2 Disks with gaps

Using the formalism of equation (3.7) we can also calculate the resulting 21 cm absorption profile in the case where there are gaps in the HI disk. This is done by simply breaking the radial integral into parts,

$$f_\nu \sim \begin{cases} \int_{\theta=0}^{\theta=\pi} \int_{r=R_{ph}}^{r=R_{max}} I & R_{max} < R_{in} \\ \int_{\theta=0}^{\theta=\pi} \int_{r=R_{ph}}^{r=R_{in}} I & R_{in} < R_{max} < R_{out} \\ \int_{\theta=0}^{\theta=\pi} \left[\int_{r=R_{ph}}^{r=R_{in}} I + \int_{r=R_{out}}^{r=R_{max}} I \right] & R_{out} < R_{max} \ , \end{cases}$$

where I is the integrand of equation (3.7), R_{in} is the inner radius of the gap, and R_{out} is the gap's outer radius. The integral can be broken to more pieces if more gaps are present. An example profile for a disk with a gap is shown in Figure 3.4. A disk with a gap lacks absorption on the region where the gap is located. Based on the dipolar contours of Figure 3.2, the velocities corresponding to a portion between $R_{in} < r < R_{max}$ is excluded from the integral, generating a profile with visible wings. The detection of a gap can be used to constraint the presence of an intermediate mass black hole companion of Sgr A* orbiting with a semimajor axis of $\sim 10^3 - 10^5$ Schwarzschild radii.

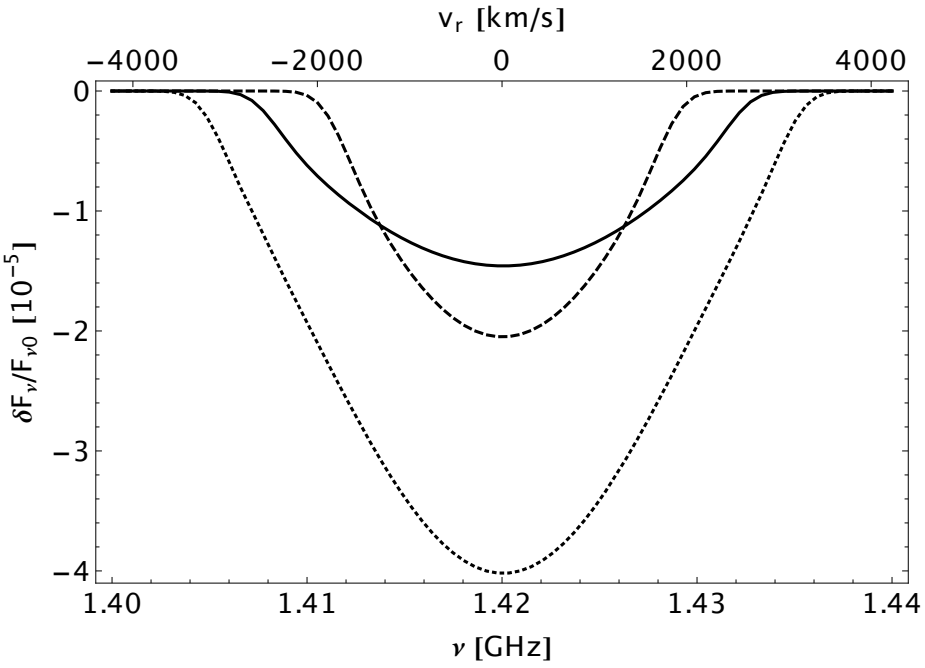

Figure 3.3: Absorption profile of the Sgr A* photosphere for $R_{ph} = 10^{15}$ cm and an inclination angle of $i = \pi/4$ (solid), $R_{ph} = 2 \times 10^{15}$ cm and $i = \pi/4$ (dashed), as well as $R_{ph} = 10^{15}$ cm and $i = \pi/3$ (dotted). v_r denotes the line-of-sight velocity. Since the disk is behind the photosphere when $r < R_{ph}$, a larger photosphere samples less of the high velocity regions of the disk, resulting in a thinner profile. However, a larger photosphere illuminates a larger disk area, resulting in more absorption. Increasing R_{ph} therefore results in a deeper, but thinner profile. Edge-on geometry implies a larger portion of the disk is illuminated by the photosphere, therefore increasing the angle i results in a deeper profile. A disk with higher i samples higher velocity regions, resulting in a wider profile. These extra high velocity regions are sampled at the edges of the illuminated disk, in contrast to the high velocity regions sampled in systems with larger R_{ph}, where the extra regions are located closer to the black hole (see Figure 3.2).

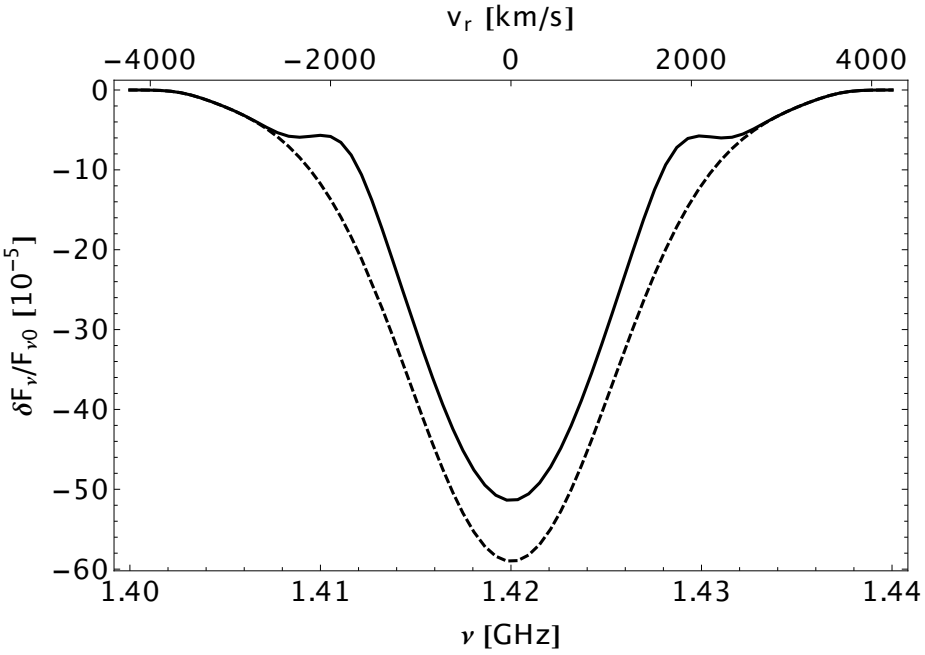

Figure 3.4: 21 cm absorption profile for a disk inclined by 80 degrees and $R_{ph} = 2 \times 10^{15}$ cm with a gap of width $\sim R_{ph}$ (solid) overplotted against a disk with no gap (dashed). v_r denotes the line-of-sight velocity.

3.2.3 Orbiting dense cloud

Another source of HI is a dense cloud that orbits in front of the 21 cm photosphere. This dense spot could be a feature in the neutral disk or a clump of self-shielded gas similar to the G2 cloud (Gillessen 2014). The resulting profile will be like that of Figure 3.3, but with an extra absorption feature located where the spot resides in frequency space, as shown schematically in Figure 3.5. The core of this feature travels in ν-space as the cloud orbits the black hole. If the spot orbits in a perfect circular orbit, the frequency position of the center of the feature, ν_c, obeys

$$\nu_{\mathrm{c}}(t) = 1.4 \times 10^{9}\mathrm{Hz}\left[1 - \frac{1}{\mathrm{c}}\sqrt{\frac{\mathrm{GM}}{\mathrm{r_c}}}\sin\mathrm{i}\cos\left(\sqrt{\frac{\mathrm{GM}}{\mathrm{r_c^3}}}(\mathrm{t}-\mathrm{t_0})\right)\right] , \tag{3.8}$$

where r_c is the radial position of the dense spot, and t the time coordinate relative to an arbitrary initial time t_0. The resulting effect in frequency space is a feature that oscillates sinusoidally around the 21 cm rest frame frequency. The amplitude of the oscillation is $\sqrt{\frac{GM}{c^2 r_c}}\sin i$ and the temporal frequency is $\sqrt{\frac{GM}{r_c^3}}$. Since both of these are observables, one can use them to measure simultaneously the orbital radius and the black hole mass up to a factor of $\sin i$. Plunging orbits can be treated by adding a time dependence to r_c,

$$\nu_{\mathrm{c}}(t) = 1.4 \times 10^{9}\mathrm{Hz}\left[1 - \frac{1}{\mathrm{c}}\sqrt{\frac{\mathrm{GM}}{\mathrm{r_c(t)}}}\sin\mathrm{i}\cos\left(\sqrt{\frac{\mathrm{GM}}{\mathrm{a^3}}}(\mathrm{t}-\mathrm{t_0})\right)\right] , \tag{3.9}$$

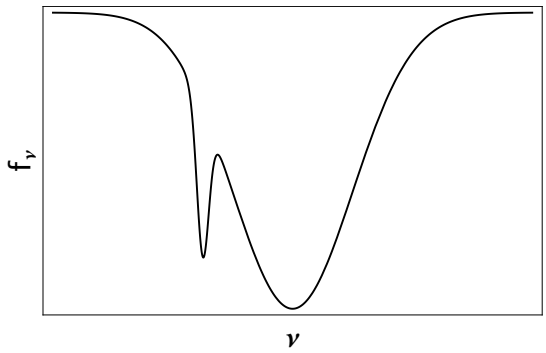

Figure 3.5: A schematic illustration of an orbiting dense spot. As the spot orbits, it covers different portions of the line of sight velocity structure. This resulted in extra absorption on top of the neutral disk profile. The feature corresponding to the dense spot travels in ν space according to $\nu_c(t)$ in equation (3.9), while the HI disk profile is stationary. For a cloud on a circular orbit, the spot absorption feature oscillates sinusoidally in frequency space. The amplitude and frequency of the oscillation can be used to simultaneously measure the spot orbital radius and the black hole mass up to a factor of $\sin i$. Note that a dense spot can exist in the absence of a disk.

where a is the semimajor axis of the orbit and

$$r(t) = \frac{a(1-e^2)}{1 + e\cos\left(\sqrt{\frac{GM}{a^3}}t\right)} \ , \tag{3.10}$$

with e being the orbital eccentricity. In addition to the inclination angle, the orbit possesses three parameters: M, a, and e (or equivalently, the orbital energy, angular momentum, and the black hole mass). If the mass of the black hole is known, the oscillation amplitude and frequency can be used to determine the orbital parameters of the cloud up to the unknown inclination factor.

3.2.4 Detectability

The signal to noise ratio of such a system is given by

$$\frac{S}{N} = \frac{\delta F_\nu}{\mathrm{SEFD}} \sqrt{2 t_o \Delta\nu} \,, \tag{3.11}$$

where SEFD is the System Equivalent Flux Density of the telescope, $\Delta\nu$ the bandwidth, t_o the observing time, and the factor of $\sqrt{2}$ results from the use of dual polarization observations. If Sgr A*'s intrinsic (unabsorbed) 21 cm flux density is $\sim$ 1 Jy, $N_H = 10^{21}$ cm^{-2}, $T_S = 8 \times 10^3$ K, $i = 80$ degrees, and $R_{ph} = 10^{15}$ cm, we find that $\delta F_\nu \sim 0.6$ mJy. The Square Kilometer Array (SKA) possesses a collecting area of 10^{10} cm^2. A system temperature of $\sim$ 50 K will then give SEFD = 0.3 Jy. Assuming $\Delta\nu \sim 10$ MHz, we obtain $S/N \gtrsim 10$ over 30 minutes of observations. We also note that the signal to noise ratio scales with column density, spin temperature, and observation time as

$$\frac{S}{N} \propto \frac{N_H}{T_S} \sqrt{t_o} \,. \tag{3.12}$$

As such, the detectability of the signal would depend on N_H and T_S of the observed system. In particular, for $i = 80$ degrees disk, the signal to noise is given by

$$\frac{S}{N} \approx 9 \left[\frac{N_H}{10^{21}\ \mathrm{cm}^{-2}} \right] \left[\frac{8 \times 10^3\ \mathrm{K}}{T_S} \right] \left[\frac{t_o}{1\ \mathrm{second}} \right]^{1/2} \,. \tag{3.13}$$

As we have no constraints on the values of N_H and T_S at the Galactic Center, the fiducial values of N_H and T_S considered are taken from observations of megamaser systems and theoretical considerations in our Galactic Center (Loeb 2008; Yusef-Zadeh & Wardle 2012). Note that the fiducial value of N_H in our calculation is modest, and column density in excess of 10^{23} cm^{-2} might be possible. The spin temperature, T_S, is even less constrained than N_H; while it could be coupled to the actual gas temperature, our model considers T_S as a free parameter that is not necessarily equal to the gas temperature. Our method promises to constrain the combination of the two parameters, N_H/T_S.

3.3 Conclusions

We have calculated the 21 cm absorption profile corresponding to a disk of neutral hydrogen around black holes. Spectroscopic measurements of a disk absorption profile can be used to determine the disk parameters, or to ascertain the presence of gaps in the disk even when the black hole-disk system is spatially unresolved. Furthermore, we demonstrated how an orbiting dense cloud of gas could also be detected through its time-dependent 21 cm absorption. In this case we delineated a method to determine the spot's orbital parameters from the absorption spectrum.

Our methodology does not require the system to be spatially resolved. While the angular size of Sgr A*'s photosphere is $\sim$ 10 milliarcseconds, interstellar blurring

could render even Sgr A* unresolveable. Interstellar absorption would also deepen the absorption profile at low velocities. However, the absorption profile near the supermassive black hole is wide, and at higher velocities ($\gtrsim$ 1000 km/s) the absorption should be purely from HI near the black hole.

While we presented results for a homogeneous neutral disk with no limb darkening, our formalism is general and could be used for systems where N_H or $I_{\nu 0}$ are nontrivial functions of the disk coordinates, or where the line function has a significant velocity width.

3.4 Acknowledgment

The authors would like to thank Mark Reid and Jim Moran for comments on the manuscript. This work was supported in part by NSF grant AST-1312034.

4

Probing the spacetime around SMBHs with ejected plasma blobs

Millimeter-wavelength VLBI observations of the supermassive black holes (SMBH) in Sgr A* and M87 by the Event Horizon Telescope could potentially trace the dynamics of ejected plasma blobs in real time. We demonstrate that the trajectory and tidal

stretching of these blobs can be used to test general relativity and set new constraints on the mass and spin of these black holes.

4.1 Introduction

The planned Event Horizon Telescope (EHT)* will possess angular resolution comparable to the Schwarzschild radius of the supermassive black holes (SMBHs), Sgr A* and the one at the center of M87, and temporal resolution on minutes timescales (Johnson et al. 2014). This is expected to open a new avenue for studying a multitude of transient phenomenae under extreme gravity.

Sgr A* is known to exhibit variability with tens of minutes timescale corresponding to accretion disk activity at the innermost stable circular orbit (ISCO) (Gillessen et al. 2009; Johnson et al. 2014). Here we study a hypothetical class of short timescale events corresponding to plasma blobs ejected near the ISCO radius. Although such blobs were never observed from a supermassive black hole, they may exist based on the analogy with microquasars, which are known to propel blobs at relativistic speeds (Mirabel et al. 1992; Mirabel 2003, 2004).

In addition to microquasars, plasma blob ejection is also observed in the Sun during coronal mass ejection (CME) events (Babu 2014; Savani et al. 2012). Microquasars and stars have very different magnetic field and gas properties, and the presence of blob ejections in both of them leads us to believe that plasma blob ejections is a

*http://www.eventhorizontelescope.org/

generic phenomenon in magnetized environments. In particular, it has been suggested that plasma ejections for both microquasars and CMEs is caused by magnetic reconnection (de Gouveia dal Pino & Lazarian 2005; Babu 2014), and in the past CME has been argued to be analogous to blob launching in microquasars (Yuan et al. 2009). Since magnetic reconnection is likely operating in the turbulent accretion disk around both Sgr A* and M87, plasma blob ejections can be expected to occur in these environments.

The second target of the EHT is the supermassive black hole at the center of the elliptical galaxy M87. In contrast to Sgr A*, M87 possesses a jet, and it is likely that blobs are ejected along the jet's symmetry axis.

In this Letter, we demonstrate that if ejected plasma blobs were detected, one could use their dynamics to probe the spacetime around the black holes. Furthermore, if the mass and spin of a given black hole are known, one can use observations of the blob's dynamics to test general relativity or infer the presence of non-gravitational sources such as gas pressure or magnetic stress. These constraints would be complimentary to constraints from pulsar timing (Pfahl & Loeb 2004; Cordes et al. 2004; Kramer et al. 2004; Psaltis & Johannsen 2011; Liu et al. 2012) or observations of the black hole shadow (Lu et al. 2014; Psaltis et al. 2015; Johannsen 2012).

There are two elements of dynamical information: the trajectory of the blob's center of mass, and its lateral expansion. Both can be used to independently constraint the black hole's spacetime. We discuss the former in §4.2 and §4.3, and the later in

	Black hole mass	Distance	Time	Space	Angle
Sgr A*	$(4.31 \pm 0.36) \times 10^6 M_\odot$	7.94 ± 0.42 kpc	21 s	0.043 AU	5.3 μas
M87	$(3.5^{+0.9}_{-0.7}) \times 10^9 M_\odot$	16.7 ± 0.9 Mpc	4.8 hr	35 AU	2.1 μas

Table 4.1: The conversion of black hole mass, M, to units of time, space, and angular size on the sky for Sgr A* and M87 (Gillessen et al. 2009; Ghez et al. 2008; Walsh et al. 2013; Eisenhauer et al. 2003; Bird et al. 2010), for $G = c = 1$.

§4.4. Throughout the discussion, we will assume general relativity. Deviations from our results would indicate the presence of non-gravitational forces or corrections to the theory of gravity. We use units where $G = c = 1$, and the conversion from these units to physical units is given in Table 4.1.

4.2 Center of Mass Motion

First we consider the motion of the blob's center of mass (COM). If the blob is ejected above the escape speed from the ISCO radius, R_{ISCO}, its azimuthal velocity will be negligibly small at $r \gg R_{ISCO}$, so we focus our discussion on the radial equation of motion. For a Schwarzschild black hole (Chandrasekhar 1983),

$$\left(\frac{dr}{d\tau}\right)^2 = \frac{2M}{r} - (1 - e^2) \quad ; \quad \frac{dt}{d\tau} = \frac{e}{1 - 2M/r} \, , \tag{4.1}$$

where M is the black hole mass, e the energy per unit rest mass of the blob, r the black hole-blob distance, t the coordinate time, and τ the blob's proper time. These two equations can be solved for dt/dr and integrated to obtain the coordinate time as

a function of the orbital radius of the blob's COM,

$$t_{Sch}(r) = \int_{R_{ISCO}}^{r} \frac{e}{\left(1 - \frac{2M}{r'}\right)\sqrt{\frac{2M}{r'} - (1 - e^2)}} dr' \ . \tag{4.2}$$

If the blob is ejected out of a Kerr black hole, a similar set of equations can be solved to obtain its COM motion in the equatorial plane,

$$t_{Kerr}(r) = \int_{R_{ISCO}}^{r} \frac{e}{\Delta} \frac{r'^2 + a^2 + \frac{2a^2M}{r'}}{\sqrt{e^2 + \frac{2Ma^2e^2}{r'^3} + \frac{a^2e^2}{r'^2} - \frac{\Delta}{r'^2}}} dr' \ , \tag{4.3}$$

where a is the black hole's spin parameter and $\Delta(r) \equiv r^2 - 2Mr + a^2$. In general, there is no reason for the blob to be ejected in the equatorial plane of the black hole, and in fact blobs should preferentially be ejected along the spin axis. But, as shown in Figure 4.1, the effect of the black hole spin is weak. At $t = 10M$, the trajectory of a blob with $e = 2$ launched from an $a = 0.999$ black hole is only $0.36M$ apart from one launched from an $a = 0$ black hole.

4.3 Ray Tracing

In simulating what would be seen by radio interferometers, we project the COM motion of the blob to the sky plane far from the black hole. We utilize the geokerr code (Dexter & Agol 2009) to trace rays from the observer plane located at infinity to the position of the blob. The coordinates (x, y) parameterize positions in this observer

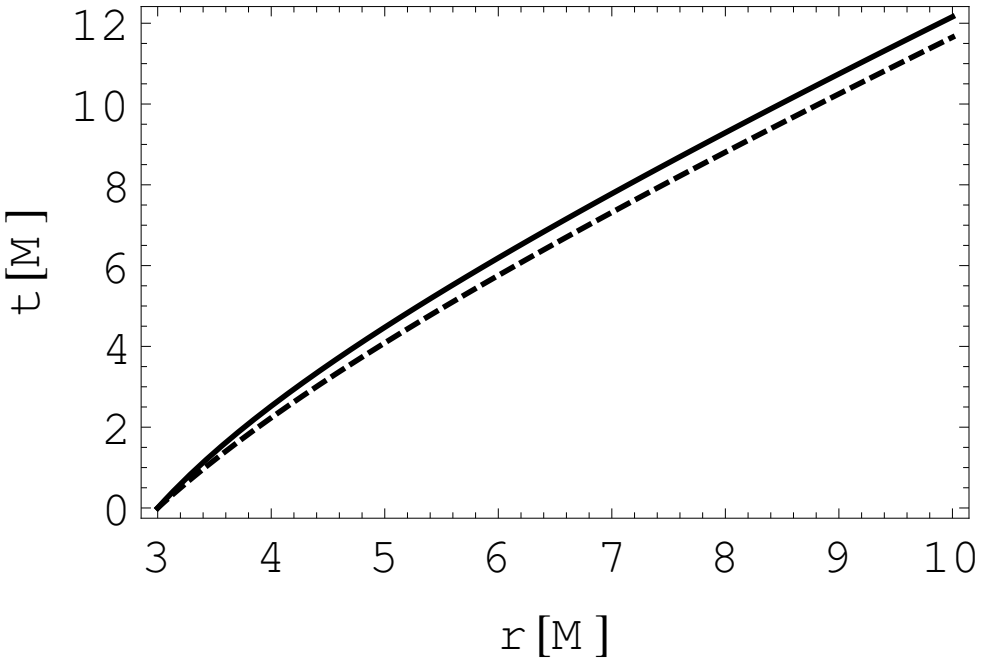

Figure 4.1: The radial motion of blobs with $e = 2$ in the equitorial plane of a black hole with $a = 0$ (solid line) and $a = 0.999$ (dotted line).

plane. The Fourier transform of this plane yields the visibility of a radio interferometer.

The blob itself is modeled as a small sphere that is emitting isotropically in its rest frame. The result for blobs with velocity vectors at angles $\theta = 0$ and $\theta = \pi/8$ away from the observer are presented in Figure 4.2. For a blob moving along the $\theta = 0$ axis, the image is briefly lensed into a ring with radius $R_{ring} \sim 5M$. Previous calculations by Johannsen & Psaltis (2010) showed that the eccentricity of this ring is not sensitive to the spin of the black hole (except for $a \approx 1$), but is very sensitive to the black hole's quadrupole moment. Thus, if detected, the ring can be used as a test of the no-hair theorem. As the ring only appears when the blob is still close to the black hole, its lifetime is short ($\sim 40M$ for a blob with $e = 10$, but longer for slower moving blobs). It is therefore necessary to have temporal resolutions on minutes timescale to detect the ring.

In addition, if the motion is fast enough and is launched at a small angle relative to the observer, the apparent trajectory can appear superluminal (e.g. Rees 1966). Close to the black hole, this apparent superluminal motion will be obscured by the bright photon ring. Thus, the detection of superluminal motion will require either waiting for the ring to dim or a manual removal of the ring.

The projected distance as a function of observed times, shown in Figure 4.3, can be compared with observations to determine the presence of non-gravitational forces (e.g. due to magnetic fields or hydrodynamic friction on background gas). In addition,

it can be used to constrain gravitational theories that predict changes on the orbit of test particles close to a black hole (e.g. Giddings 2014).

4.4 Tidal effects

If the forces holding the blob together are much smaller than the tidal gravitational forces, the blob will be tidally sheared. The magnitude of this tidal shear depends on the black hole's mass and spin, and thus can be used to probe the black hole metric. Under the approximation that the force per unit mass keeping the blob together is $\ll (2MR/r^3)$, where R is the radius of the blob, the elements of the blob can be treated as if they are moving along geodesics.

If the blob is small, we can define the geodesic deviation vector ξ^α between the geodesic followed by the particle at the center of the blob and the different geodesic followed by particles at the blob's edge by,

$$\xi^\alpha = \frac{\partial x^\alpha}{\partial s} \,, \tag{4.4}$$

where s is the parameter indexing neighboring geodesics. We can calculate the rate of change of ξ^α with respect to the affine parameter of the geodesic,

$$\frac{d}{d\tau}\xi^\alpha = u^\beta \nabla_\beta \xi^\alpha - \Gamma^\alpha_{\beta\gamma}\xi^\gamma u^\beta \tag{4.5}$$

$$= \xi^\beta \nabla_\beta u^\alpha - \Gamma^\alpha_{\beta\gamma}\xi^\gamma u^\beta \,, \tag{4.6}$$

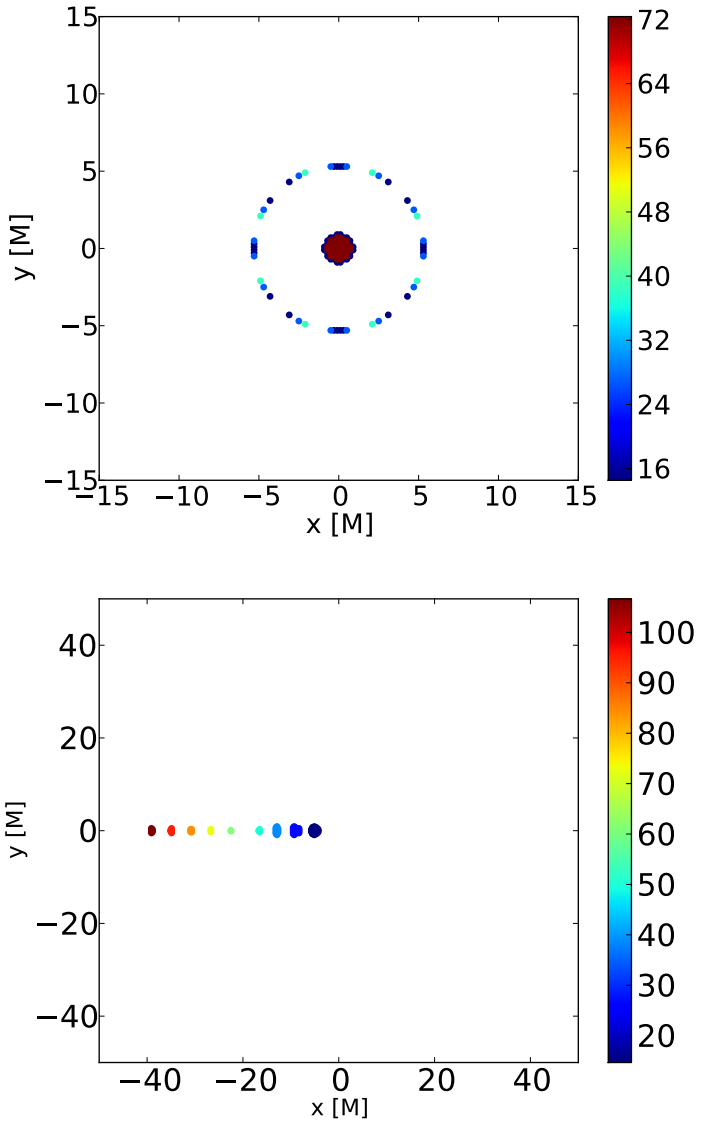

Figure 4.2: Blobs with $e = 10$ and radius M launched with $\theta = 0$ and $\theta = \pi/8$ as seen in the observer plane with the black hole located at (0,0). The observer's time axis (in units of M) is indicated by the color bar. For a blob moving with $\theta = 0$, the image is briefly lensed into a ring. The eccentricity of this ring can be used to test the no-hair theorem.

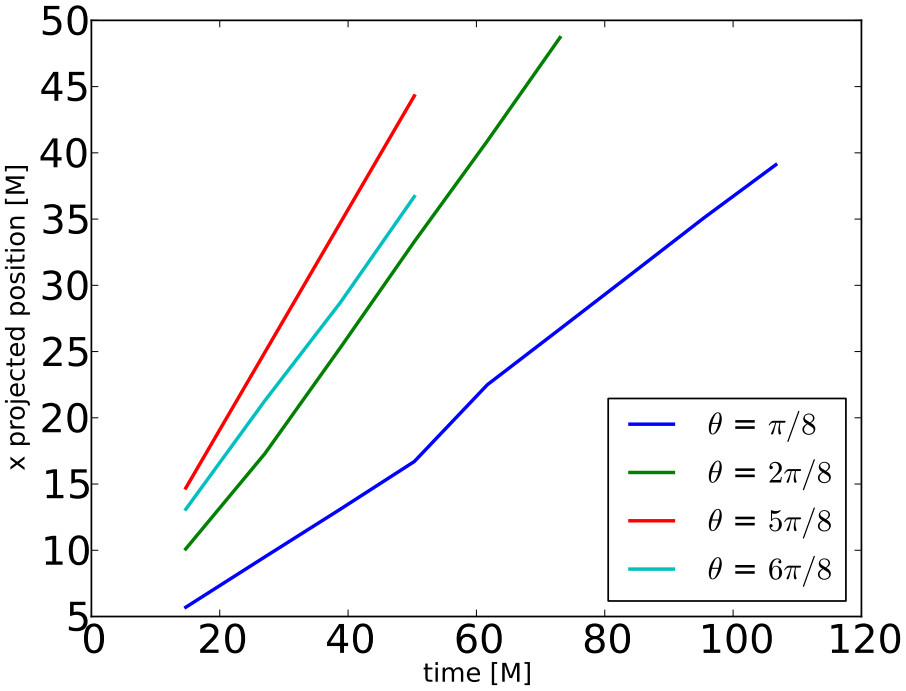

Figure 4.3: The projected position of blobs with $e = 10$ launched at a variety of angles versus observer time.

where we have used the identity (Poisson 2004),

$$u^\beta \nabla_\beta \xi^\alpha = \xi^\beta \nabla_\beta u^\alpha \tag{4.7}$$

which is valid for geodesic deviation vectors. Writing explicitly,

$$\xi^\beta \nabla_\beta u^\alpha = \xi^\beta \frac{\partial u^\alpha}{\partial x^\beta} + \Gamma^\alpha_{\beta\gamma} u^\gamma \xi^\beta \ , \tag{4.8}$$

yields

$$\frac{d}{d\tau}\xi^\alpha = \xi^\beta \frac{\partial u^\alpha}{\partial x^\beta} \ . \tag{4.9}$$

The four velocity of a blob ejected from a Schwarzschild black hole with negligible angular momentum is:

$$u^\alpha = \left(\frac{e}{1 - \frac{2M}{r}}, -\sqrt{\frac{2M}{r} - (1 - e^2)}, 0, 0 \right)^\alpha \ , \tag{4.10}$$

For relative motion between particles at the center of the blob and particles at the edge of the blob in the radial direction:

$$\xi^\alpha = (0, R, 0, 0)^\alpha \ . \tag{4.11}$$

Plugging equation (4.11) into equation (4.9) gives:

$$\frac{1}{R}\frac{dR}{d\lambda} = -\frac{M}{r^2\sqrt{-1+e^2+\frac{2M}{r}}} \,. \tag{4.12}$$

Note that substituting t for λ in equation (4.12), then taking a derivative with respect to t with $M/r \to \infty$ reproduces the tidal acceleration of Newtonian gravity: $a_{tidal} \sim MR/r^3$.

Substituting the orbital radius r in place of λ in equation (4.12) and integrating, we get:

$$\int_{R_0}^{R} \frac{dR'}{R'} = -\int_{r_0}^{r} \frac{M dr'}{r'^2\left(-1+e^2+\frac{2M}{r'}\right)} \,, \tag{4.13}$$

where $R_0 \ll r$ is the initial size of the blob and r_0 the starting orbital radius of the blob. Assuming that the blob is ejected from the ISCO radius, $r_0 = 6M$ for $a = 0$, we obtain:

$$\frac{R}{R_0} = \left[\frac{(-2+3e^2)r}{6M+3(e^2-1)r}\right]^2 \,. \tag{4.14}$$

This change in radius is in principle observable, and can therefore be used to find the mass of the black hole if e is inferred from the COM trajectory. The constant e can be inferred far away from the black hole where it obeys $e = 1/\sqrt{1-v_{COM}^2}$, where v_{COM} is the COM velocity of the blob at $r \gg M$. Figure 4.4 shows the radial growth factor for blobs with specific energy $e = 1.0001$, 1.001, 1.01, and 10. Because blobs of

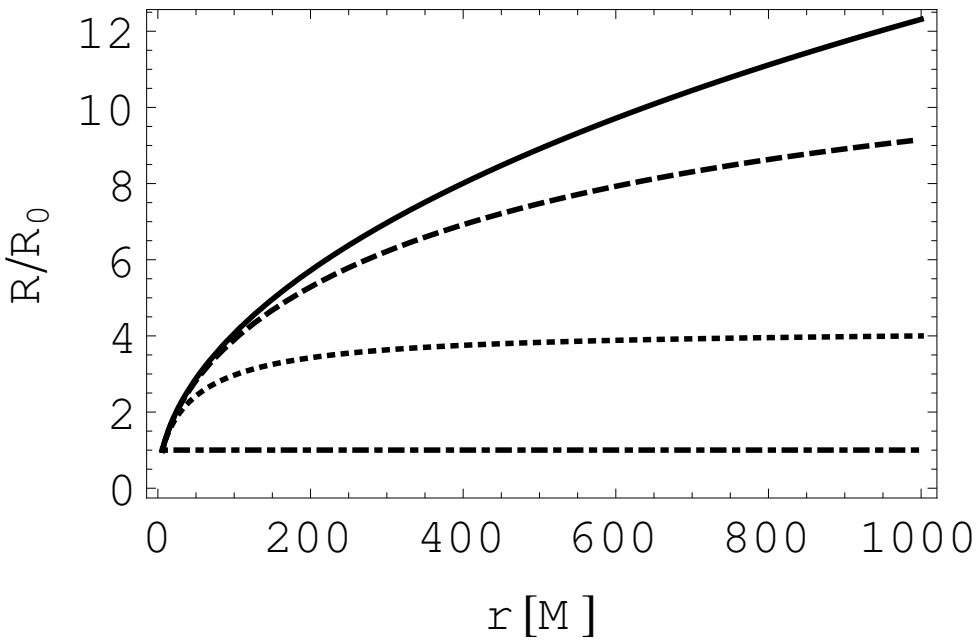

Figure 4.4: The growth factor of the blob radius due to gravitational tide as a function of distance from the black hole for a blob moving with negligible angular momentum. The blob's specific energy is $e = 1.0001$, 1.001, 1.01, and 10 for the solid, dashed, dotted lines, and dot-dashed lines, respectively.

smaller e spend more time close to the black hole, the tidal effect is larger the closer e is to unity. In the case of $e \sim 1$, one can get a growth factor of $R/R_0 \sim 10$ at $r = 1000M$. This is a change that is observable by the EHT. Assuming that the biggest source of uncertainty is in measuring R/R_0, an error propagation calculation implies that the precision of mass measured using this method is $\sim 25\%/\sqrt{N}$, where N is the number of blobs observed. This is competitive with the current measurement precision for M87 (Walsh et al. 2013). In general, one can also compute the relative motion between the center and the edge of the blob in the $\hat{\phi}$ and $\hat{\theta}$ direction via an analogous calculation.

We can extend this calculation to the case of a spinning black hole with a blob moving radially in the equatorial plane. For this configuration, the relevant components of u^α are,

$$u^t = \frac{e}{\Delta}\left(r^2 + a^2 + \frac{2a^2M}{r}\right) , \tag{4.15}$$

$$u^r = \sqrt{e^2 + \frac{2M}{r^3}(ae)^2 + \frac{a^2e^2}{r^2} - \frac{\Delta}{r^2}} . \tag{4.16}$$

Again we adopt,

$$\xi^\alpha = (0, R, 0, 0)^\alpha . \tag{4.17}$$

Performing an analogous calculation as in the $a = 0$ case, we obtain,

$$\frac{R}{R_0} = \frac{R_0\sqrt{a^2\left(-3+4e^2\right)M + 36\left(-2+3e^2\right)M^3}r^{3/2}}{6M^{3/2}\sqrt{3r^2\left[2M+\left(-1+e^2\right)r\right] + 3a^2\left[-r+e^2(2M+r)\right]}} . \tag{4.18}$$

If the mass of the black hole and the blob energy e are known, this equation can be used to measure the spin of the black hole. Figure 4.5 shows the growth factor R/R_0 for blobs with dimensionless spin parameter $a = 0,\ 0.5,$ and 1. The effect of spin is weak, and its measurement would be challenging. Again, assuming that the biggest uncertainty is in measuring R/R_0, we performed an error propagation calculation to estimate the precision of the dimensionless spin parameter, a, measured using this technique to be $\sim 0.6/\sqrt{N}$, where N is the number of blobs observed. The current

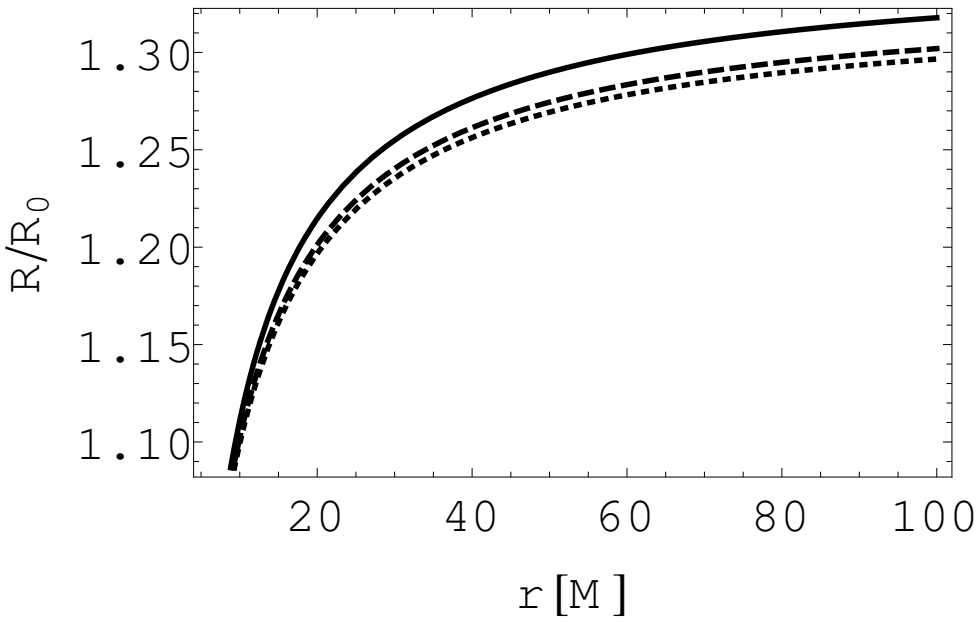

Figure 4.5: The growth factor of the blob radius as a function of distance from a spinning black hole for a blob trajectory with a negligible angular momentum. The black hole's spin is $a = 0,\ 0.5,$ and 1 for the solid, dashed, and dotted lines, respectively. The blob energy is $e = 1.2$ for all curves.

constraint on the spin parameter of M87 is $a > 0.5$ (Doeleman et al. 2012).

4.5 Conclusion

We have shown that observations of ejected plasma blobs from the supermassive black holes Sgr A* and M87, can be used to constrain the spacetime near these black holes. There are two pieces of information that can be obtained from these observations: the blob's trajectory and the tidal effects on the blob's shape.

The trajectory of the blob can be used to limit the presence of non-gravitational forces around the black hole or to constrain theories of gravity that predict anomalies

in the orbit of test particles in the vicinity of black holes (e.g. Giddings 2014). If a photon ring is detected, its eccentricity could be used as a test of the no-hair theorem. Furthermore, observations of the tidal stretching of the ejected blob can be used to determine both the mass and spin parameter of the black hole.

4.6 Acknowledgment

This work was supported in part by NSF grant AST-1312034.

5

Magnetic field probe of the no-hair theorem

We discuss the consequences of violating the no-hair theorem on magnetic fields surrounding a black hole. This is achieved by parametrically deforming the Kerr spacetime and studying the effects of such deformations on asymptotically uniform mag-

netic fields around the black hole. We compute the deformed electromagnetic field for slow spins and small deformation parameter, and show that the correction is of order the deformation parameter and mimics the angular structure of a quadrupole.

5.1 Introduction

The no-hair theorem of General Relativity (GR) states that isolated, stationary black holes are described by only three parameters: M, the mass of the black hole; J, the spin of the black hole; and Q, the charge of the black hole (Israel 1967, 1968; Carter 1971; Hawking 1972; Robinson 1975). In terms of the metric, this means that the most general black holes satisfying the no-hair theorem is the Kerr-Newman metric describing a charged, rotating black hole. However, in typical astrophysical settings, charge neutrality is expected. This reduces the metric to the Kerr metric describing an uncharged, rotating black hole, given in Boyer-Lindquist coordinates (t, r, θ, ϕ) as

$$ds^2 = -\left(1 - \frac{2Mr}{\Sigma}\right) dt^2 - \frac{4Mar\sin^2\theta}{\Sigma} dt d\phi + \frac{\Sigma}{\Delta} dr^2 + \Sigma d\theta^2 + \left(r^2 + a^2 + \frac{2Ma^2 r \sin^2\theta}{\Sigma}\right) \sin^2\theta d\phi^2 \,, \tag{5.1}$$

where $G = c = 1$, $a = J/M$, $\Sigma = r^2 + a^2\cos^2\theta$, $\Delta = r^2 - 2Mr + a^2$, and we have taken the $(-,+,+,+)$ as the metric signature.

In the derivation of the no-hair theorem, it is necessary to assume that the black hole spacetime does not possess either naked singularities or closed timelike curves outside of a horizon. Therefore, the detection of a black hole which violates the no-hair theorem implies that either GR, the Cosmic Censorship Conjecture, or the Chronologic Censorship Conjecture is invalid (Johannsen 2013).

There has been multiple proposals in the past for testing the black hole no-hair theorem, with most of them focusing on methods to observe the black hole quadrupole. For an uncharged black hole, the no-hair theorem demands that all multipole moments of the black hole depend only on M and J. In particular, the dimensionless black hole quadrupole, q is given by

$$q \equiv \frac{c^4 Q}{G^2 M^3} = -\left[\frac{cJ}{GM^2}\right]^2 , \tag{5.2}$$

where Q is the black hole's quadrupole moment, and we have reintroduced the factors of c and G. Violations of equation (5.2) causes astrophysical observables like the relativistically broadened iron lines (Johannsen & Psaltis 2013), the shape of the black hole shadow (Johannsen & Psaltis 2010), and the Shapiro delay to be modified from their Kerr counterparts (Christian et al. 2015).

In this work we propose that the magnetic field structure around the black hole will also be modified by the presence of a non-Kerr quadrupole. This change could in principle be detected by observational campaigns designed to probe magnetic fields

close to the black hole horizon (Gold et al. 2017). Furthermore, this calculation is important for testing force-free numerical computations.

In particular, we are interested in black holes immersed in an asymptotically uniform external magnetic field which shares the same symmetries of the spacetime. The magnetic field is considered to be a test field that does not affect the spacetime geometry, and is assumed to satisfy the source-free Maxwell's equations. Examples where such a condition is realized in an astrophysical setting is when a magnetar orbits a black hole within its light cylinder (D'Orazio & Levin 2013; D'Orazio et al. 2016) or for a black hole immersed in tenuous plasma (Morozova et al. 2014).

The main machinery of this work is a theorem by Wald (Wald 1974) which states that in GR the behavior of electromagnetic test fields around an asymptotically flat, axisymmetric, vacuum spacetimes is related to the spacetime Killing vectors. While this theorem has been extended to a variety of non-GR gravitational theories (Azreg-Aïnou 2016; Abdujabbarov et al. 2011; Abdujabbarov & Ahmedov 2010), we will only need the GR version here. The reason for this is twofold: first, we want to be agnostic towards the particular theoretical extension of GR; and second, it is possible that even within GR the no-hair theorem is violated (Manko & Novikov 1992). To this end we employ a metric that parametrically deforms the Kerr spacetime, and compute the effects of the deformation parameter on the test magnetic field. This approach was first attempted by Abdujabbarov et al. (2013) for the Johannsen-Psaltis (JP) metric (Johannsen & Psaltis 2011). However, the JP metric is not Ricci flat (Johannsen

2013; Johannsen & Psaltis 2011), rendering the Wald solution invalid.

The organization of this article is as follows: in §5.2 we discuss the quasi-Kerr (QK) metric, a parametric deformation of the Kerr metric that we employ in our calculation; in §5.3 we review the Wald solution; in §5.4 we compute the Wald solution for the QK metric in the Boyer-Lindquist like coordinates; in §5.5 we transform the solution to the Zero Angular Momentum Observer (ZAMO) frame; and in §5.6 we provide some concluding remarks.

5.2 The quasi-Kerr metric

The QK metric (Glampedakis & Babak 2006) is a parametric deformation of the Kerr metric given by

$$g_{\mu\nu} = g^{\rm Kerr}_{\mu\nu} + \epsilon h_{\mu\nu} \ , \tag{5.3}$$

where $g^{\rm Kerr}_{\mu\nu}$ is the Kerr metric, ϵ a small parameter, and $h_{\mu\nu}$ is given by

$$\begin{aligned}
h^{tt} &= (1-2M/r)^{-1}\left[(1-3\cos^2\theta)\mathcal{F}_1(r)\right] \ , \\
h^{rr} &= (1-2M/r)\left[(1-3\cos^2\theta)\mathcal{F}_1(r)\right] \ , \\
h^{\theta\theta} &= -r^{-2}\left[(1-3\cos^2\theta)\mathcal{F}_2(r)\right] \ , \\
h^{\phi\phi} &= -(r\sin\theta)^{-2}\left[(1-3\cos^2\theta)\mathcal{F}_2(r)\right] \ ,
\end{aligned} \tag{5.4}$$

where the coordinates (t, r, θ, ϕ) are Boyer-Lindquiest like, and the functions $\mathcal{F}_1(r)$ and $\mathcal{F}_2(r)$ are given in Appendix A of Glampedakis & Babak (2006) as

$$\mathcal{F}_1(r) = -\frac{5(r-M)}{8Mr(r-2M)}(2M^2+6Mr-3r^2) - \frac{15r(r-2M)}{16M^2}\ln\left(\frac{r}{r-2M}\right) , \quad (5.5)$$

$$\mathcal{F}_2(r) = \frac{5}{8Mr}(2M^2-3Mr-3r^2) + \frac{15}{16M^2}(r^2-2M^2)\ln\left(\frac{r}{r-2M}\right) . \quad (5.6)$$

The ϵ parameter of the QK metric modifies the quadrupole moment, Q, of the black hole into (Johannsen 2013)

$$Q = -M(a^2+\epsilon M^2) , \quad (5.7)$$

where the a^2 piece is the quadrupole moment of the standard Kerr black hole.

The QK metric is stationary and axisymmetric, admitting a timelike Killing vector η^ν and an axisymmetric Killing vector ψ^ν. Furthermore, it is asymptotically flat and satisfy the vacuum Einstein equation for low spins and small ϵ. Indeed, neglecting terms of order $O(a^2)$, $O(\epsilon a)$, and $O(\epsilon^2)$, the metric is Ricci flat (Johannsen 2013). In this article we will work exclusively in these regimes.

5.3 Wald magnetic field solution

If we immerse a black hole in an external magnetic field, the immense curvature of the spacetime modifies the magnetic field close to the black hole. If the magnetic field

is a test field (i.e. small enough to not disturb the spacetime itself), it is required to satisfy the source-free Maxwell's equations,

$$\nabla_\nu F^{\mu\nu} = 0 \ , \tag{5.8}$$

where $F^{\mu\nu}$ is the electromagnetic tensor. Wald found that for a magnetic field that is asymptotically parallel to the rotation axis of the black hole (Wald 1974),

$$\vec{B} = B_0 \hat{z} \ , \tag{5.9}$$

at spatial infinity, where $\hat{z}$ is the direction parallel to the black hole's rotation axis, the solution of the source-free Maxwell's equations is given by

$$F = \frac{1}{2} B_0 \left(d\psi + 2a d\eta \right) \ , \tag{5.10}$$

where a is the spin of the black hole, while $d\psi$ and $d\eta$ refers to the one-forms corresponding to the Killing vectors ψ^ν and η^ν, defined by

$$\eta \equiv \eta_\nu dx^\nu \ , \tag{5.11}$$

$$\psi \equiv \psi_\nu dx^\nu \ . \tag{5.12}$$

This solution is valid as long as the spacetime satisfies the vacuum Einstein equation (Ricci flat),

$$R_{\mu\nu} = 0 \ . \tag{5.13}$$

As the QK metric is Ricci flat when the spin and deformation parameter are small, we can use this method to solve the source-free Maxwell's equations for QK black holes in these regimes.

5.4 QK black hole immersed in magnetic field

In the coordinates we are using, the Killing vectors of the QK black hole is identical to the usual Kerr Killing vectors in Boyer-Lindquist coordinates,

$$\eta^{\nu} = \frac{\partial}{\partial t} \ , \tag{5.14}$$

$$\psi^{\nu} = \frac{\partial}{\partial \phi} \ . \tag{5.15}$$

Therefore, we can rewrite the Wald solution in terms of the metric components via the identifications

$$\eta_{\nu} = g_{\nu t} \ , \tag{5.16}$$

$$\psi_{\nu} = g_{\nu \phi} \ . \tag{5.17}$$

In particular, due to its dependence on $d\psi$ and $d\eta$, the electromagnetic tensor F will consist of terms proportional to derivatives of the metric $\partial_\alpha g_{\mu\nu}$.

Churning through these derivatives, we obtain the following components of F up to second order in the spin parameter a:

$$F_{tr} = -B_0 \frac{4aM(\sin^2\theta - 1)}{r^2} \,. \tag{5.18}$$

$$F_{t\theta} = B_0 \frac{8aM\cos\theta\sin\theta}{r} \,, \tag{5.19}$$

$$\begin{aligned} F_{r\phi} = {} & 2B_0 r\sin^2\theta + \epsilon B_0 \frac{5(M+r)\left[1+3\cos(2\theta)\right]}{8M^2(2M-r)}\sin^2(\theta) \\ & \times \left[2M\left(M^2-6Mr+3r^2\right) - 3r\left(2M^2-3Mr+r^2\right)\log\left(\frac{r}{-2M+r}\right)\right] \end{aligned} \tag{5.20}$$

$$\begin{aligned} F_{\theta\phi} = {} & 2B_0 r^2\sin\theta\cos\theta + \epsilon B_0 \frac{5r}{32M^2}\left[2\sin(2\theta) - 3\sin(4\theta)\right] \\ & \times \left[2M\left(2M^2-3Mr-3r^2\right) + 3r\left(-2M^2+r^2\right)\log\left(\frac{r}{-2M+r}\right)\right] \end{aligned} \tag{5.21}$$

Note that to order a^2, the electric field is identical to the Kerr solution. This is because the electric field is generated by the frame dragging of the magnetic field by the rotation of the black hole. Therefore, the electric field terms are at least of order a. Higher order corrections to the electric field due to violations of the no-hair theo-

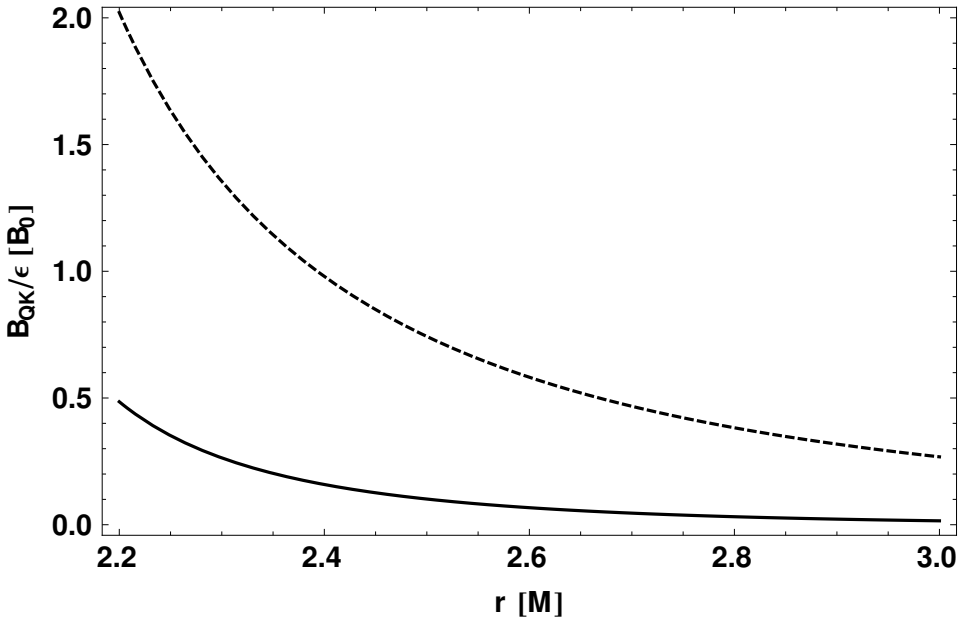

Figure 5.1: $B^{\hat{\theta}_{QK}}$ (solid) and $B^{\hat{r}_{QK}}$ (dashed) as a function of radius from the black hole for $\theta = \pi/4$. Close to the black hole, the corrections due to the quadrupole modification is of order ϵ.

rem is neglected in our approximation. As a result, the Wald charge accumulated by a slowly spinning QK black hole is identical to that of a Kerr black hole.

5.5 Fields in the ZAMO Frame

In order to obtain the electric and magnetic fields from F, a frame must be specified. To this end, we specify the Zero Angular Momentum Observer (ZAMO) frame of the QK metric up to order ϵ:

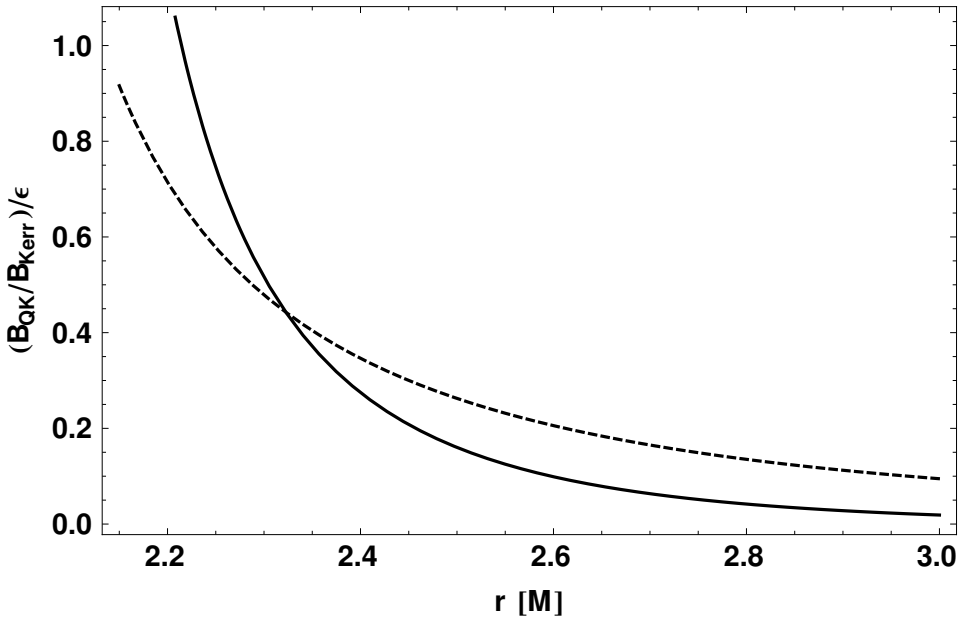

Figure 5.2: The ratio of $B^{\hat{\theta}}_{QK}$ (solid) and $B^{\hat{r}}_{QK}$ (dashed) to the Kerr solution as a function of radius from the black hole for $\theta = \pi/4$. Close to the black hole, the corrections due to the quadrupole modification can exceed that of the Kerr contribution.

$$e^{\hat{t}}_{\ t} = \sqrt{1-\frac{2M}{r}} + \epsilon \frac{5\left[-1+3\cos^2(\theta)\right]\left[-2M(M-r)\left(2M^2+6Mr-3r^2\right)+3r^2(-2M+r)^2\log\left(\frac{r}{-2M+r}\right)\right]}{32M^2\sqrt{1-\frac{2M}{r}}r^2}\,, \tag{5.22}$$

$$e^{\hat{r}}_{r} = \sqrt{\frac{r}{-2M+r}} + \epsilon \frac{5\left[-1+3\cos^2(\theta)\right]\left[2M(M-r)\left[2M^2+6Mr-3r^2\right)-3r^2(-2M+r)^2\log\left(\frac{r}{-2M+r}\right)\right]}{32M^2(-2M+r)^2\sqrt{1+\frac{2M}{-2M+r}}} \,, \tag{5.23}$$

$$e^{\hat{\theta}}_{\theta} = r - \epsilon \frac{5\left[-1+3\cos^2(\theta)\right]\left[2M\left(2M^2-3Mr-3r^2\right)+3r\left(-2M^2+r^2\right)\log\left(\frac{r}{-2M+r}\right)\right]}{32M^2} \,, \tag{5.24}$$

$$e^{\hat{\phi}}_{t} = \frac{2aM\sin^2\theta}{r^2} - \epsilon \frac{5a\left[-1+3\cos^2(\theta)\right]\left[2M\left(2M^2-3Mr-3r^2\right)+3r\left(-2M^2+r^2\right)\log\left(\frac{r}{-2M+r}\right)\right]\sin^3\theta}{16Mr^3} \,. \tag{5.25}$$

$$e^{\hat{\phi}}_{\phi} = r\sin\theta - \epsilon \frac{5\left[-1+3\cos^2(\theta)\right]\left[2M\left(2M^2-3Mr-3r^2\right)+3r\left(-2M^2+r^2\right)\log\left(\frac{r}{-2M+r}\right)\right]\sin\theta}{32M^2} \,, \tag{5.26}$$

where the hatted coordinates are that of the ZAMO frame, and all other components of $e^{\hat{\alpha}}_{\beta}$ is zero.

Projecting $F_{\mu\nu}$ to the ZAMO frame, we obtain the following

$$F_{\hat{\mu}\hat{\nu}} = F^{\text{Kerr}}_{\hat{\mu}\hat{\nu}} + \epsilon F^{QK}_{\hat{\mu}\hat{\nu}} \ , \tag{5.27}$$

where the quasi-Kerr components $F^{QK}_{\hat{\mu}\hat{\nu}}$ are given by

$$F^{QK}_{\hat{r}\hat{\phi}} = -B^{\hat{\theta}}_{QK} = -\frac{5B_0\sqrt{\frac{1}{-2M+r}}\left[1+3\cos(2\theta)\right]\sin\theta}{16M^2r^{3/2}}\left[2M(M-3r)\left(5M^2+3Mr-3r^2\right)\right.$$
$$\left.+3r\left(-6M^3+M^2r+7Mr^2-3r^3\right)\log\left(\frac{r}{-2M+r}\right)\right] \ , \tag{5.28}$$

$$F^{QK}_{\hat{\theta}\hat{\phi}} = B^{\hat{r}}_{QK} = \frac{15B_0\cos\theta\sin^2\theta\left[2M\left(2M^2-3Mr-3r^2\right)+3r\left(-2M^2+r^2\right)\log\left(\frac{r}{-2M+r}\right)\right]}{8M^2r} \ , \tag{5.29}$$

where $B^{\hat{\theta}_{QK}}$ and $B^{\hat{r}}_{QK}$ are the $\hat{\theta}$ and $\hat{r}$ components of the magnetic field three-vector in the ZAMO frame. We plotted these components as a function of distance from the black hole in Figure 5.1 for $\theta = \pi/4$. We also plot the ratio between the QK components and the Kerr component in Figure 5.2 to show that there are points close to the black hole where the QK components of the magnetic field become as large as that of the Kerr component. Note that this does not invalidate our approximation of working

in the limit where ϵ is a small parameter, as we do not impose that B_{QK} is small, but rather that $\epsilon h_{\mu\nu}$ is small compared to $g^{\text{Kerr}}_{\mu\nu}$.

In order to present our result in an invariant way, we calculate the electromagnetic invariant

$$I \equiv \frac{1}{2} F^{\mu\nu} F_{\mu\nu} = B^2 - E^2 \,, \tag{5.30}$$

of the ϵ part of the solution as a function of angle and distance from the black hole and plotted them in Figure 5.3. From the angular structure of I, the quadrupolar nature of the electromagnetic field is revealed.

5.6 Conclusion

We computed the asymptotically uniform magnetic field solution for a black hole that is parametrically deformed from Kerr spacetime using the Wald formalism. We showed that no-hair deformations of the spacetime generates extra fields of strength $\sim \epsilon$ that mimics the quadrupolar structure of the spacetime. Finally, we would like to note that our solution can be transformed to that of an asymptotically uniform electric field by simply taking a Hodge dual of $F_{\mu\nu}$.

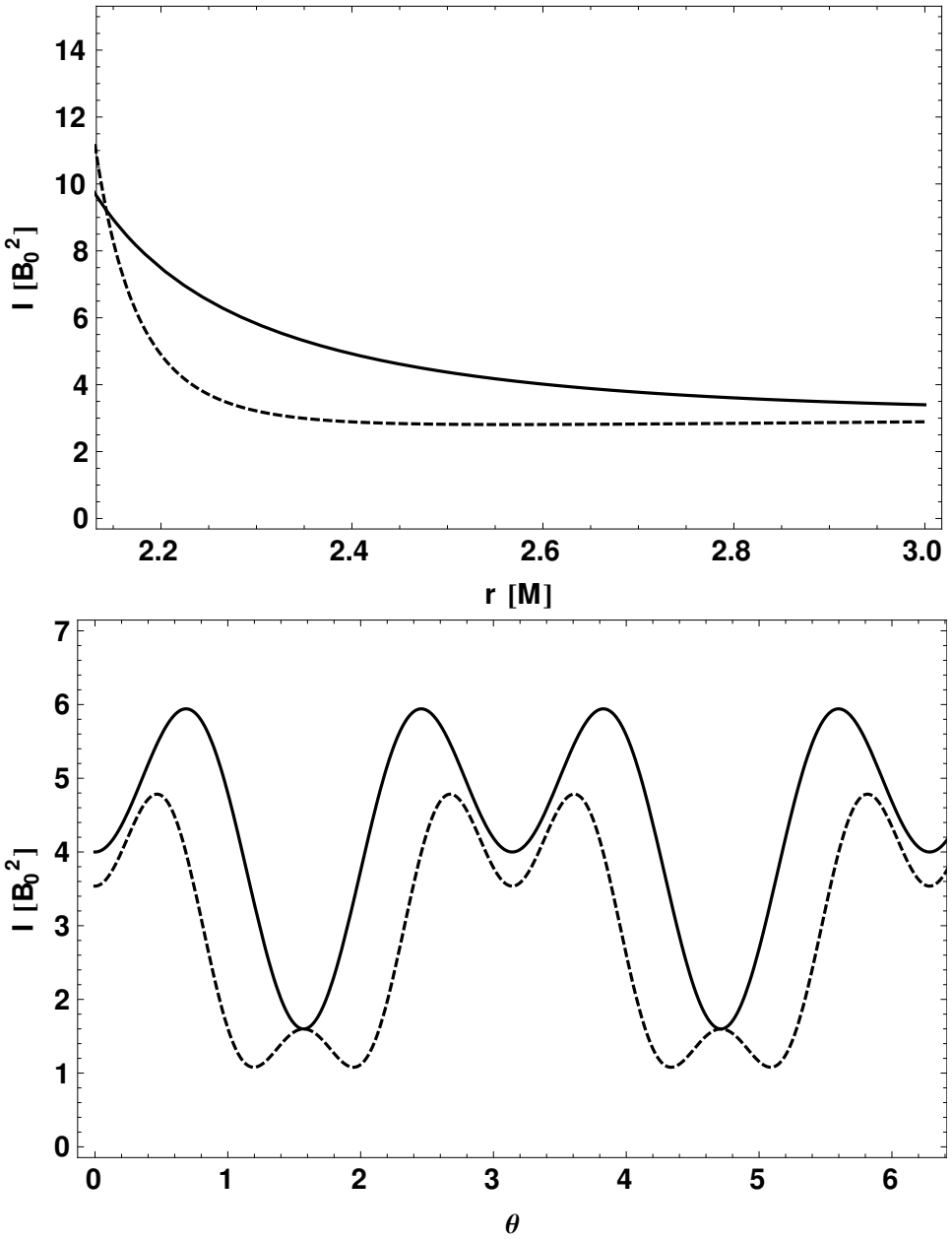

Figure 5.3: The electromagnetic invariant $I = \frac{1}{2}F^{\mu\nu}F_{\mu\nu} = B^2 - E^2$ as a function of distance from the black hole and angle for $a = 0$ (solid) and $a = 0.9$ (dashed). The quadrupolar nature of the electromagnetic field is revealed by the angular structure of I.

6

Shapiro delay tests of the Kerr spacetime using pulsars

One avenue for testing the Kerr spacetimes of astrophysical black holes is obtained through timing a pulsar orbiting close to a black hole and fitting for the properties of the Kerr metric on the time-of-arrival of pulses. To this end, we derive an expression

for the light travel time delay for a pulsar orbiting in a black-hole spacetime described by the Butterworth-Ipser metric, which has an arbitrary spin and a free parameter β which can be used to parameterize deviations of the metric from Kerr. We consider terms up to second order in (GM/rc^2), where M is the black hole mass and r the distance from the black hole, and derive the time-delay expression in a closed analytic form. This allows for fast computations that are useful in fitting time-of-arrival observations of pulsars orbiting close to astrophysical black holes. We apply our results to pulsars in circular orbits to determine possible signatures of deviations from the Kerr metric in the pulsar time delay.

6.1 Introduction

The no-hair theorem of general relativity Israel (1967, 1968); Carter (1971); Hawking (1972); Robinson (1975) states that the metric of an electromagnetically neutral black hole depends only on its mass, M, and its angular momentum, S. If it is found to be violated, one of the following possibilities must occur: either the theory of general relativity needs to be modified, or one of our assumptions regarding black-hole solutions to the Einstein equation is invalid (e.g., the cosmic censorship conjecture or the non-existence of closed timelike curves).

While so far there is an agreement between astrophysical observations and the no-hair theorem, in the near future higher observational precision via the analysis of

of-arrival (TOA) analysis of pulsars (Wex & Kopeikin 1999) orbiting close to the supermassive black hole, Sgr A*, at the center of the Milky Way (Pfahl & Loeb 2004; Cordes et al. 2004; Liu et al. 2012) might challenge this statement. The recent discovery of PSR J1745−2900, a magnetar orbiting close to Sgr A* (Kennea et al. 2013; Mori et al. 2013; Eatough et al. 2013b; Shannon & Johnston 2013), generated further interest towards this possibility. While PSR J1745−2900 is both too unstable for precise time delay measurements (Kaspi et al. 2014) and located too far from the black hole for relativistic effects to be significant*, the cluster of stars around Sgr A* should still harbor a significant number of pulsars (Pfahl & Loeb 2004; Cordes et al. 2004; Wharton et al. 2012; Chennamangalam & Lorimer 2014; Psaltis et al. 2016).

The biggest drawback in calculating the Shapiro time delay for arbitrary spacetimes is related to the fact that the presence of a Carter-like constant is, in general, not guaranteed. Unlike the case for Petrov-type D spacetimes, such as the Kerr metric, the Hamilton-Jacobi equation is not separable and the null geodesic motion is challenging to solve. For discussions on the deflection of light by quadrupoles, we refer the reader to (Kopeikin et al. 1999; Kopeikin & Makarov 2007). Moreover, testing the no-hair theorem of black holes (especially when dealing with near-horizon tests) requires using special spacetimes that do not have any pathologies near the horizon. In order to avoid pathologies, such spacetimes do not have necessarily the same behav-

*Astrophysical implications of timing delays of pulsars at large distances from their black holes have been considered in a previous work (Christian & Loeb 2015).

ior as Parametrized Post-Newtonian (PPN) metrics at the second or higher order Johannsen (2013).

In this paper we took a different approach and instead start with the general axis-symmetric family of Ricci flat metrics first discussed by Butterworth & Ipser Butterworth & Ipser (1975) of which the Kerr metric is a particular solution. By changing the Butterworth & Ipser parameters of the Kerr metric, we can deform the black hole and calculate the the effect of such deformations on the orbits of null geodesics.

This deformed metric will not necessarily possess a Carter-like constant, so directly solving the Hamilton-Jacobi equation for the light rays is difficult. However, Ref. Teyssandier & Le Poncin-Lafitte (2008) showed that the coordinate travel time for a null geodesic obeys a Hamilton-Jacobi like equation of motion that allows for the solution to be written in terms of iterative integrals (see Klioner & Kopeikin (1992); Kopeikin (1997); Kopeikin et al. (2006) for a different approach to integrating null geodesics). In this paper, we use this iterative approach to obtain an expression describing the time delay of light as it propagates in the vicinity of a black hole up to second order in GM/rc^2. For the Butterworth & Ipser metric, we obtain an expression that is analytical and allows for fast calculations to be performed.

6.2 Calculations

6.2.1 The metric and inverse metric to second order

Any asymptotically flat metric that is both stationary and axisymmetric can be written up to order $(GM/rc^2)^2$ in the quasi-isotropic coordinates (t, r, θ, ϕ) as (AlGendy & Morsink 2014; Butterworth & Ipser 1975),

$$g_{tt} = -1 + \frac{2GM}{rc^2} - 2\left(\frac{GM}{rc^2}\right)^2 + \mathcal{O}\left[\left(\frac{GM}{rc^2}\right)^3\right] , \tag{6.1}$$

$$g_{rr} = 1 + \frac{2GM}{rc^2} + \left(\frac{3}{2} - 2\beta + 4\beta\cos^2\theta\right)\left(\frac{GM}{rc^2}\right)^2 + \mathcal{O}\left[\left(\frac{GM}{rc^2}\right)^3\right] , \tag{6.2}$$

$$g_{\phi\phi} = r^2\sin^2\theta + r^2\sin^2\theta\frac{2GM}{rc^2} + r^2\sin^2\theta\left(\frac{3}{2} + 2\beta\right)\left(\frac{GM}{rc^2}\right)^2 + \mathcal{O}\left[\left(\frac{GM}{rc^2}\right)^3\right] , \tag{6.3}$$

$$g_{\phi t} = -2\frac{a_* GM^2}{r^3c^2}r^2\sin^2\theta\left(1 + \frac{GM}{rc^2}\right) + \mathcal{O}\left[\left(\frac{GM}{rc^2}\right)^3\right] , \tag{6.4}$$

$$g_{\theta\theta} = r^2 g_{rr} \tag{6.5}$$

where $a_* \equiv cS/(GM^2)$ and, following AlGendy & Morsink (2014), we have defined

$$\beta \equiv (1/4) + \tilde{B}_0/M^2 , \tag{6.6}$$

as the dimensionless parameter characterizing the black-hole where $\tilde{B}_0$ is a multipole of Ref. (Butterworth & Ipser 1975). Notably, for the Kerr metric, and thus for black

holes obeying the no-hair theorem (Pappas & Apostolatos 2012),

$$\beta_{\rm Kerr} = a_\star^2 \, . \tag{6.7}$$

Our approach in this paper is to take the metric equation (6.1)-(6.5) as an ansatz and to identify the deviation of the parameter β from $\beta_{\rm Kerr}$ as an indication of the violation of the no-hair theorem. Note that the parameter β is a parameter with a known value in the Kerr metric that can obtain different values in a different theory of gravity that possesses black holes disobeying the no-hair theorem.

We will now convert this to Cartesian coordinates, set $G = c = 1$, use geometric units (so that distances and times are measured in units of M), and write the metric order by order. To first order, we get

$$g_{tt}^{(1)} = g_{xx}^{(1)} = g_{yy}^{(1)} = g_{zz}^{(1)} = \frac{2}{\sqrt{x^2+y^2+z^2}} \, , \tag{6.8}$$

where the contravariant metric to first order

$$g_{(1)}^{\mu\nu} = \eta^{\mu\alpha}\eta^{\nu\beta} g_{\alpha\beta}^{(1)} \, , \tag{6.9}$$

gives identical components. Similarly, the second order metric $g^{(2)}_{\mu\nu}$ is

$$g^{(2)}_{tt} = -\frac{2}{(x^2+y^2+z^2)} \,, \tag{6.10}$$

$$g^{(2)}_{xt} = \frac{2a_* y}{(x^2+y^2+z^2)^{3/2}} \,, \tag{6.11}$$

$$g^{(2)}_{yt} = -\frac{2a_* x}{(x^2+y^2+z^2)^{3/2}} \,. \tag{6.12}$$

$$g^{(2)}_{xy} = -\frac{4xy\beta}{(x^2+y^2+z^2)^2} \,, \tag{6.13}$$

$$g^{(2)}_{xx} = \frac{\left[x^2(3-4\beta) + \left(y^2+z^2\right)(3+4\beta)\right]}{2\left(x^2+y^2+z^2\right)^2} \,, \tag{6.14}$$

$$g^{(2)}_{yy} = \frac{\left[y^2(3-4\beta) + \left(x^2+z^2\right)(3+4\beta)\right]}{2\left(x^2+y^2+z^2\right)^2} \,, \tag{6.15}$$

$$g^{(2)}_{zz} = \frac{\left[(x^2+y^2)(3-4\beta) + z^2(3+4\beta)\right]}{2\left(x^2+y^2+z^2\right)^2} \,. \tag{6.16}$$

and the contravariant metric to second order

$$g^{\mu\nu}_{(2)} = \eta^{\mu\alpha}\eta^{\nu\beta}g^{(2)}_{\alpha\beta} + \eta^{\mu\alpha}g^{(1)}_{\alpha\beta}g^{\beta\nu}_{(1)} \tag{6.17}$$

becomes

$$g^{tt}_{(2)} = -\frac{6}{(x^2+y^2+z^2)} \ , \tag{6.18}$$

$$g^{xt}_{(2)} = -\frac{2a_* y}{(x^2+y^2+z^2)^{3/2}} \ , \tag{6.19}$$

$$g^{yt}_{(2)} = \frac{2a_* x}{(x^2+y^2+z^2)^{3/2}} \ , \tag{6.20}$$

$$g^{xy}_{(2)} = -\frac{4xy\beta}{(x^2+y^2+z^2)^2} \ , \tag{6.21}$$

$$g^{xx}_{(2)} = \frac{\left[x^2(11-4\beta) + \left(y^2+z^2\right)(11+4\beta)\right]}{2\left(x^2+y^2+z^2\right)^2} \ , \tag{6.22}$$

$$g^{yy}_{(2)} = \frac{\left[y^2(11-4\beta) + \left(x^2+y^2\right)(11+4\beta)\right]}{2\left(x^2+y^2+z^2\right)^2} \ , \tag{6.23}$$

$$g^{zz}_{(2)} = \frac{\left[\left(x^2+y^2\right)(11-4\beta) + z^2(11+4\beta)\right]}{2\left(x^2+y^2+z^2\right)^2} \ . \tag{6.24}$$

The geodesic equation involves terms, via the Christoffel symbols, that are of second order in the metric and its derivatives. As such, the equation for the null geodesics to second order will, in principle, involve terms that are proportional to M and M^2 (describing the effects of mass), to a_* and a_*^2 (describing frame dragging), to β, and cross terms proportional to $a_* M$.

6.2.2 Parametrization of the pulsar orbit

In this paper, we concentrate on the effect of the black-hole metric on the light propagation and treat the pulsar orbit parametrically. Relativistic effects on the orbit,

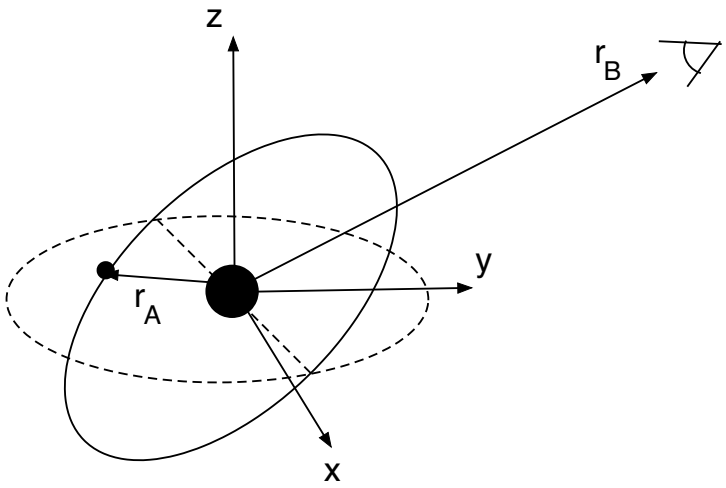

Figure 6.1: The geometry used in the calculation. The z-axis of the coordinate system is aligned with the spin of the black hole, the position vector of the pulsar is $\mathbf{r}_A$, and the position vector of the distant observer is $\mathbf{r}_B$ and lies on the $y-z$ plane.

calculated in Refs. Wex & Kopeikin (1999); Liu et al. (2012), can be added to our calculation to lowest order by adding time dependences on the orbital parameters. To focus on the effects of the time delays along geodesics, we also neglect phenomena that arise from the velocity of the pulsar.

In the following, we will set a Cartesian coordinate systems centered on the black hole, with the $z-$axis parallel to the black-hole angular momentum vector (see Figure 6.1). We also set the y-axis such that the line connecting the black hole and the observer lies on the $y-z$ plane (even though we write our expression in a general vector notation that allows for an arbitrary orientation of the observer). We focus our discussion on the light propagation delay from the pulsar at position $\mathbf{r}_A$ to the observer at $\mathbf{r}_B$.

For a pulsar in an eccentric orbit with semi-major axis a and eccentricity e, the magnitude of the distance between the pulsar and black hole at an orbital phase corresponding to a true anomaly ν is given by

$$r_A = \frac{a(1-e^2)}{1+e\cos\nu}\,, \tag{6.25}$$

while the direction of the vector $\mathbf{r}_A$ is given by

$$\hat{n}_A \equiv \frac{\mathbf{r}_A}{r_A} = \mathbf{R_z}(\Omega)\mathbf{R_y}(i)\mathbf{R_z}(\nu)\mathbf{R_z}(\omega)\mathbf{R_y}(-i)\cdot\begin{pmatrix}0\\1\\0\end{pmatrix}\,, \tag{6.26}$$

where we have made use of the following definitions for the rotation matrices

$$\mathbf{R_y}(\theta) \equiv \begin{pmatrix}\cos\theta & 0 & \sin\theta\\ 0 & 1 & 0\\ -\sin\theta & 0 & \cos\theta\end{pmatrix}\,, \quad \mathbf{R_z}(\theta) \equiv \begin{pmatrix}\cos\theta & -\sin\theta & 0\\ \sin\theta & \cos\theta & 0\\ 0 & 0 & 1\end{pmatrix}\,. \tag{6.27}$$

In this expression, ω is the argument of periapsis, Ω is the longitude of the ascending node, and i is the inclination of the orbit with respect to the black hole spin.

Our expressions will depend on the angle between $\mathbf{r}_A$ and $\mathbf{r}_B$, which we will leave expressed as the dot product $\mathbf{n}_A \cdot \mathbf{n}_B$, where $\mathbf{n}_B \equiv \mathbf{r}_B/r_B$. For most of the numerical examples shown in the figures, we will set, for simplicity, the observer along the y axis,

such that

$$\mathbf{n}_A \cdot \mathbf{n}_B = \hat{y} \cdot \hat{n}_A = \begin{pmatrix} 0 & 1 & 0 \end{pmatrix} \cdot \hat{n}_A \, . \tag{6.28}$$

We further define the geometric distance between $\mathbf{r}_A$ and $\mathbf{r}_B$ as

$$R_{AB} \equiv \sqrt{r_A^2 + r_B^2 - 2 r_A r_B \mathbf{n}_A \cdot \mathbf{n}_B} \, . \tag{6.29}$$

6.2.3 The first order Shapiro delay

Because arbitrary stationary, axisymmetric spacetimes do not generally admit a fourth constant of motion, solving analytically the null geodesic equation of motion is difficult. However, it was recently observed by Ref. Teyssandier & Le Poncin-Lafitte (2008) that the coordinate time travelled by light rays obeys Hamilton-Jacobi like equations that allows the light propagation time delay to be written in terms of iterative integrals. In particular, the propagation time delay to first order is given by (Teyssandier & Le Poncin-Lafitte 2008)

$$\Delta^{(1)}(\mathbf{r}_A, \mathbf{r}_B) = \frac{1}{2} R_{AB} \int_0^1 \left[g^{00}_{(1)} - 2 N^i_{AB} g^{0i}_{(1)} + N^i_{AB} N^j_{AB} g^{ij}_{(1)} \right]_{\mathbf{z}_+(\mu)} d\mu \, , \tag{6.30}$$

where $N^i_{AB} = (r^i_B - r^i_A)/R_{AB}$ and $\mathbf{z}_+(\mu) = \mathbf{r}_A + \mu(\mathbf{r}_B - \mathbf{r}_A)$.

Looking at the contravariant metric to first order, we can identify the first and last term as the well known Shapiro delay effect for non-rotating bodies (up to order 1).

This is given by (Shapiro 1964; Teyssandier & Le Poncin-Lafitte 2008)

$$\Delta^{(1)}(\mathbf{r}_A, \mathbf{r}_B) \equiv \int_0^1 \left[g^{00}_{(1)} + N^i_{AB} N^j_{AB} g^{ij}_{(1)} \right]_{\mathbf{z}_+(\mu)} d\mu$$
$$= 2 \log \left(\frac{r_A + r_B + R_{AB}}{r_A + r_B - R_{AB}} \right) , \tag{6.31}$$

where r_A and r_B are the magnitudes of $\mathbf{r}_A$ and $\mathbf{r}_B$ respectively.

In this section, we will express the magnitudes of the various effects on the Shapiro delays in terms of their dependences on the Euclidian distance of closest approach to the light ray from the black hole

$$r_c = \frac{r_A r_B}{R_{AB}} |\mathbf{n}_A \times \mathbf{n}_B| \, . \tag{6.32}$$

We, therefore, rewrite equation (6.31) as

$$\Delta^{(1)}(\mathbf{r}_A, \mathbf{r}_B) \approx 2 \log \left(\frac{r_c + r_A \mathbf{n}_A \times \mathbf{n}_B}{r_c - r_A \mathbf{n}_A \times \mathbf{n}_B} \right) , \tag{6.33}$$

where we used the approximation that for astronomical applications, $r_A << r_B$. This shows explicitly the known fact that the magnitude of the first order Shapiro delay is logarithmic in r_c.

6.2.4 The second order time delay

The second order contribution to the light time travel delay is given by Teyssandier & Le Poncin-Lafitte (2008)

$$\Delta^{(2)}(\mathbf{r}_A, \mathbf{r}_B) = \frac{1}{2} R_{AB} \int_0^1 \left\{ \left[g^{00}_{(2)} - 2 N^i_{AB} g^{0i}_{(2)} + N^i_{AB} N^j_{AB} g^{ij}_{(2)} \right]_{\mathbf{z}_+(\mu)} \right.$$
$$\left. + 2 \left[N^j_{AB} g^{ij}_{(1)} \right]_{\mathbf{z}_+(\mu)} \frac{\partial \Delta^{(1)}}{\partial x^i}(\mathbf{x}_A, \mathbf{z}_+(\mu)) + \eta^{ij} \left[\frac{\partial \Delta^{(1)}}{\partial x^i} \frac{\partial \Delta^{(1)}}{\partial x^j} \right]_{(\mathbf{x}_A, \mathbf{z}_+(\mu))} \right\} d\mu \, . \tag{6.34}$$

This includes terms that are of second order in the mass and spin of the black hole, as well as terms that are of first order in the parameter β. As such, it describes the second order corrections to the Shapiro time delays, the increase in the light paths because of gravitational lensing, as well as the cross terms between these effects. In this section we obtain analytical forms for this second order time delay for spinning black holes with arbitrary β parameters.

Mass contribution

We will first consider the second order mass terms in equation (6.34). These are the terms in the second line of equation (6.34) together with the $g^{00}_{(2)}$ term in the first line. These terms are identical to those evaluated in Ref.(Teyssandier & Le Poncin-Lafitte

2008; Brumberg 1987), i.e.,

$$\begin{aligned}\Delta^{(2)}_{\text{mass}} = \frac{1}{2}R_{AB}\int_0^1 \Big\{ & g^{00}_{(2)} + N^i_{AB}N^j_{AB}g^{ij}_{(2),M} \\ & 2\left[N^j_{AB}g^{ij}_{(1)}\right]_{\mathbf{z}_+(\mu)}\frac{\partial\Delta^{(1)}}{\partial x^i}(\mathbf{x}_A,\mathbf{z}_+(\mu)) + \eta^{ij}\left[\frac{\partial\Delta^{(1)}}{\partial x^i}\frac{\partial\Delta^{(1)}}{\partial x^j}\right]_{(\mathbf{x}_A,\mathbf{z}_+(\mu))}\Big\} d\mu \\ = \frac{1}{2}R_{AB}&\left[\frac{15\arccos(\mathbf{n}_A\cdot\mathbf{n}_B)}{2r_Ar_B\sqrt{1-(\mathbf{n}_A\cdot\mathbf{n}_B)^2}} - \frac{8}{r_Ar_B(1+\mathbf{n}_A\cdot\mathbf{n}_B)}\right] .\end{aligned} \tag{6.35}$$

Here, $g^{ij}_{(2),M}$ refers to the mass contribution to the spatial metric, i.e., the terms that are not proportional to the parameter β. Equation (6.35) takes into account the effect of gravitational lensing on the Shapiro delay. Writing this second order mass contribution as

$$\Delta^{(2)}_{\text{mass}} = \frac{|\mathbf{n}_A\times\mathbf{n}_B|}{r_c}\left[\frac{15\arccos(\mathbf{n}_A\cdot\mathbf{n}_B)}{4\sqrt{1-(\mathbf{n}_A\cdot\mathbf{n}_B)^2}} - \frac{4}{(1+\mathbf{n}_A\cdot\mathbf{n}_B)}\right] , \tag{6.36}$$

we find that this effect is of order $1/r_c$.

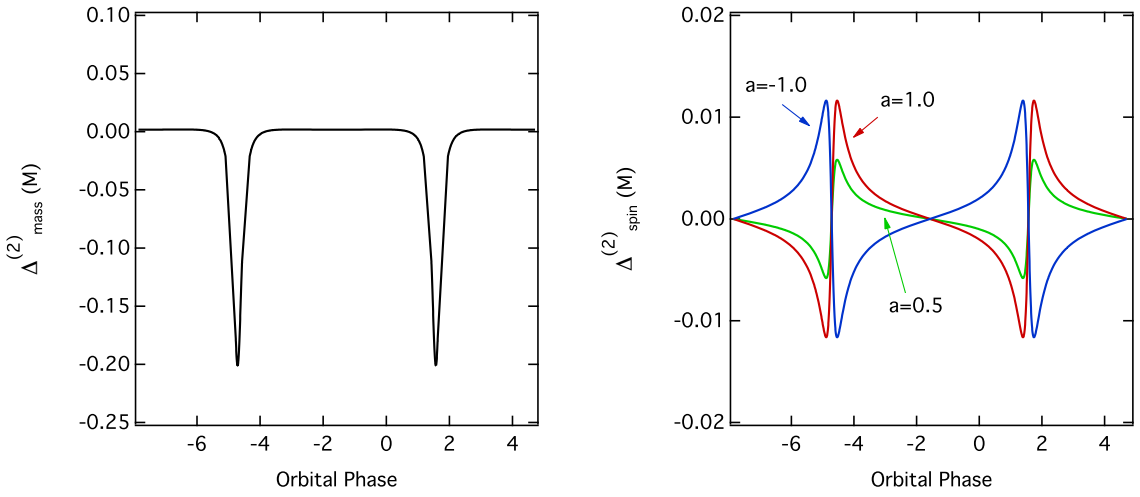

Figure 6.2: The second-order contribution due to (Left) lensing and (Right) frame dragging to the light travel time delay for a pulsar in a circular orbit around a spinning black hole, as a function of orbital phase. The green and red lines in the right panel correspond to black-hole spins of $a = 0.5$ and $a = 1$, respectively, whereas the blue line corresponds to a black hole spinning at $a = 1$ but in the opposite sense with respect to the pulsar orbit. In both panels, the pulsar orbital radius is $1000M$ and its inclination is 80 degrees; the observer is set on the equatorial plane of the black hole; superior conjunction occurs at an orbital phase of $\pi/2$.

Spin contribution

The spin contribution to the second order light propagation delay is given by

$$\Delta^{(2)}_{\rm spin}(\mathbf{r}_A, \mathbf{r}_B) = \frac{1}{2} R_{AB} \int_0^1 \left[-2 N^i_{AB} g^{0i}_{(2)} \right]_{\mathbf{z}_+(\mu)} d\mu \tag{6.37}$$

$$= -\int_0^1 \left[(x_B - x_A) \frac{2a_* y}{(x^2+y^2+z^2)^{3/2}} - (y_B - y_A) \frac{2a_* x}{(x^2+y^2+z^2)^{3/2}} \right] d\mu \, . \tag{6.38}$$

Replacing y and x with $y = y_A + \mu(y_B - y_A)$ and $x = x_A + \mu(x_B - x_A)$, we obtain

$$\Delta^{(2)}_{\text{spin}}(\mathbf{r}_A, \mathbf{r}_B) = -\int_0^1 a_* \left[\frac{-2x_B y_A + 2x_A y_B}{(x^2+y^2+z^2)^{3/2}}\right] d\mu \,. \tag{6.39}$$

In order to perform this integral, we follow the integration scheme of Ref.Teyssandier (2014) with a small modification. We rotate the coordinate axis to the plane defined by $\mathbf{r}_A$ and $\mathbf{r}_B$.

$$|\mathbf{z}_+(\mu)| = \sqrt{(x^2+y^2+z^2)} = \frac{r_c}{\cos(\gamma - \gamma_c)}, \tag{6.40}$$

where γ is the angle between $\mathbf{r}_A$ and $\mathbf{r}_B$ (defined to be 0 at $\mathbf{r}_B$) and γ_c is the angle to the point of closest approach. With these expressions and noting that the differential can be expressed as

$$d\mu = \frac{|\mathbf{z}_+(\mu)|^2}{r_c R_{AB}} d\gamma \,, \tag{6.41}$$

the integral becomes

$$\int_0^1 \frac{d\mu}{(x^2+y^2+z^2)^{3/2}} = \int_0^1 \frac{d\mu}{|\mathbf{z}_+|^3} = \int_{\gamma_A}^{\gamma_B} \frac{\cos(\gamma - \gamma_c)}{r_c^2 R_{AB}} d\gamma = \frac{r_A + r_B}{r_c^2 R_{AB}^2}(1 - \mathbf{n}_A \cdot \mathbf{n}_B) \,. \tag{6.42}$$

Incorporating this to equation (6.39), we obtain the second order spin correction to the propagation time delay,

$$\Delta^{(2)}_{\text{spin}}(\mathbf{r}_A, \mathbf{r}_B) = 2a_*(x_B y_A - x_A y_B)\left[\frac{r_A + r_B}{r_A^2 r_B^2}\frac{(1 - \mathbf{n}_A \cdot \mathbf{n}_B)}{|\mathbf{n}_A \times \mathbf{n}_B|^2}\right] \,. \tag{6.43}$$

We can obtain the magnitude of the effect described by this equation by noting that

$$(x_B y_A - x_A y_B) = r_A r_B [\mathbf{n}_B - (\mathbf{n}_B \cdot \hat{z})\hat{z}] \times [\mathbf{n}_A - (\mathbf{n}_A \cdot \hat{z})\hat{z}] \,, \tag{6.44}$$

allowing us to rewrite equation (6.43) as

$$\Delta^{(2)}_{\rm spin}(\mathbf{r}_A, \mathbf{r}_B) \approx \frac{2a_*}{r_c} \frac{[\mathbf{n}_B - (\mathbf{n}_B \cdot \hat{z})\hat{z}] \times [\mathbf{n}_A - (\mathbf{n}_A \cdot \hat{z})\hat{z}](1 - \mathbf{n}_A \cdot \mathbf{n}_B)}{\mathbf{n}_A \times \mathbf{n}_B} \,. \tag{6.45}$$

This demonstrates that the second-order effect on the Shapiro delay that is due to frame dragging is of order a_*/r_c. This term corresponds to the gravitomagnetic time delay first discussed in (Ciufolini et al. 2003).

The right panel of Figure 6.2 shows the second-order contribution to the light time travel delay due to frame dragging for a pulsar in a circular orbit around a black hole as a function of orbital phase. We also compare it (left panel) to the second-order contribution due to lensing derived in the previous section. For the purposes of this figure, we set the pulsar orbital radius to $1000M$, its inclination to $80°$, and the observer on the equatorial plane of the black hole. We also varied the spin of the black hole from being retrograde to the orbital motion ($a = -1$) to being prograde ($a = 0, 0.4, 1.04$).

As expected, the contribution due to frame dragging changes sign around orbital phases $\nu = \pi/2$, as the photons from the pulsar to the distant observer change from

moving with the direction of frame dragging to moving against it. The fact that at, these two phases in a circular orbit, the contribution due to frame dragging vanishes while the contribution due to lensing has its maximum value, makes the overall amplitude of the former to be significantly suppressed compared to the amplitude of the latter effect, even though they both have the same scaling with r_c.

Contribution from the β parameter

The terms we are interested now in equation (6.34) are the $g^{ij}_{(2)}$ terms that are proportional to the parameter β. In order to evaluate them, we write

$$\begin{aligned}\frac{1}{2}R_{AB}\left[N^i_{AB}N^j_{AB}g^{ij}_{(2),\mathrm{Q}}\right]_{\mathbf{z}_+(\mu)} = \\ \beta\frac{(x_B-x_A)^2}{R_{AB}}\frac{-x^2+y^2+z^2}{(x^2+y^2+z^2)^2} + \beta\frac{(y_B-y_A)^2}{R_{AB}}\frac{-y^2+x^2+z^2}{(x^2+y^2+z^2)^2} \\ -\beta\frac{(z_B-z_A)^2}{R_{AB}}\frac{-z^2+x^2+y^2}{(x^2+y^2+z^2)^2} - 8\beta\frac{(x_B-x_A)(y_B-y_A)}{R_{AB}}\frac{xy}{(x^2+y^2+z^2)^2}\,,\end{aligned} \tag{6.46}$$

where $g^{ij}_{(2),\mathrm{Q}}$ refers to the spatial metric components that are proportional to β. After substituting $\mathbf{r} = \mathbf{r}_A + \mu(\mathbf{r}_B - \mathbf{r}_A)$, we perform the same mathematical trick as before, but this time separating the terms proportional to μ^0, μ, and μ^2, and writing them in

terms of their coefficients, A, B, and C, i.e.,

$$\frac{1}{2}R_{AB}\int_0^1 \left[N^i_{AB}N^j_{AB}g^{ij}_{(2)}\right]_{\mathbf{z}_+(\mu)} d\mu$$
$$= \int_0^1 \left[\frac{A}{(x^2+y^2+z^2)^2} + \mu\frac{B}{(x^2+y^2+z^2)^2} + \mu^2\frac{C}{(x^2+y^2+z^2)^2}\right] d\mu \ , \tag{6.47}$$

where

$$\begin{aligned}
A \equiv 2[&-4x_A(x_A-x_B)y_A(y_A-y_B) - (x_A-x_B)^2(x_A^2-y_A^2-z_a^2) \\
&+ (y_A-y_B)^2(x_A^2-y_A^2+z_a^2) - (x_A^2+y_A^2-z_a^2)(z_a-z_B)^2]\beta \\
B \equiv 4\{&x_A^4 - 3x_A^3x_B - x_Ax_B(x_B^2+3y_A^2-4y_Ay_B+y_B^2-z_a^2+z_B^2) \\
&+ x_A^2(3x_B^2+2y_A^2-3y_Ay_B+y_B^2-z_az_B+z_B^2) \\
&+ (x_B^2+y_A^2-2y_Ay_B+y_B^2+z_a^2-2z_az_B+z_B^2)[y_A^2-y_Ay_B+ \\
&z_a(-z_a+z_B)]\}\beta \\
C \equiv 2\{&x_A^4 - 4x_A^3x_B + x_B^4 + y_A^4 - 4x_Ax_B[x_B^2+(y_A-y_B)^2]+ \\
&- 4y_A^3y_B2x_A^2[3x_B^2+(y_A-y_B)^2] + 2x_B^2(y_A-y_B)^2 \\
&+ 6y_A^2y_B^2 - 4y_Ay_B^3 + y_B^4 - z_a^4 + 4z_a^3z_B - 6z_a^2z_B^2 + 4z_az_B^3 - z_B^4\}\beta \ .
\end{aligned} \tag{6.48}$$

We can, therefore, write the second order contribution in this case as

$$\Delta^{(2)}_\beta(\mathbf{r}_A,\mathbf{r}_B) = [I_0+I_1+I_2]^1_0 \ , \tag{6.49}$$

where the indefinite integrals

$$I_0 \equiv \int \frac{A}{r^4} d\mu \ , \tag{6.50}$$

$$I_1 \equiv \int \frac{\mu B}{r^4} d\mu \ , \tag{6.51}$$

$$I_2 \equiv \int \frac{\mu^2 C}{r^4} d\mu \ , \tag{6.52}$$

can be found in Section 6.4.

Figure 6.3 shows the second-order contribution due to changes in the β parameter to the light travel time delay for a pulsar in a circular orbit around a black hole. We consider black holes characterized by $\beta = -0.5,\ 0.2$, and 0.5. The orbital distance of the pulsar is $1000M$, its inclination is 80°, and the observer is placed on the equatorial plane of the black hole.

The overall magnitude of the excursion due to variations in the β parameter is much smaller than lensing and frame-dragging contributions and increases with the magnitude of β. The complicated expressions shown in Section 6.4 make it hard to obtain the scaling of this effect in an analytical manner. However, as we show in 6.5, comparing our results with those of Ref. Zschocke & Klioner (2009), which were obtained using a different approach with harmonic coordinates, allows us to simplify expression (6.49), for the particular configuration that we are considering here as an

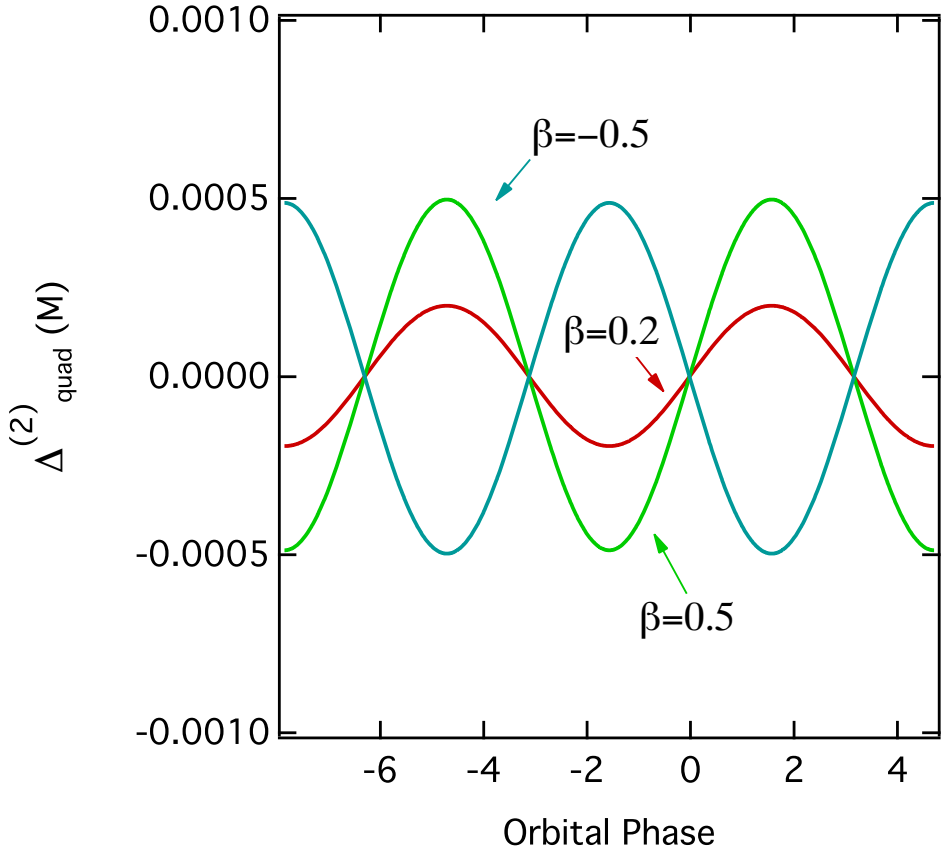

Figure 6.3: The second order β contribution to the light travel time delay for a pulsar in a circular orbit around black holes with different values of the parameter β. The orbital radius of the orbit is $1000M$, its inclination is 80°, and the observer is at the equatorial plane of the black hole; superior conjunction occurs at an orbital phase of $\pi/2$.

example, to

$$\Delta^{(2)}_{\beta} = -\frac{\beta}{2R_{AB}}\left(\frac{r_A^2 - r_B^2 - R_{AB}^2}{r_B^2} + \frac{r_B^2 - r_A^2 - R_{AB}^2}{r_A^2}\right) . \tag{6.53}$$

At the astrophysically relevant limit $r_B \gg r_A$, this expression reduces to

$$\Delta_\beta^{(2)} = -\frac{\beta}{r_A}\mathbf{n}_A \cdot \mathbf{n}_B \ . \tag{6.54}$$

Comparing this second-order contribution, which scale as the inverse of the orbital distance to the pulsar, to the mass and spin effects derived in the previous subsection, which scale as the inverse of the distance of closest approach of light to the black hole, accounts for the fact that the effect of the β parameter is significantly smaller for high-inclination observers than those of the mass and the spin.

6.3 Conclusion

In this paper we have provided formulae for the light time travel delays for pulsars orbiting in the spacetime of a black hole, taking into account terms that are up to the $(GM/rc^2)^2$ order. We identified three effects that are, in principle, of the same order. The first effect is expressed in terms that are proportional to the square of the black-hole mass and describe the additional delays due to the lensed trajectories of the photons. The second effect is expressed in terms that are proportional to the black-hole spin and describe the effects of frame dragging. Finally, the last effect describes the influence of the deformation parameter β of the spacetime on the time delays.

We reproduce our expression here for ease of reading, under the astrophysically

relevant assumption $r_B \gg r_A$:

$$\begin{aligned}
\Delta^{(1)} &= 2\log\left(\frac{r_c + r_A \mathbf{n}_A \times \mathbf{n}_B}{r_c - r_A \mathbf{n}_A \times \mathbf{n}_B}\right) , \\
\Delta^{(2)}_{\rm mass} &= \frac{\mathbf{n}_A \times \mathbf{n}_B}{r_c}\left[\frac{15\arccos(\mathbf{n}_A \cdot \mathbf{n}_B)}{4\sqrt{1-(\mathbf{n}_A \cdot \mathbf{n}_B)^2}} - \frac{4}{(1+\mathbf{n}_A \cdot \mathbf{n}_B)}\right] , \\
\Delta^{(2)}_{\rm spin} &= \frac{2a_*}{r_c}\frac{[\mathbf{n}_B - (\mathbf{n}_B \cdot \hat{z})\hat{z}] \times [\mathbf{n}_A - (\mathbf{n}_A \cdot \hat{z})\hat{z}](1 - \mathbf{n}_A \cdot \mathbf{n}_B)}{\mathbf{n}_A \times \mathbf{n}_B} \\
\Delta^{(2)}_{\beta} &= -\frac{\beta}{r_A}\mathbf{n}_A \cdot \mathbf{n}_B \, .
\end{aligned} \tag{6.55}$$

Even though the second-order effects are significantly smaller than the traditional Shapiro delay, their amplitude for the case of a pulsar orbiting a supermassive black hole is not negligible. This is shown in Figure 6.4, where we plot the amplitude of each effect (defined as the difference between the time delays calculated at the points of superior and inferior conjunction) for different pulsars orbiting the black-hole in the center of the Milky Way, Sgr A*. For reasonable distances of closest approach (see, e.g, discussion in Pfahl & Loeb (2004); Cordes et al. (2004); Liu et al. (2012); Psaltis et al. (2016)), the amplitudes of these effects are of the order of 100 ms−10 s. These are much larger than the ~ 1 ms measurement uncertainties expected for observations of a pulsar in orbit around Sgr A* with a 100-m dish or the $\lesssim 0.1$ ms uncertainties expected with SKA Liu et al. (2012).

At large distances from Sgr A*, the time delay in the pulsar signal may be contaminated by the presence of additional mass between the pulsar and the black hole. The

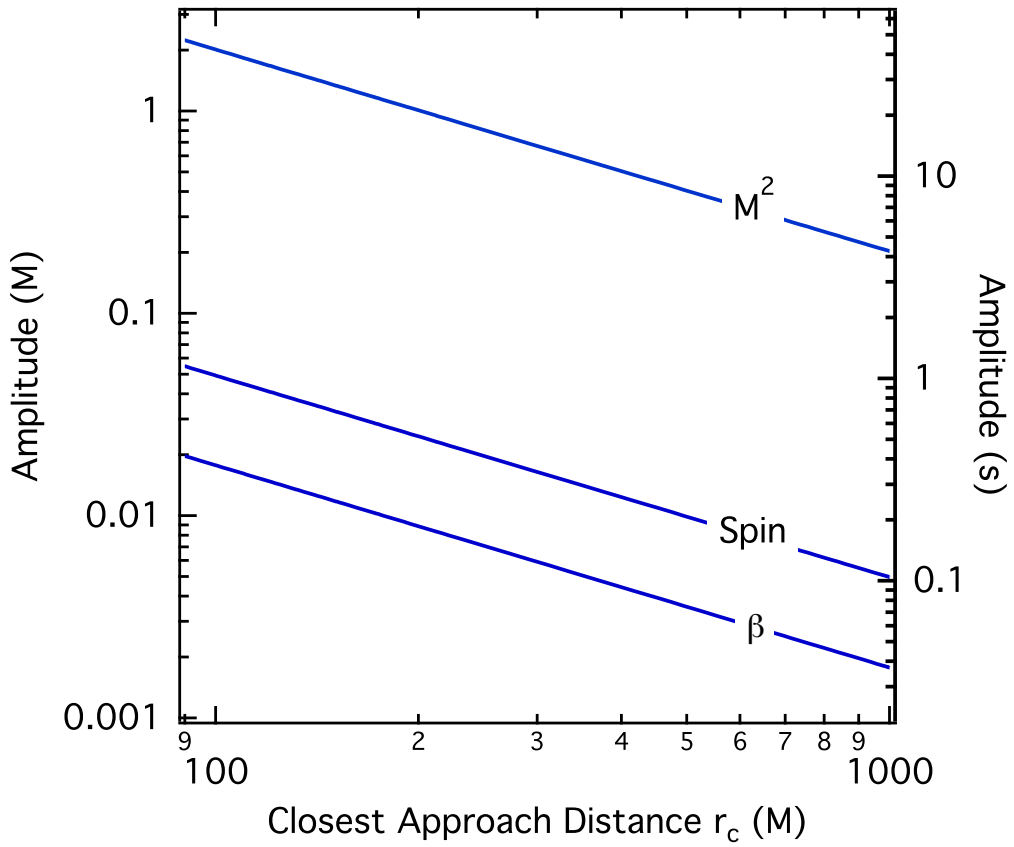

Figure 6.4: The amplitudes of the various contributions to the light travel time delay for a pulsar in different circular orbits around a black hole, as a function of the closest approach distance r_c. The inclination of the orbit is 80°, the observer is at the equatorial plane of a Kerr black hole, and the spin of the black hole is maximal. The right axis shows the amplitudes of the various contributions in seconds, for the $4.3 \times 10^6 M_\odot$ mass of Sgr A*. Even though these higher-order effects are small compared to the traditional Shapiro delay, they are much larger than the expected measurement uncertainties for pulsars around Sgr A*.

ratio between the leading second-order terms in the metric due to the gravitational field of the black hole and the first-order terms due to the additional enclosed mass

scale as Psaltis et al. (2016)

$$\propto \frac{M_{\rm enc}}{M}\left(\frac{ac^2}{GM}\right) = 4.8\times10^{-8}\left(\frac{M_{\rm enc}}{10^6\ M_\odot}\right)\left(\frac{a_0}{1\ {\rm pc}}\right)^{-1}\left(\frac{ac^2}{GM}\right)^2 , \tag{6.56}$$

where $M_{\rm enc}$ is the enclosed mass within a distance a_0 from the black hole and we have assumed a radial profile in the density of matter proportional to r^{-2}. In order for the gravitational effects of the enclosed mass to be negligible compared to the second-order effects due to the gravitational field of the black hole, the above ratio has to be smaller than unity, or

$$\frac{ac^2}{GM} \lesssim 4500\left(\frac{M_{\rm enc}}{10^6\ M_\odot}\right)^{-1}\left(\frac{a_0}{1\ {\rm pc}}\right) . \tag{6.57}$$

For pulsars in orbits with larger separations from the black hole, the second order effects we calculated here will not be measurable. The magnitude of the effects shown in Figure 6.4 are larger than the orbital effects due to the spacetime quadrupole that were discussed in Ref. Psaltis et al. (2016).

As a final validity check of our analytic expansion, we compared our analytic result to a numerical calculation of light time travel delays using the numerical algorithm of Ref. Psaltis & Johannsen (2012). In Figure 6.5 we plot the difference between the light travel time at superior and inferior conjunctions as a function of orbital radius, for a pulsar in circular orbits around a non-spinning black hole at an inclination of

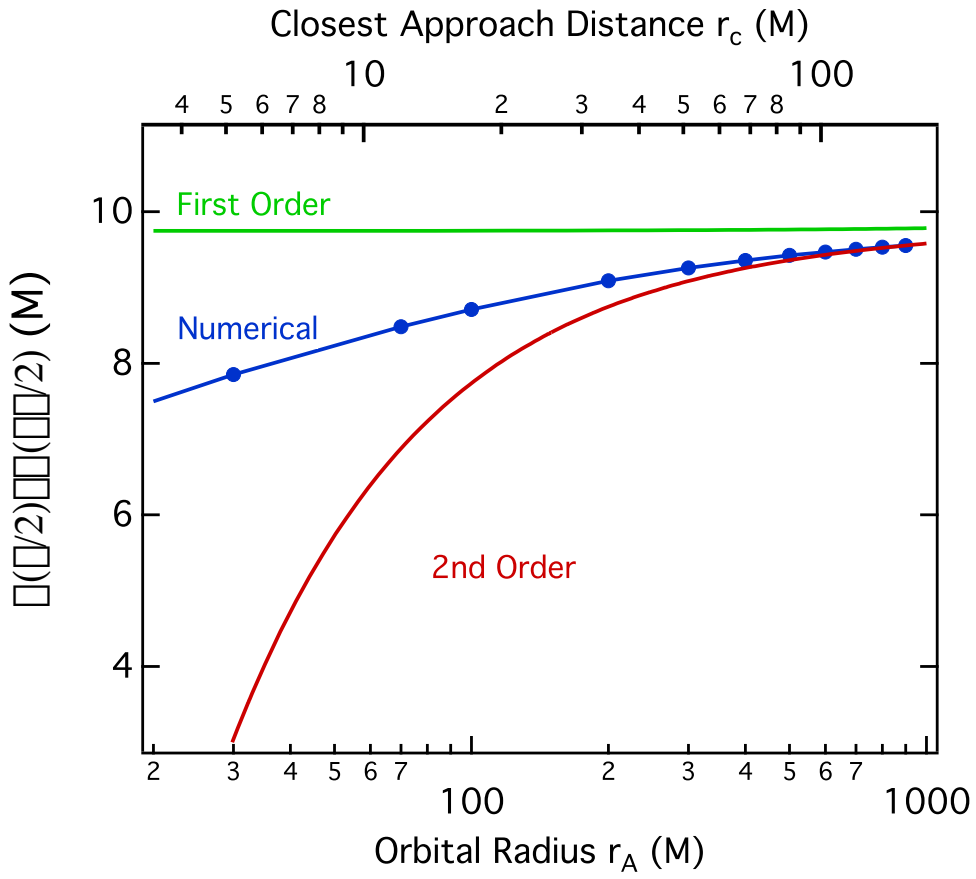

Figure 6.5: The difference between the light travel time delay at superior and inferior conjunction as a function of orbital radius for a pulsar in circular orbits around a non-spinning black hole at an inclination of 80°. The green line is the first order Shapiro delay and the red line is our second order calculation. The blue line with the filled circles is the result of a numerical calculation using the Psaltis-Johannsen algorithm (Psaltis & Johannsen 2012). The difference between the numerical result and the first order solution is significant even at large radii. The second order solution becomes inaccurate only at distances of closest approach that are $r_c \lesssim 60$ M.

80 degrees. It is clear even from this comparison that second-order effects become important at orbital radii that are of interest to pulsars around the black hole in the center of the Milky Way. Moreover, this comparison demonstrates that our second-order results remain accurate down to distances of closest approach $r_c \sim 60M$ and

will, therefore, be useful in the analysis of pulsar observations in this context.

6.4 Expression for the integrals of the β contribution

The indefinite integrals required to calculate the propagation time delay to second order in equation (6.52) is given by

$$\int \frac{A}{r^4} d\mu = \big(-4x_A(x_A - x_B)y_A(y_A - y_B) - (x_A - x_B)^2\big(x_A^2 - y_A^2 - z_A^2\big)$$

$$+ (y_A - y_B)^2\big(x_A^2 - y_A^2 + z_A^2\big) + \big(x_A^2 + y_A^2 + z_A^2\big)(z_A - z_B)^2\big)$$

$$\beta\big(\big(-z_A^2 + z_A z_B + x_A^2(-1+\mu) + y_A^2(-1+\mu) + x_B^2\mu + y_B^2\mu + z_A^2\mu$$

$$- 2z_A z_B\mu + z_B^2\mu + x_A(x_B - 2x_B\mu) + y_A(y_B - 2y_B\mu)\big)/\big(\big(x_B^2\big(y_A^2 + z_A^2\big) + (y_B z_A - y_A z_B)^2$$

$$- 2x_A x_B(y_A y_B + z_A z_B) + x_A^2\big(y_B^2 + z_B^2\big)\big)\big(z_A^2 + x_A^2(-1+\mu)^2 + y_A^2(-1+\mu)^2 - 2z_A^2\mu$$

$$+2z_A z_B\mu - 2x_A x_B(-1+\mu)\mu - 2y_A y_B(-1+\mu)\mu + x_B^2\mu^2 + y_B^2\mu^2 + z_A^2\mu^2 - 2z_A z_B\mu^2 + z_B^2\mu^2\big)\big)$$

$$+\Bigg(\big(x_A^2 - 2x_A x_B + x_B^2 + y_A^2 - 2y_A y_B + y_B^2 + z_A^2 - 2z_A z_B + z_B^2\big)\mathrm{ArcTan}\Big\{\big(-z_A^2 + z_A z_B + x_A^2(-1+\mu)$$

$$+ y_A^2(-1+\mu) + x_B^2\mu + y_B^2\mu + z_A^2\mu - 2z_A z_B\mu + z_B^2\mu + x_A(x_B - 2x_B\mu) + y_A(y_B - 2y_B\mu)\big)$$

$$/\big[(x_B^2\big(y_A^2 + z_A^2\big) + (y_B z_A - y_A z_B)^2 - 2x_A x_B(y_A y_B + z_A z_B) + x_A^2\big(y_B^2 + z_B^2\big))^{(1/2)}\big]\Big\}\Bigg)/$$

$$\big(x_B^2\big(y_A^2 + z_A^2\big) + (y_B z_A - y_A z_B)^2 - 2x_A x_B(y_A y_B + z_A z_B) + x_A^2\big(y_B^2 + z_B^2\big)\big)^{3/2}\big)$$

$$\int \frac{\mu B}{r^4} d\mu = 2\big(2(x_A - x_B)(y_A - y_B)(2x_A y_A - x_B y_A - x_A y_B)$$

$$- \big(x_A^2 - x_A x_B + y_A^2 - y_A y_B + z_A(z_A - z_B)\big)(z_A - z_B)^2$$

$$+ (y_A - y_B)^2\big(-x_A^2 + x_A x_B + y_A^2 - y_A y_B + z_A(-z_A + z_B)\big)$$

$$+ (x_A - x_B)^2\big(x_A^2 - x_A x_B - y_A^2 + y_A y_B + z_A(-z_A + z_B)\big)\big)$$

$$\beta\big(\big(x_A^2(-1+\mu) + y_A^2(-1+\mu) - x_A x_B \mu - y_A y_B \mu + z_A(z_A(-1+\mu) - z_B\mu)\big)/$$

$$\big(\big(x_B^2\big(y_A^2 + z_A^2\big) + (y_B z_A - y_A z_B)^2 - 2x_A x_B(y_A y_B + z_A z_B) + x_A^2$$

$$\big(y_B^2 + z_B^2\big)\big)\big(z_A^2 + x_A^2(-1+\mu)^2 + y_A^2(-1+\mu)^2 - 2z_A^2\mu + 2z_A z_B\mu - 2x_A x_B(-1+\mu)\mu - 2y_A y_B(-1+\mu)\mu$$

$$+ x_B^2\mu^2 + y_B^2\mu^2 + z_A^2\mu^2 - 2z_A z_B\mu^2 + z_B^2\mu^2\big)\big) + \big(\big(x_A^2 - x_A x_B + y_A^2 - y_A y_B + z_A(z_A - z_B)\big)$$

$$\times \text{ArcTan}\big[\big(-z_A^2 + z_A z_B + x_A^2(-1+\mu) + y_A^2(-1+\mu) + x_B^2\mu + y_B^2\mu + z_A^2\mu - 2z_A z_B\mu + z_B^2\mu$$

$$+ x_A(x_B - 2x_B\mu) + y_A(y_B - 2y_B\mu)\big)/\big(x_B^2\big(y_A^2 + z_A^2\big) + (y_B z_A - y_A z_B)^2$$

$$- 2x_A x_B(y_A y_B + z_A z_B) + x_A^2\big(y_B^2 + z_B^2\big)\big)^{(1/2)}\big]\big)$$

$$/\big(x_B^2\big(y_A^2 + z_A^2\big) + (y_B z_A - y_A z_B)^2 - 2x_A x_B(y_A y_B + z_A z_B) + x_A^2\big(y_B^2 + z_B^2\big)\big)^{3/2}\big)$$

$$\int \frac{\mu^2 C}{r^4} d\mu = -2\big(x_A^4 - 4x_A^3 x_B + x_B^4 + y_A^4 - 4x_A x_B\big(x_B^2 + (y_A - y_B)^2\big) + 2x_A^2\big(3x_B^2 + (y_A - y_B)^2\big)$$

$$+ 2x_B^2(y_A - y_B)^2 - 4y_A^3 y_B + 6y_A^2 y_B^2 - 4y_A y_B^3 + y_B^4 - z_A^4 + 4z_A^3 z_B - 6z_A^2 z_B^2 + 4z_A z_B^3 - z_B^4\big)$$

$$\beta\big(\big(-x_A^4 + x_A^3 x_B - 2x_A^2 y_A^2 + x_A x_B y_A^2 - y_A^4 + x_A^2 y_A y_B + y_A^3 y_B - 2x_A^2 z_A^2$$

$$+ x_A x_B z_A^2 - 2y_A^2 z_A^2 + y_A y_B z_A^2 - z_A^4 + x_A^2 z_A z_B + y_A^2 z_A z_B + z_A^3 z_B + x_A^4 \mu - 2x_A^3$$

$$x_B\mu + x_A^2 x_B^2 \mu + 2x_A^2 y_A^2 \mu - 2x_A x_B y_A^2 \mu - x_B^2 y_A^2 \mu + y_A^4 \mu - 2x_A^2 y_A y_B \mu + 4x_A x_B y_A y_B \mu - 2y_A^3 y_B \mu$$

$$- x_A^2 y_B^2 \mu + y_A^2 y_B^2 \mu + 2x_A^2 z_A^2 \mu - 2x_A x_B z_A^2 \mu - x_B^2 z_A^2 \mu + 2y_A^2 z_A^2 \mu - 2y_A y_B z_A^2 \mu$$

$$- y_B^2 z_A^2 \mu + z_A^4 \mu - 2x_A^2 z_A z_B \mu + 4x_A x_B z_A z_B \mu - 2y_A^2 z_A z_B \mu + 4y_A y_B z_A z_B \mu - 2z_A^3 z_B \mu - x_A^2 z_B^2 \mu - y_A^2 z_B^2 \mu$$

$$+ z_A^2 z_B^2 \mu\big)/\big(2\big(x_A^2 - 2x_A x_B + x_B^2 + y_A^2 - 2y_A y_B + y_B^2 + z_A^2 - 2z_A z_B + z_B^2\big)$$

$$\big(x_B^2 y_A^2 - 2x_A x_B y_A y_B + x_A^2 y_B^2 + x_B^2 z_A^2 + y_B^2 z_A^2 - 2x_A x_B z_A z_B - 2y_A y_B z_A z_B + x_A^2 z_B^2$$

$$+ y_A^2 z_B^2\big)\big(x_A^2 + y_A^2 + z_A^2 - 2x_A^2\mu + 2x_A x_B \mu - 2y_A^2 \mu + 2y_A y_B \mu - 2z_A^2 \mu + 2z_A z_B \mu + x_A^2 \mu^2 - 2x_A x_B \mu^2$$

$$+ x_B^2 \mu^2 + y_A^2 \mu^2 - 2y_A y_B \mu^2 + y_B^2 \mu^2 + z_A^2 \mu^2 - 2z_A z_B \mu^2 + z_B^2 \mu^2\big)\big) + \big(\big(x_A^2 + y_A^2 + z_A^2\big)$$

$$\mathrm{ArcTan}\big[\big(-x_A^2 + x_A x_B - y_A^2 + y_A y_B - z_A^2 + z_A z_B + x_A^2 \mu - 2x_A x_B \mu + x_B^2 \mu + y_A^2 \mu - 2y_A y_B \mu + y_B^2 \mu + z_A^2 \mu$$

$$- 2z_A z_B \mu + z_B^2 \mu\big)/\big(\big(\big(x_B^2 y_A^2 - 2x_A x_B y_A y_B + x_A^2 y_B^2 + x_B^2 z_A^2 + y_B^2 z_A^2 - 2x_A x_B z_A z_B - 2y_A y_B z_A z_B + x_A^2 z_B^2$$

$$+ y_A^2 z_B^2\big)\big)^{1/2}\big]\big)/\big(2\big(x_B^2 y_A^2 - 2x_A x_B y_A y_B + x_A^2 y_B^2 + x_B^2 z_A^2 + y_B^2 z_A^2 - 2x_A x_B z_A z_B - 2y_A y_B z_A z_B$$

$$+ x_A^2 z_B^2 + y_A^2 z_B^2\big)^{3/2}\big)\big)$$

6.5 Comparison with other calculations

In this section, we compare the results of our calculations to those of other analytic efforts that employed different approximations and/or methods of solution. We also compare our results to numerical calculations that take into account all multipole moments of a spinning spacetime, in order to explore tha range of validity of our approximations.

We do not attempt to compare our results to those of Refs. Rafikov & Lai (2006); Lai & Rafikov (2005) for two reasons. First, those calculations combine the first-order Shapiro delay terms with the lensing equation, making it hard to identify and compare the effects of individual orders. Second, the lensing equation gives accurate results when the pulsar is behind the black hole, at a distance that is much larger than the distance of closest approach for light. This approximation is valid only for a very narrow range of orbital phases (very close to $\pi/2$) and observer inclinations (very close to $\pi/2$) and introduces significant errors in more general configurations (see discussion in Masooma (2011)).

Our results are in detail agreement with the PPN calculations of Ref. Richter & Matzner (1982a,b, 1983), who also used a quasi-isotropic coordinate system, when expressed in the appropriate variables.

Ref. (Zschocke & Klioner 2009) calculated the light travel delay for the Schwarzschild

metric using the PPN formalism in de Donder (harmonic) coordinates. Their result is

$$\begin{aligned}\Delta_{PPN} = & R^D_{AB} \\ & + 2\log\left(\frac{r^D_A + r^D_B + R^D_{AB}}{r^D_A + r^D_B - R^D_{AB}}\right) \\ & + 2\frac{R^D_{AB}}{|\mathbf{r}^D_B \times \mathbf{r}^D_A|}\left[(r^D_B - r^D_A)^2 - (R^D_{AB})^2\right] \\ & + \frac{15}{4}\frac{R^D_{AB}}{|\mathbf{r}^D_B \times \mathbf{r}^D_A|}\cos^{-1}(\mathbf{n}_A \cdot \mathbf{n}_B) \\ & + \frac{1}{8}\frac{1}{R^D_{AB}}\left[\frac{(r^D_A)^2 - (r^D_B)^2 - (R^D_{AB})^2}{(r^D_B)^2} + \frac{(r^D_B)^2 - (r^D_A)^2 - (R^D_{AB})^2}{(r^D_A)^2}\right] , \end{aligned} \tag{6.58}$$

where the superscript D denotes the r-coordinate in the de Donder gauge.

The first term in the above expression corresponds to the geometric delay, while the second term is the first order Shapiro delay. This second term is identical to our first order mass contribution to the time delay given by equation (6.31), even though they are written in different coordinates. The reason is that the conversion between the r-coordinates of de Donder, r^D, and the radial Schwarzschild coordinate, $r_{\rm Sch}$, is (where for clarity, we have temporarily reintroduced the black hole mass M into our equations)

$$r^D = r_{\rm Sch}\left(1 - \frac{M}{r_{\rm Sch}}\right) , \tag{6.59}$$

while the conversion between the isotropic radial coordinate (which we use here), r,

and the radial Schwarzschild coordinate, $r_{\rm Sch}$, is

$$r = \frac{r_{\rm Sch}}{2}\left[1 - \frac{M}{r_{\rm Sch}} + \left(1 - 2\frac{M}{r_{\rm Sch}}\right)^{\frac{1}{2}}\right] \tag{6.60}$$

$$\approx r_{\rm Sch}\left(1 - \frac{M}{r_{\rm Sch}}\right) , \tag{6.61}$$

As a result, to first order in M/r, $r \approx r^D$, and our expression is algebraically identical to that of Ref. Zschocke & Klioner (2009).

To second order in mass, the transformation between r and r^D is given by

$$r \approx r^D - \frac{M^2}{4(r^D)^2} . \tag{6.62}$$

It is easily verifiable that plugging this transformations to our equation for the second order mass term in the time delay does not change the algebraic expression, i.e.,

$$\Delta^{(2)}_{\rm mass} = \frac{R^D_{AB}}{2r^D_A r^D_B}\left[\frac{15\arccos(\mathbf{n}_A\cdot\mathbf{n}_B)}{2\sqrt{1-(\mathbf{n}_A\cdot\mathbf{n}_B)^2}} - \frac{8}{(1+\mathbf{n}_A\cdot\mathbf{n}_B)}\right] . \tag{6.63}$$

Using the definition of R^D_{AB}, the third term of the delay in equation (6.58) can be manipulated to read

$$2\frac{R^D_{AB}}{|\mathbf{r}^D_B\times\mathbf{r}^D_A|^2}\left[(r^D_B - r^D_A)^2 - R^{D2}_{AB}\right] = -\frac{4R^D_{AB}}{r^D_A r^D_B}\frac{1}{1+\cos\theta} , \tag{6.64}$$

which is the same as the second term of equation (6.63). Similarly, a trigonometric

identity can be used to transform the fourth term of the delay in equation (6.58) into

$$\frac{15}{4}\frac{R^D_{AB}}{|\mathbf{r}^D_B \times \mathbf{r}^D_A|}\cos^{-1}(\mathbf{n}_A \cdot \mathbf{n}_B) = \frac{15R^D_{AB}}{4r^D_A r^D_B}\frac{1}{\sqrt{1-\cos^2\theta}}\,, \tag{6.65}$$

which is the same as the first term of equation (6.63).

If the orbital configuration of the binary system is such that the $g^{(2)}_{zz}$ term can be ignored, i.e. when the term proportional to $(z_B - z_A)^2$ in equation (6.46) is small, it is straightforward to identify the last term of equation (6.58) with the $\beta = -1/4$ case of equation (6.49) and write

$$\Delta^{(2)}_\beta \left[I_0 + I_1 + I_2\right]_{\beta=-1/4} = \frac{1}{8R_{AB}}\left(\frac{r_A^2 - r_B^2 - R_{AB}^2}{r_B^2} + \frac{r_B^2 - r_A^2 - R_{AB}^2}{r_A^2}\right)\,. \tag{6.66}$$

We are inspired to seek a similar equivalence for arbitrary β, and by inspection we found that arbitrary β contributions of (6.49) in this limit can be written as

$$\Delta^{(2)}_\beta = -\frac{\beta}{2R_{AB}}\left(\frac{r_A^2 - r_B^2 - R_{AB}^2}{r_B^2} + \frac{r_B^2 - r_A^2 - R_{AB}^2}{r_A^2}\right)\,. \tag{6.67}$$

This serves as a simplification of the complicated equation (6.49), valid for all orbital configurations in the limit where the $g^{(2)}_{zz}$ term can be ignored. Indeed, for astrophysical purposes where $r_B \gg r_A$, the β contribution to the delay in this limit is given by

the extremely simple expression

$$\Delta_{\beta}^{(2)}|_{r_B \gg r_A} = -\frac{\beta}{r_A}\mathbf{n}_A \cdot \mathbf{n}_B \ . \tag{6.68}$$

7

Introduction to gravitational wave astrophysics

The detections of gravitational radiation from merging black holes by the Laser Interferometer Gravitation-Wave Observatory (LIGO) (Abbott et al. 2016b,a, 2017b,d,c) signaled the beginning of gravitational wave astrophysics. In this chapter, we provide

a brief introduction to gravitational waves. We begin with a description of gravitational waves as spacetime perturbations in GR, before proceeding with a discussion of their sources. We also describe some unique features of gravitational radiation that make them distinct from the more familiar electromagnetic radiation. In this chapter we again adopt geometrized units where $G = c = 1$, and our metric signature is $(-,+,+,+)$.

7.1 Linearized Einstein Equations and plane gravitational waves

In astrophysics, gravitational waves are formulated as small spacetime perturbations that propagate in the background spacetime. Consider a small perturbation of Minkowski spacetime,

$$g_{\mu\nu} = \eta_{\mu\nu} + h_{\mu\nu} \ , \tag{7.1}$$

where $\eta_{\mu\nu}$ is the Minkowski metric, and $h_{\mu\nu}$ is a perturbation satisfying $|h_{\mu\nu}| \ll 1$. Using the fact that up to linear order in $h_{\mu\nu}$, the Christoffel symbols are

$$\Gamma^{\mu}_{\alpha\beta} = \frac{1}{2}\eta^{\mu\nu}\left(\partial_\beta h_{\alpha\nu} + \partial_\alpha h_{\beta\nu} - \partial_\nu h_{\alpha\beta}\right) \ , \tag{7.2}$$

and the fact that the Ricci tensor is given by

$$R_{\mu\nu} = R^{\alpha}{}_{\mu\alpha\nu} = \partial_\alpha \Gamma^{\alpha}_{\mu\nu} - \partial_\nu \Gamma^{\alpha}_{\mu\alpha} + \Gamma^{\alpha}_{\beta\alpha}\Gamma^{\beta}_{\mu\nu} - \Gamma^{\alpha}_{\beta\nu}\Gamma^{\beta}_{\mu\alpha} \ , \tag{7.3}$$

one can show that the Ricci tensor to linear order is

$$R_{\mu\nu} = \frac{1}{2}\left(\partial_\nu\partial_\alpha h_\mu{}^\alpha + \partial_\mu\partial_\alpha h_\nu{}^\alpha - \partial^\alpha\partial_\alpha h_{\mu\nu} - \partial_\mu\partial_\nu h\right) \ , \tag{7.4}$$

where $h \equiv h_\alpha{}^\alpha$, and the raising and lowering of indices are done using the background metric, $\eta_{\mu\nu}$ instead of $g_{\mu\nu}$. Note also that $\partial_\alpha\partial^\alpha$ is simply $\Box_\eta$, the d'Alembertian of Minkowski spacetime.

We can plug in equation (7.1) to the Einstein Equation (with the cosmological constant suppressed),

$$G_{\mu\nu} = 8\pi T_{\mu\nu} \ , \tag{7.5}$$

to obtain an equation for $h_{\mu\nu}$. In order to simplify the resulting equation, it is convenient to define the quantity

$$\bar{h}_{\mu\nu} \equiv h_{\mu\nu} - \frac{1}{2}\eta_{\mu\nu}h \ , \tag{7.6}$$

and to work in the coordinates satisfying the Lorenz gauge condition

$$\partial_\alpha \bar{h}^{\mu\alpha} = 0 \ . \tag{7.7}$$

The end result is an equation for $\bar{h}_{\mu\nu}$ known as the linearized Einstein Field Equations,

$$-\partial_\alpha\partial^\alpha \bar{h}_{\mu\nu} = 16\pi T_{\mu\nu} \ . \tag{7.8}$$

In vacuum, this equation reduces to the wave equation

$$\Box_\eta \bar{h}_{\mu\nu} = 0 \; . \tag{7.9}$$

The simplest solution to this equation is the tensor plane-wave,

$$\bar{h}_{\mu\nu} = A_{\mu\nu} \exp(ik_\alpha x^\alpha) \; , \tag{7.10}$$

where k^α is a null vector denoting the wave vector, and $A_{\mu\nu}$ is a tensor of amplitudes satisfying $A_{\mu\alpha}k^\alpha = 0$. While this equation is complex, only the real part is taken as physical. This solution is analogous to the wave equation in electromagnetism,

$$\mathbf{E} = \mathbf{E}_0 e^{i(\mathbf{k}\cdot\mathbf{r}-\omega t)} \; , \tag{7.11}$$

where the electric field $\mathbf{E}$ is proportional to an amplitude vector $\mathbf{E}_0$ that is orthogonal to the wave vector, $\mathbf{E}_0 \cdot \mathbf{k} = 0$.

The Lorenz condition, equation (7.7) does not fully specify the gauge. Customarily, the leftover gauge freedom is used to impose the transverse-traceless (TT) gauge, where only the spatial components of $h_{\mu\nu}$ is nonzero,

$$h^{\mathrm{TT}}_{0\nu} = 0 \quad ; \quad \eta^{\mu\nu} h^{\mathrm{TT}}_{\mu\nu} = 0 \quad ; \quad \partial_\mu h^{\mu\nu}_{\mathrm{TT}} = 0 \; . \tag{7.12}$$

One can always convert $h_{\mu\nu}$ in any gauge to the TT gauge as long as the system under consideration is far from any sources, $T_{\mu\nu} \approx 0$. Importantly, in the TT gauge,

$$\bar{h}^{\mathrm{TT}}_{\mu\nu} = h^{\mathrm{TT}}_{\mu\nu} \ . \tag{7.13}$$

7.2 Polarization of plane gravitational waves

For a plane wave moving in the **k** direction, one can choose a Cartesian coordinate (t, x, y, z) where the spatial component of the wave vector is in the z direction,

$$k^{\mu} = (\omega, 0, 0, k) \ . \tag{7.14}$$

Because $k_{\nu}k^{\nu} = 0$,

$$\omega^2 = k^2 \ , \tag{7.15}$$

thus the wave vector is simply

$$k^{\mu} = (\omega, 0, 0, \omega) \ . \tag{7.16}$$

In the traceless transverse gauge, $h^{\mathrm{TT}}_{0\nu} = 0$ implies that

$$A^{\mathrm{TT}}_{0\nu} = 0 \ . \tag{7.17}$$

This condition along with the transversality of the plane-wave solution, $A^{\rm TT}_{\mu\alpha}k^\alpha = 0$ gives us the condition that

$$A^{\rm TT}_{z\nu} = 0 \; . \tag{7.18}$$

Because $A_{\mu\nu}$ is symmetric and traceless, we can further identify that

$$A^{\rm TT}_{xx} = -A^{\rm TT}_{yy} \qquad ; \qquad A^{\rm TT}_{xy} = A^{\rm TT}_{yx} \; . \tag{7.19}$$

By convention, these two propagating degrees of freedom are renamed to be

$$h_+ \equiv A^{\rm TT}_{xx} \qquad (\text{"plus" polarization}) \; , \tag{7.20}$$

$$h_\times \equiv A^{\rm TT}_{xy} \qquad (\text{"cross" polarization}) \; . \tag{7.21}$$

7.3 Sources of gravitational radiation

The linearized Einstein equation in the Lorenz gauge,

$$\Box \bar{h}_{ij} = -16\pi T_{ij} \; , \tag{7.22}$$

can be solved by the retarded Green's function, giving

$$\bar{h}_{ij}(t,\mathbf{x}) = 4\int \frac{1}{|\mathbf{x}-\mathbf{y}|} T_{ij}(t-|\mathbf{x}-\mathbf{y}|,\mathbf{y})\; d^3y \; , \tag{7.23}$$

where $\mathbf{x}$ (field point) and $\mathbf{y}$ (source point) are 3-vectors in space only, and the integral over d^3y are taken over the source. Taking the Fourier transform with respect to time defined as

$$\tilde{f}(\omega, \mathbf{x}) = \frac{1}{2\pi} \int e^{i\omega t} f(t, \mathbf{x}) dt \ , \tag{7.24}$$

gives us

$$\tilde{\bar{h}}_{\mu\nu}(\omega, \mathbf{x}) = 4 \int e^{i\omega|\mathbf{x}-\mathbf{y}|} \frac{\tilde{T}_{\mu\nu}(\omega, \mathbf{y})}{|\mathbf{x}-\mathbf{y}|} d^3y \ . \tag{7.25}$$

In astrophysics, typically our field points $\mathbf{x}$ are far from the source of the gravitational wave. If in addition, if the source is isolated and slowly moving, it is justifiable to take the following approximation: defining r as the distance between $\mathbf{x}$ and the "location of the of the source" (e.g. the center of mass of the source),

$$\tilde{\bar{h}}_{\mu\nu}(\omega, \mathbf{x}) = 4 \frac{e^{i\omega r}}{r} \int \tilde{T}_{\mu\nu}(\omega, \mathbf{y}) d^3y \ . \tag{7.26}$$

Integrating the right hand side by parts, we obtain that the spatial components of $\tilde{\bar{h}}_{\mu\nu}$ is given by

$$\tilde{\bar{h}}_{ij} = -2\omega^2 \frac{e^{i\omega r}}{r} \tilde{I}_{ij}(\omega) \ , \tag{7.27}$$

where

$$I_{ij}(t) = \int y^i y^j T^{00}(t, \mathbf{y}) d^3y \ , \tag{7.28}$$

is the quadrupole moment tensor. As before, the integral over d^3y is taken over the source. The timelike components of $\bar{\bar{h}}_{\mu\nu}$ can be obtained using the constraint

$$\omega \bar{\bar{h}}^{0\nu} = i\partial_i \bar{\bar{h}}^{i\nu} \ , \tag{7.29}$$

enforced by the Lorenz gauge condition. Performing the inverse Fourier transform on equation (7.27) gives us the famous quadrupole formula for the generation of gravitational radiation, which in units where we have reintroduced factors of G's and c's is given by

$$\bar{h}_{ij}(t, \mathbf{x}) = \frac{2G}{c^4 r} \frac{d^2}{dt^2} \left[I_{ij}(t - r/c) \right] \ . \tag{7.30}$$

This equation states that sources of gravitational radiation are time varying energy density quadrupoles.

7.4 Gravitational waves from binary inspirals

The quadrupole moment tensor of a circular binary system orbiting in the x-y plane in the Kepler problem is

$$I_{xx} = \frac{1}{2}\mu a^2[1 + \cos(2\Omega t)] \ , \tag{7.31}$$

$$I_{yy} = \frac{1}{2}\mu a^2[1 - \cos(2\Omega t)] \tag{7.32}$$

$$I_{xy} = \frac{1}{2}\mu a^2 \sin(2\Omega t) \ , \tag{7.33}$$

$$I_{iz} = 0 \ , \tag{7.34}$$

where μ is the reduced mass, a the semimajor axis, and Ω the orbital period. Plugging this to equation (7.30) gives us gravitational waves that depend on the trigonometric factors $\cos(2\Omega t_r)$ and $\sin(2\Omega t_r)$, where the trigonometric function depends on if we are looking at the x-x, x-y, or y-y components, i.e. it takes the form

$$\bar{h}_{ij} = \frac{2}{r}\mu a^2\Omega^2 \times [\text{trigonometric factors}]_{\text{ij}} \ , \tag{7.35}$$

where the trigonometric factors are:

$$\bar{h}_{xx} = -\bar{h}_{yy} \propto -\cos 2\Omega t_r \ , \tag{7.36}$$

$$\bar{h}_{xy} \propto -\sin 2\Omega t_r \ . \tag{7.37}$$

The amplitude of the wave with factors of G's and c's reintroduced is

$$|\bar{h}_{ij}| = \frac{2G}{c^4 r}\mu a^2 \Omega^2 \ , \tag{7.38}$$

and the gravitational wave frequency is twice the orbital frequency, 2Ω. The circular two-body problem in Newtonian physics is therefore a source of gravitational radiation that is both monochromatic and unchanging in time. Further, it is easy to see (either intuitively or through a direct computation of I_{ij}) that if the orbital motion is elliptical, the resulting gravitational radiation power will be spread over multiple frequencies.

As gravitational waves carry energy away from the system, the Keplerian two-body problem is only a good assumption when the energy of the orbiting bodies is large compared to the energy carried away by gravitational radiation*. In this limit, the gravitational waves are essentially non-dynamical, i.e. they do not affect the dynamics of the orbiting bodies. In all other cases, the loss of orbital energy through gravitational radiation will shrink the binary orbit. As gravitational waves also carry angular momentum, an eccentric binary will also evolve into a circular one (Peters 1964).

The energy-momentum of gravitational radiation can be given by the Landau-Lifshitz pseudotensor, $t_{\mu\nu}$, which in the TT gauge can be averaged over many wave-

*In addition to the standard approximations of Newtonian physics e.g. ignoring relativistic precessions.

lengths to give (Landau & Lifshitz 1975).

$$t_{\mu\nu} = \frac{1}{32\pi} \left\langle \partial_\mu h^{\rm TT}_{\rho\sigma} \partial_\nu h^{\rho\sigma}_{\rm TT} \right\rangle \ . \tag{7.39}$$

where $\langle \ldots \rangle$ denotes averaging over many wavelengths. For a plane wave with wave vector k^ν, this quantity is (Carroll 2004)

$$t_{\mu\nu} = \frac{1}{64\pi} k_\mu k_\nu A^{\rm TT}_{\rho\sigma} A^{\rho\sigma}_{\rm TT} \ . \tag{7.40}$$

Choosing a Cartesian coordinate so that the spatial component of k^ν points in the z axis, one obtains that $A^{\rm TT}_{\rho\sigma} A^{\rho\sigma}_{\rm TT} = 2(h_+^2 + h_\times^2)$. This results in the only nonzero components of $t_{\mu\nu}$ to be

$$t_{tt} = t_{zz} = -t_{tz} = -t_{zt} = \frac{1}{32\pi} \omega^2 (h_+^2 + h_\times^2) \ , \tag{7.41}$$

where again ω is the angular frequency of the gravitational radiation. For the binary problem, $\omega = 2\Omega$.

If we treat $t_{\mu\nu}$ as any other energy-momentum tensor, its $t_{t\nu}$ components represent an energy flux vector. The power radiated through a surface A is then

$$P_A = \int_A t_{t\nu} n^\nu dA \ , \tag{7.42}$$

where dA is the differential area of a surface element and n^ν its normal vector. Therefore, we can compute the power radiated away to null infinity to be

$$\langle P \rangle = \int_{S_\infty} t_{tr} r^2 d\Omega \, , \tag{7.43}$$

where the integral is taken over S_∞, the two sphere with radius $r \to \infty$, and we have switched to spherical coordinates (t, r, θ, ϕ). Note that the $\langle \ldots \rangle$ around P is necessary as the $t_{\mu\nu}$ of equation (7.39) is only defined over many wavelengths. Plugging in $t_{\mu\nu}$ for a circular binary, we obtain

$$\langle P \rangle = -\frac{32G^4}{5c^5 a^5} \mu^2 M^3 \, , \tag{7.44}$$

where μ is the reduced mass, M the total mass, and a the semimajor axis of the binary. For ease of comparison with physical units, we have also temporarily reintroduced G's and c's in this equation and for the rest of this section. In the binary problem, we have to average over a longer timescale than many wave periods. In this case, $\langle \ldots \rangle$ indicates an average over the orbital period.

Since orbital energy is radiated away, the binary tightens, and the semimajor axis changes following the formula (Peters 1964)

$$\frac{da}{dt} = -\frac{64G^3}{5c^5} \frac{\mu M^2}{a^3} \, . \tag{7.45}$$

Integrating this equation from $a = a_i$ to $a = 0$, where a_i is the current semimajor axis of the binary, one obtains the merger time of the binary

$$t_m = \frac{5c^5}{256G^3}\frac{a_i^4}{\mu M^2} \ . \tag{7.46}$$

7.5 Why gravitational radiation goes down as 1/distance

The first point is that h_{ij} goes down as $1/r$. As argued in the previous section, when the source is much smaller than the distance between the source and the observer, the $|\mathbf{x} - \mathbf{y}|$ in equation (7.23) is essentially $\sim r$, the distance between the observer and the center of the source, so that

$$\bar{h}_{ij} \propto \frac{1}{r} \ . \tag{7.47}$$

This is completely analogous to E&M, in which the radiative part of the electric field goes down as $1/r$ for the Lienard-Wiechert fields. Now, the reason the signal LIGO detects goes down as $1/r$ is because it is sensitive to the proper lengths of the interferometer arms, which in turn are sensitive to h_{ij}. If the two ends of one arm are separated by a distance δ in the x-axis, then the four displacement is

$$\Delta x^\mu = (0, \delta, 0, 0)^\mu \ . \tag{7.48}$$

The proper length along the arm is given by:

$$\Delta s = \sqrt{g_{\mu\nu}\Delta x^\mu \Delta x^\nu}\ , \tag{7.49}$$

$$= \sqrt{(\eta_{\mu\nu} + h_{\mu\nu})\Delta x^\mu \Delta x^\nu}\ , \tag{7.50}$$

$$= \sqrt{(1 + h_{xx})}\delta\ . \tag{7.51}$$

Since we are now in the TT gauge, the metric perturbation $h_{\mu\nu}$ is equal to its trace-reverse ($\bar{h}_{\mu\nu} = h_{\mu\nu}$) so that

$$\Delta s = \sqrt{(1 + \bar{h}_{xx})}\delta\ . \tag{7.52}$$

$$\approx \left[1 + \frac{1}{2}\bar{h}_{xx}\right]\delta\ . \tag{7.53}$$

Since h_{ij} goes down as $1/r$, then the extra proper length induced on the LIGO interferometer by the passing gravitational wave is

$$\frac{1}{2}\bar{h}_{xx} \propto \frac{1}{r}\ . \tag{7.54}$$

7.6 Why the signal for electromagnetic telescopes goes as 1/distance^2, and the analogous gravitational radiation problem

In the electromagnetic case, the radiative electric field goes down as $1/r$ (c.f. the Lienard-Wiechert field). The problem is that conventional telescopes care about fluxes

(i.e. energy per time per area) instead of the pure electric field. The Poynting vector is

$$\mathbf{S} = \frac{c}{4\pi}\mathbf{E} \times \mathbf{B} \,, \tag{7.55}$$

and has units of energy per time per area. This is the quantity that goes down as $1/r^2$ because

$$|S| \propto |E|^2 \propto \frac{1}{r^2} \,. \tag{7.56}$$

Similar to the electric field E_i, the h_{ij} of gravitational wave does not have units of energy per time per area; it is not the energy flux of gravitational radiation. However, analogously to the E&M case, we can write down a "Poynting vector" for gravitational wave to get to the energy flux. As discussed in the previous sections, the Poynting vector of E&M radiation is just c times the $0i$ part of the energy-momentum tensor, the analogous construction for gravitational wave (where we have specified the wave to move in the z direction and reintroduced factors of G's and c's) is therefore

$$S_z^{\mathrm{GW}} = -\frac{t_{0z}}{c} = \frac{1}{32}\frac{c^2}{G}\omega^2(h_+^2 + h_\times^2) \,, \tag{7.57}$$

where $t_{\mu\nu}$ is the gravitational wave energy-momentum pseudotensor, ω is the gravitational wave frequency, and the subscripts $+/\times$ denotes the two polarizations of gravitational radiation.

S_z^{GW} is analogous to the E&M Poynting vector in the z direction, and has units

energy per time per area: it is the energy flux of gravitational radiation. In particular, because it depends on $\sim \bar{h}^2$,

$$S_z^{\mathrm{GW}} \propto \frac{1}{r^2} \, . \tag{7.58}$$

Thus, the reason why the LIGO signal does not drop off as $1/r^2$ is because LIGO does not care about the energy flux (energy per time per area), in contrast to conventional telescopes. It cared simply of h_{ij}, which goes down as $1/r$. This is completely analogous to the E&M case: if one cares only of the electric field, one will get something that goes down as $1/r$. We only get the usual $1/r^2$ if we cared about the energy flux, with units of energy per time per area.

8

LISA detection of binary black holes in the Milky Way Galaxy

Using the black hole merger rate inferred from LIGO, we calculate the abundance of tightly bound binary black holes in the Milky Way galaxy. Binaries with a small semi-major axis ($\lesssim 10 R_\odot$) originate at larger separations through conventional formation

mechanisms and evolve as a result of gravitational wave emission. We find that LISA could detect them in the Milky Way. We also identify possible X-ray signatures of such binaries.

8.1 Introduction

The Laser Interferometer Gravitation-Wave Observatory (LIGO) discovered gravitational waves from binary black holes (Abbott et al. 2016b,a), composed of black holes with masses $\gtrsim 10 M_{\odot}$.

Two stars in an isolated binary can evolve to produce the progenitors of the LIGO sources. To possess the observed parameters of the LIGO sources, these binaries must have progenitors with high masses ($M \sim 40 - 100 M_{\odot}$) and low metallicities (Belczynski et al. 2016b). The binary evolution could be initially affected by mass transfer through a common envelope phase.

However, in the chemically homogeneous evolution model (de Mink & Mandel 2016; Mandel & de Mink 2016), two massive stars in a near contact binary spin rapidly due to tidal spin-orbit coupling. The rapid rotation of a star mixes its interior, allowing transport of hydrogen from the envelope to the core and metals from the core to the envelope (Maeder 1987). In contrast to the standard binary evolution model, the stars do not follow a common envelope phase, due to their contraction within their Roche lobes.

Regardless of the formation mechanism, none of the progenitor systems could directly produce two black holes at arbitrarily small separations. Here we focus on tight binary black holes with a semimajor axis smaller than could feasibly be created directly by conventional stellar evolution mechanisms. These binary black holes were born at a larger semimajor axis through standard evolution, and then migrated to smaller separations via gravitational wave emission. Most of these binary black holes reside in an intermediate regime, where their coalescence time is shorter than the Hubble time but longer than the LIGO operation lifetime before they become detectable in the LIGO frequency band.

We focus our analysis on binary black holes within the Milky Way galaxy. While most of our equations could be applied to binaries at arbitrary distances, the signatures of the systems under consideration are not observable outside of the Milky Way. We will assume circular orbits, as the detected LIGO binaries are constrained to possess low eccentricities (Abbott et al. 2016b). This means that we neglect binary black hole production via many body encounters and strong interactions in globular clusters (Sigurdsson & Hernquist 1993; Rodriguez et al. 2015). Aside from these assumptions, we will remain agnostic as to the specific mechanism producing the binaries.

Recently, Seto (2016) used an estimate of the population of Galactic binary black holes to predict that LISA will have the sensitivities required to detect binaries like GW150914. In this article, we used a more sophisticated population analysis to show that the result can be generalized to more complicated population models. Further-

more, we extend the calculation to black hole populations with varying masses and take into account the black hole mass function.

In §8.2 we perform a population analysis of tight binary black holes in the Milky Way. In §8.3 we show that the gravitational wave signatures of these tight binaries are observable by LISA. In §8.4 we examine possible X-ray signatures of these binaries. Finally, §8.5 summarizes our conclusions.

8.2 Population analysis

The number of binary black holes at a given time t with semimajor axis between a and $a + da$ can be written as,

$$dN(a,t) = \rho(a,t)da \ . \tag{8.1}$$

Assuming that their dynamical evolution is dominated by the emission of gravitational radiation, $\rho(a,t)$ obeys a simple advection equation,

$$\frac{\partial \rho(a,t)}{\partial t} - \frac{\partial}{\partial a}\left[K(M_1,M_2)\frac{\rho(a,t)}{a^3}\right] = S(a,t) \ , \tag{8.2}$$

where M_1 and M_2 are the masses of the two black holes, $S(a,t)$ is a source term that parameterizes the production of binaries at a semimajor axis a, and K is given by,

$$K(M_1, M_2) \equiv \frac{64}{5}\frac{G^3}{c^5}(M_1 M_2)(M_1 + M_2) \; .$$

In the simple case of $S = 0$, the solution of equation (8.2) is given by

$$\rho(a,t) = a^3 F\left[\frac{a^4}{4K} + t\right] \; , \tag{8.3}$$

where F is some arbitrary function. The simplest solution can be obtained in a steady state, where equation (8.2) reduces to

$$\frac{\partial}{\partial a}\left[K\frac{\rho(a)}{a^3}\right] = 0 \; . \tag{8.4}$$

Integrating this equation gives

$$\rho(a) = C\frac{a^3}{K} \; , \tag{8.5}$$

where C is an arbitrary constant. This is a special case of the solution in equation (8.3), with $F = C/K$.

The inferred merger rate from LIGO for two $30M_\odot$ black holes is between 2 and 600 Gpc^{-3} yr^{-1} (Abbott et al. 2016d) in comoving units. We can estimate the Galactic merger rate by adopting the number of Milky Way-like galaxies to be 10^{-2} per

comoving Mpc^3 (Montero-Dorta & Prada 2009). Adopting 100 Gpc^{-3} yr^{-1} as a fiducial LIGO inferred merger rate gives the LIGO Galactic merger rate to be $\sim 10^{-5} R_{100}$ mergers per galaxy per year.

A merger is detected by LIGO when the semimajor axis of the binary is small enough that it enters the LIGO frequency band. Denoting this critical semimajor axis as a_m, the merger rate R is equal to the flux in a-space at $a = a_m$,

$$\rho(a_m)\frac{K}{a_m^3} = R\,. \tag{8.6}$$

Therefore,

$$\rho(a) = \rho(a_m)\left[\frac{a}{a_m}\right]^3 = \frac{R}{K}a^3\,, \tag{8.7}$$

where we have substituted $\rho(a_m)$ from equation (8.6). Using the inferred Galactic merger rate and specializing to binary black holes of mass $M_1 = M_2 = 30M_\odot$, we can integrate over a to obtain the number of Galactic binary black holes with semimajor axis $\leq a$,

$$N(\leq a) \approx 3 \times 10^{-2} R_{100}\left[\frac{a}{\mathrm{R}_\odot}\right]^4\,, \tag{8.8}$$

where $R_\odot$ is the solar radius and R_{100} is the rate in units of 100 Gpc^{-3} yr^{-1}.

8.2.1 Source functions with a minimum injection scale

Next, we generalize the population analysis to cases with a source function. Most formation mechanisms cannot produce binaries that are very tight. We model this situation with a source function that is proportional to a step function, $S = \tilde{S}(a)\Theta(a - a_0)$, where a_0 is the minimum binary separation for the formation mechanism, Θ is the Heavyside step function, and $\tilde{S}(a)$ is an arbitrary function.

Given this source function, the general solution is,

$$\rho(a,t) = -\frac{1}{K}a^3\left[A\Theta(a-a_0)\int_{a_0}^{a}\tilde{S}da\right] + a^3F\left[\frac{a^4}{4K}+t\right] , \tag{8.9}$$

as long as the function $\tilde{S}(a)$ is not singular at $a = a_0$. For example, a power law source with normalization A and index n, $S = Aa^n\Theta(a - a_0)$, admits the general solution,

$$\rho(a,t) = -\frac{1}{K}a^3\left[A\frac{\Theta(a-a_0)}{(n+1)}(a^{n+1}-a_0^{n+1})\right] + a^3F\left[\frac{a^4}{4K}+t\right] . \tag{8.10}$$

Note also that in the case of a delta function source injected at $a = a_0$, the solution is given by,

$$\rho(a,t) = -\frac{1}{K}a^3A\Theta(a-a_0) + a^3F\left[\frac{a^4}{4K}+t\right] . \tag{8.11}$$

The most important feature of equation (8.9) is that the solution below the injection

point, $a < a_0$ is unchanged from the sourceless case. This implies that as long as we restrict our analysis to $a \leq a_0$, we can simply use the sourceless solution. Our results will therefore be robust due to its insensitivity to the particular binary black hole production mechanism.

8.2.2 Power-law source functions with a maximum injection scale

For the sake of generality, we also consider a source function without a minimum scale, namely $S(a) \propto a^n$ with positive n that extends all the way to $a = 0$. In principle, n is related to the power law index of the binary separation of massive stars (Sana et al. 2012). However, as not all massive binaries evolve into binary black holes, the mapping between the two indices is unknown. Since binaries are not produced up to arbitrarily high semimajor axis, we truncate our source function at high values of a by an exponential factor,

$$S(a) \propto a^n \exp\left[-\frac{a}{a_c}\right], \tag{8.12}$$

where a_c, is some large semimajor axis above which binary black holes are rarely produced. This source function corresponds to a mechanism that produces binaries over a broad range of a, where instead of a minimum injection scale, a_0, we now have a maximum injection scale, a_c. At large semimajor axes, this distribution corresponds to the end states of binary star evolution, whereas at small a it corresponds to more exotic processes such as direct collapse (Loeb 2016).

The binary population with this source term obeys

$$\frac{\partial \rho(a,t)}{\partial t} - \frac{\partial}{\partial a}\left[K(M_1,M_2)\frac{\rho(a,t)}{a^3}\right] = K_2 a^n \exp\left[-\frac{a}{a_c}\right], \tag{8.13}$$

where K_2 and n are constants that in principe can be constrained by observations. The general solution to this equation is given by,

$$\rho(a,t) = a^3 F\left[\frac{a^4}{4K} + t\right] + \frac{a^3 a_c^{n+1} K_2}{K}\Gamma\left[1+n, \frac{a}{a_c}\right], \tag{8.14}$$

where F is an arbitrary function and Γ is the incomplete Gamma function. As before, we can look for a steady state solution by setting the function F to be a constant C, giving

$$\rho(a) = a^3 C + \frac{a^3 a_c^{n+1} K_2}{K}\Gamma\left[1+n, \frac{a}{a_c}\right]. \tag{8.15}$$

In this case, the merger rate R equals the flux in a-space at $a = a_m$ plus a term corresponding to the source,

$$\rho(a_m)\frac{K}{a_m^3} + \sigma = R, \tag{8.16}$$

where σ is the rate of binary black holes created with $a \leq a_m$, given by,

$$\begin{aligned}\sigma &= \int_0^{a_m} K_2 a^n \exp\left[-\frac{a}{a_c}\right] da \\ &= K_2 a_c^{n+1}\left[\Gamma(1+n) - \Gamma\left(1+n, \frac{a_m}{a_c}\right)\right].\end{aligned} \tag{8.17}$$

Since $a_m \ll a_c$, we get,

$$C = \frac{R - K_2 a_c^{n+1} \Gamma\left(1+n, a_m/a_c\right)}{K} \ . \tag{8.18}$$

The number density of binary black holes is then given by,

$$\begin{aligned} \rho(a) &= a^3 \frac{R}{K} + \frac{a^3 a_c^{n+1} K_2}{K} \left[\Gamma\left(1+n, \frac{a}{a_c}\right) - \Gamma\left(1+n, \frac{a_m}{a_c}\right) \right] \\ &\approx a^3 \frac{R}{K} \ , \end{aligned} \tag{8.19}$$

where in the second equality we used the fact that both a/a_c and a_m/a_c are much smaller than unity. This result shows that in the case of a power law source function, the scaling of the sourceless solution $\rho \propto a^3$ remains valid even if the source function does not have a minimum scale as long as there is a maximum injection scale. The case of a power law with neither a maximum or minimum injection scale is treated in the §8.7.

8.2.3 Population analysis for varying black hole masses

In the previous sections, the abundance of binaries was derived for a given value of $K(M_1, M_2)$. In reality, the black hole population spans a range of masses with a probability given by the black hole mass function. Thus, the binaries possess varying values of K. In this section we incorporate this diversity of K values. Note that there is

a single advection equation for every value of K, i.e. there are many copies of equation (8.2), each for a different value of K. To make explicit its dependence on K, we label the density ρ in equation (8.2) as $\rho_K(a, K)$. The total number of binary black holes per semimajor axis is given in terms of $\rho_K(a, K)$ by,

$$\rho(a) = \int_{K_{min}}^{\infty} f_K \rho_K(a, K) dK \ , \tag{8.20}$$

where f_K is the probability of finding a binary black hole with a particular value of K. As $K = K(M_1, M_2)$ is a function of the two black hole masses, its probability distribution is determined by the mass functions of the first and second black holes, f_{M_1} and f_{M_2}, respectively. For simplicity, we adopt $f_{M_1} = f_{M_2} = \Phi_M$, and the distribution f_K can be obtained from Φ_M by a series of convolutions. Adopting a phenomenological power-law relation, $f_K = K_3 K^m$ with an index $m < -1$ and a normalization,

$$\int_{K_{min}}^{\infty} f_K dK = 1 \ , \tag{8.21}$$

we can derive the normalization constant K_3 in terms of K_{min}. Theoretically, the minimum K value is obtained when both black holes are at the limit imposed by the Tolman-Oppenheimer-Volkoff equation of a Chandrasekhar-Landau mass ($\sim 3M_\odot$) each. However, there is evidence that there exists a mass gap under $\sim 5M_\odot$ (Özel et al. 2010; Farr et al. 2011; Kreidberg et al. 2012). We thereby chose the minimum

K to be that when both black holes are $\sim 5M_\odot$ each.

For our phenomenological model with $m < -1$, the integral converges and can be solved to give,

$$K_3 = \frac{|m+1|}{K_{min}^{m+1}} = |m+1|K_{min}^{|m+1|} \; . \tag{8.22}$$

The merger rate is given by the sum over all masses of the fluxes in a-space,

$$\int_{K_{min}}^{\infty} f_K \rho_K(a_m, K) \frac{K}{a_m^3} dK = R \; . \tag{8.23}$$

For the sourceless steady-state solution, $\rho(a) = Ca^3/K$, we can find C in the phenomenological $f_K = K_3 K^m$ model by noting that,

$$\begin{aligned} R &= \int_{K_{min}}^{\infty} K_3 K^m \left[\frac{Ca_m^3}{K}\right] \frac{K}{a_m^3} dK \\ &= \frac{CK_3}{(m+1)} \; K^{m+1}\Big|_{K_{min}}^{\infty} \; . \end{aligned} \tag{8.24}$$

For $(m+1) < 0$, this integral converges to

$$R = -\frac{CK_3}{(m+1)} K_{min}^{m+1} \; , \tag{8.25}$$

which implies that for $(m+1) < 0$,

$$\rho_K(a, K) = -\frac{R(m+1)}{K_3 K_{min}^{m+1}} \frac{a^3}{K} \; . \tag{8.26}$$

The number of binary black holes per unit semimajor axis is therefore given by,

$$\rho(a) = -\frac{R(m+1)a^3}{K_3 K_{min}^{m+1}} \int_{K_{min}}^{\infty} \frac{K_3 K^m}{K} dK$$
$$= \frac{(m+1)}{m} \frac{Ra^3}{K_{min}} \, . \tag{8.27}$$

The number of Galactic binary black holes with semimajor axis $\leq a$ is given by

$$N(\leq a) = \frac{(m+1)}{m} \frac{Ra^4}{4K_{min}} \, . \tag{8.28}$$

Aside from numerical factors of order unity the only change from the single K case is that K_{min} appears in the denominator in place of K. Since K_{min} is $\sim$ 200 times smaller than the K for two 30 solar mass black holes, this number is of order 200 larger than in equation (8.8).

8.2.4 Population analysis for varying black hole masses: Chabrier/Kroupa IMF

Next, we proceed beyond the phenomenological toy model for f_K assuming that the black hole mass function follows the power-law dependence of massive stars, $\Phi_M = kM^{-2.3}$ (Chabrier 2003), where k is a constant. We define the quantity,

$$\tilde{K} \equiv \frac{5c^5}{64G^3} K = (M_1 + M_2) M_1 M_2 \, , \tag{8.29}$$

so that the respective distribution $f_{\tilde{K}}$ follows,

$$f_K(K) = \frac{5c^5}{64G^3} f_{\tilde{K}} \left[\frac{5c^5}{64G^3} K \right] \ . \tag{8.30}$$

If the masses M_1 and M_2 are independently distributed, f_K can be derived from Φ_M as follows. We first switch from the random variables M_1 and M_2 to $\tilde{K}$ and W, where $W \equiv M_1$ and,

$$M_2 = \frac{-W^2 + \sqrt{W^4 + 4W\tilde{K}}}{2W} \ , \tag{8.31}$$

where the positive root was chosen since W, M_2, and $\tilde{K}$ are positive definite. The distribution function $f_{\tilde{K}W}$ is then given by,

$$f_{\tilde{K}W} = |J| \Phi_M(W) \times \Phi_M \left[\frac{-W^2 + \sqrt{W^4 + 4W\tilde{K}}}{2W} \right] \ , \tag{8.32}$$

where the determinant of the Jacobian of the transformation,

$$|J| = \frac{1}{\sqrt{W^4 + 4W\tilde{K}}} \ . \tag{8.33}$$

The marginal distribution $f_{\tilde{K}}$ is therefore,

$$f_{\tilde{K}} = \int_{M_{\min}}^{M_{\max}} f_{\tilde{K}W} dW \ , \tag{8.34}$$

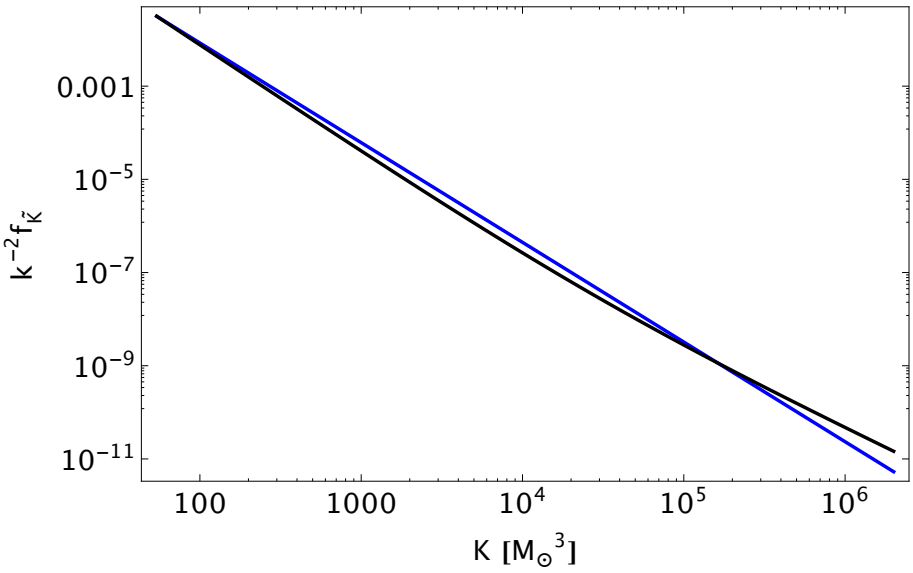

Figure 8.1: The probability function $f_{\tilde{K}}$ for the Chabrier/Kroupa IMF, $\Phi_M(m) = km^{-2.3}$ (black), compared with the fitting function $A\tilde{K}^{-\alpha}$ for $A = 159$ and $\alpha = 2.14$ (blue).

which for the assumed mass function is given by,

$$f_{\tilde{K}} = \int_{W_{\min}}^{W_{\max}} k^2 |J| W^{-2.3} \left[\frac{-W^2 + \sqrt{W^4 + 4W\tilde{K}}}{2W} \right]^{-2.3} dW \ . \tag{8.35}$$

Here, $W_{\min/\max}$ corresponds to the minimum and maximum black hole masses; in particular, $W_{\min}$ is again chosen to be $\sim 5M_\odot$ and $W_{\max} \sim 100M_\odot$, respectively.

Although the integral in equation (8.35) could only be solved numerically, the distribution is well represented by a power law form between $W_{\min}$ and $W_{\max}$ with a negative index $-\alpha \sim -2.1$ (see Figure 8.1). In order to simplify the analysis, we will therefore adopt,

$$f_{\tilde{K}}(\tilde{K}) \approx k^2 A \tilde{K}^{-\alpha} \ , \tag{8.36}$$

where $A = 159$. This gives

$$f_K(K) \approx \left[\frac{5c^5}{64G^3}\right]^{2/3} k^2 A K^{-\alpha} \tag{8.37}$$

$$\equiv K_3 K^{-\alpha} \, . \tag{8.38}$$

We proceed analogously to the previous section, where the main difference is that we now have an upper cutoff on black hole masses at $W_{\max}$.

For the steady state solution, $\rho(a) = Ca^3/K$, the rate of binary black holes entering the LIGO band is given by,

$$\begin{aligned} R &= \int_{K_{min}}^{K_{max}} f_K \rho_K(a_m, K) \frac{K}{a_m^3} dK \\ &= \int_{K_{min}}^{K_{max}} C K_3 K^{-\alpha} dK \\ &= C K_3 \frac{(K_{max}^{1-\alpha} - K_{min}^{1-\alpha})}{1-\alpha} \, . \end{aligned} \tag{8.39}$$

In equation (8.39), the integration limits refer to the maximum and minimum black hole masses that LIGO is sensitive to. The assumption that LIGO is sensitive to all black hole masses available in the black hole mass function translates to substituting K_{max} and K_{min} as these limits. Note that as the IMF is dominated by low mass black holes, our result is only weakly dependent on the exact value of K_{max}. Using R

to eliminate the constant C yields,

$$\rho_K(a,K) = \frac{R(1-\alpha)}{K_3(K_{max}^{1-\alpha} - K_{min}^{1-\alpha})}\frac{a^3}{K} \ . \tag{8.40}$$

The abundance of binaries is therefore given by,

$$\begin{aligned}\rho(a) &= \int_{K_{min}}^{K_{max}} f_K \rho_K(a,K) dK \\ &= \frac{(1-\alpha)Ra^3}{(K_{max}^{1-\alpha} - K_{min}^{1-\alpha})}\int_{K_{min}}^{K_{max}} \frac{K^{-\alpha}}{K} dK \\ &= \frac{(1-\alpha)Ra^3(K_{min}^{-\alpha} - K_{max}^{-\alpha})}{\alpha(K_{max}^{1-\alpha} - K_{min}^{1-\alpha})} \ .\end{aligned} \tag{8.41}$$

The number of binary black holes with semimajor axis $\leq a$ is then,

$$N(\leq a) = \frac{(1-\alpha)Ra^4(K_{min}^{-\alpha} - K_{max}^{-\alpha})}{4\alpha(K_{max}^{1-\alpha} - K_{min}^{1-\alpha})} \tag{8.42}$$

$$\approx 3 \times 10^4 R_{100}\left[\frac{a}{10R_\odot}\right]^4 \ . \tag{8.43}$$

While this result is derived by assuming that the black hole mass function follows the power-law mass function of massive stars, simulations indicate that not all massive stars form black holes, and that stars above $\sim 50M_\odot$ blow off too much of their mass to produce black holes (Sukhbold et al. 2016). These complications could lower the abundance of black holes relative to that predicted by equation (8.42). This means that our prediction should be interpreted as an upper bound to the number of binary

black holes in the Galaxy.

8.2.5 Comparison with population synthesis models

In order to compare our result to population synthesis models, we first transform our variable from a to the frequency f. The number of binary black holes with semimajor axis $\leq a_{\rm max}$ is equal to the number of binary black holes with frequency $\geq f_{\rm min}$, where $f_{\rm min}$ is the orbital period of the smallest black holes in the population with separation $a_{\rm max}$.

For the systems under consideration, $a_{\rm max} = 10R_\odot$ and the smallest black hole mass is $5M_\odot$, resulting in a minimum frequency of $f_{\rm min} = 2 \times 10^{-5}$Hz. Equation (8.42) therefore predicts $\approx 3 \times 10^4 R_{100}$ binary black holes in the Galaxy with frequency greater than 2×10^{-5}Hz.

The population synthesis model A of Belczynski et al. (2010a) predicts ∼thousands of binary black holes with frequencies greater than 2×10^{-5}Hz. Noting that the LIGO rate R_{100} ranges from 0.02 to 6, this is consistent with our result. An earlier calculation by Nelemans et al. (2001) predicts a number that is an order of magnitude larger than model A of Belczynski et al. (2010a), which is still consistent with our result.

8.3 Gravitational wave signal from Milky Way binaries

Most of the $3 \times 10^4 R_{100}$ Galactic binary black holes with orbital separation $a \leq 10 R_\odot$, will not enter the LIGO bandpass in a short enough time for them to be observed by LIGO. For example, the timescale for two $30 M_\odot$ black holes to coalesce from $a \sim$ a few $R_\odot$ is thousands of years. These binaries, however, will be observable by LISA* which is sensitive to lower frequencies than LIGO.

Focusing on the case of two $\sim 30 M_\odot$ black holes, we find from equation (8.8) that the tightest binary black hole in our Galaxy has $a \sim 2.5 R_\odot$. For such a binary consisting of two $30 M_\odot$ black holes, the gravitational wave frequency is $f \sim 3 \times 10^{-4}$ Hz, which is within the LISA bandpass (Farmer & Phinney 2003). The angular-averaged gravitational wave strain for the $n = 2$ mode is given by (Peters & Mathews 1963; Seto 2016),

$$A \approx 2.1 \times 10^{-20} \left(\frac{8 \text{ kpc}}{d} \right) \left(\frac{M_c}{28 M_\odot} \right)^{5/3} \left(\frac{f}{5 \times 10^{-4} \text{ Hz}} \right)^{2/3} , \tag{8.44}$$

where $M_c \equiv (M_1 M_2)^{3/5} (M_1 + M_2)^{-1/5}$ is the chirp mass. Integrating the signal over an observational period τ, the signal to noise ratio becomes (Seto 2016),

$$SNR \approx 70 \left(\frac{A}{2.1 \times 10^{-20}} \right) \left(\frac{h(f)}{3 \times 10^{-18} \text{ Hz}^{-1/2}} \right)^{-1} \left(\frac{\tau}{3 \text{ years}} \right)^{1/2} , \tag{8.45}$$

*http://www.elisascience.org

where $h(f)$ is the LISA instrumental noise, with a value of $\sim 3 \times 10^{-18}$ Hz$^{-1/2}$ at 0.5 mHz (Amaro-Seoane et al. 2012). Scaling the noise with frequency as the power law $h(f) \propto f^{-2}$ (Seto 2016), the signal to noise ratio becomes,

$$\begin{aligned} SNR &\approx 70 \left(\frac{A}{2.1 \times 10^{-20}}\right) \left(\frac{f}{5 \times 10^{-4}\text{Hz}}\right)^2 \left(\frac{\tau}{3 \text{ years}}\right)^{1/2} \\ &\approx 70 \left(\frac{8 \text{ kpc}}{d}\right) \left(\frac{M_c}{28 M_\odot}\right)^{5/3} \left(\frac{f}{5 \times 10^{-4} \text{ Hz}}\right)^{8/3} \left(\frac{\tau}{3 \text{ years}}\right)^{1/2} . \end{aligned} \tag{8.46}$$

For observations across the Milky Way with $d = 20$ kpc, we find,

$$SNR \approx 12 \times \left(\frac{20 \text{ kpc}}{d}\right) \left(\frac{\tau}{3 \text{ years}}\right)^{1/2} . \tag{8.47}$$

Figure 8.2 shows the expected number of such Milky Way binaries as a function of their SNR.

8.3.1 Confusion with cosmological sources

A supermassive binary black hole at cosmological distances can possess similar values of strain amplitude and frequency to a Galactic binary black hole, thus masquerading as a Galactic source. However, this confusion can be eliminated by measuring the change in gravitational wave frequency as a function of time, $\dot{f}$.

The time derivative of the gravitational wave frequency is given by (Cutler & Flana-

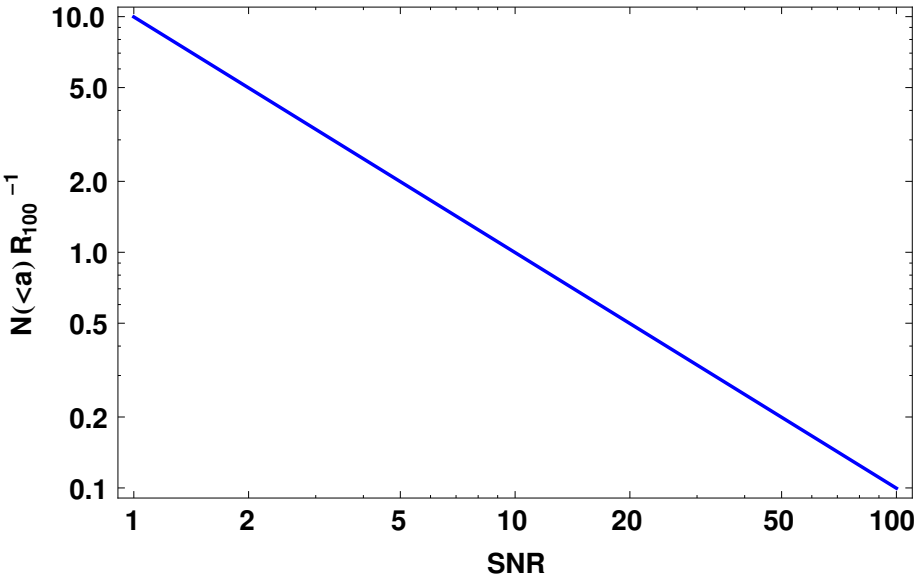

Figure 8.2: Expected number of Milky Way binaries composed of two $30M_\odot$ black holes as a function of the SNR at a distance $d = 20$ kpc.

gan 1994)

$$\dot{f} = \frac{96\pi^{8/3} f^{11/3}}{5} \left(\frac{G}{c^3} M_c\right)^{5/3} \propto M_c^{5/3} \,. \tag{8.48}$$

Supermassive binary black holes possess chirp masses that are much greater than that of Galactic binaries. As such, their frequency changes at a much faster pace than Galactic binaries.

8.4 Electromagnetic flag

8.4.1 Binary black hole accretion in a hierarchical triple system

A binary black hole could accrete gas if it resides in a hierarchical triple system, where the third object is a main sequence star. The wind of the third star would lead to accretion at the Bondi-Hoyle-Lyttleton rate (Hoyle & Lyttleton 1939; Bondi & Hoyle 1944),

$$\dot{M} = \frac{4\pi G^2 M_{tot}^2 \rho_w}{\sqrt{(c_w^2 + v_w^2)^3}} \ , \tag{8.49}$$

where $M_{tot} = M_1 + M_2$, ρ_w the mass density of the stellar wind, v_w the wind speed, and $c_w \equiv (5kT_w/3m_p)$ is the sound speed, with T_w be the wind temperature. Scaling the wind parameters to solar values at a distance of 1 AU and assuming an efficiency of 0.1 for converting rest mass into radiation, the luminosity produced by the binary where both black holes are ~ 30 solar masses is,

$$L \approx 2 \times 10^{30} \left[\frac{l}{1\text{AU}}\right]^{-2} \text{erg s}^{-1} \ , \tag{8.50}$$

where l is the separation of the star from the binary. The maximum luminosity is given by the Eddington limit,

$$L_E \approx 10^{40} \left[\frac{M_{tot}}{60 M_\odot}\right] \text{erg s}^{-1} \ . \tag{8.51}$$

Due to the orbital motion of the black holes around the center of mass, the observed flux would be modulated by Doppler beaming. Assuming that the emitted flux, $F_{\nu 0}$ scales with frequency as $F_{\nu 0} \propto \nu^{\beta}$, the Doppler modulation is given by

$$F_{\nu} = D^{3-\beta} F_{\nu 0} \ , \tag{8.52}$$

where F_{ν} is the observed flux, and D is the Doppler factor. To first order, the flux modulation is given by (D'Orazio et al. 2015),

$$\frac{\Delta F_{\nu}}{F_{\nu 0}} \approx (3-\beta)\sqrt{\frac{GM_{tot}}{a}}\frac{\cos\phi}{c}\sin i \ , \tag{8.53}$$

where ϕ is the orbital phase and i the inclination.

At the Eddington luminosity, the amplitude of the flux modulation of two $30M_{\odot}$ binary, is given by,

$$\Delta F \approx 0.6\left[\frac{10R_{\odot}}{a}\right]^{1/2}\left[\frac{\mathrm{pc}}{d}\right]^{2} \mathrm{erg\ s^{-1}\ cm^{-2}} \ , \tag{8.54}$$

where d is the distance to the object and we have assumed $\beta \sim 1$ (Sobolewska et al. 2011; D'Orazio et al. 2015). Given the flux sensitivity of XRM-Newton of $2{\times}10^{-15}$ erg cm^{-2} s^{-1}, for a semimajor axis of $a \sim 10R_{\odot}$, the flux modulation of these objects will be observable out to $d \sim 10$ Mpc.

Realistically, it is unlikely for such binaries to emit at the Eddington luminosity.

For general Bondi-Hoyle-Lyttleton accretion, the flux modulation depends on the binary and stellar wind parameters,

$$\Delta F \approx \frac{0.1\rho_w(3-\beta)c}{d^2\sqrt{(c_w^2+v_w^2)^3}}\sqrt{\frac{G^5M_{tot}^5}{a}}\sin i\ . \tag{8.55}$$

Substituting the solar wind parameters at $d = 1$ AU and the XRM-Newton sensitivity for ΔF yields for the observer distance of $d \sim 300$ pc at which a pair of $30M_\odot$ black holes will be detectable. The X-ray surveyor[†], a next generation x-ray observatory with a flux sensitivity of $\sim 10^{-19}$ erg cm^{-2} s^{-1}, will be able to detect this flux modulation out to a distance of ~ 30 kpc, which allows their detection throughout the entirety of the Milky Way galaxy.

Owing to the fact that most massive stars are in multiple systems (Raghavan et al. 2010; Tokovinin 2014), and that there is precedent for X-ray binaries in triple systems (Grindlay et al. 1988; Thorsett et al. 1999; Chou & Grindlay 2001; Zdziarski et al. 2007; Prodan & Murray 2015), most binary black holes will likely possess a third companion. Further evidence of this comes from observations of superorbital modulations in high-mass X-ray binary systems, which could be caused by a third companion (Farrell et al. 2006; Corbet & Krimm 2013). However, only a fraction of binary black holes in a hierarchical triplet would host companions in the relevant mass range for accretion to be efficient. Since only companions with masses $\sim 1M_\odot$ and above gener-

[†]http://wwwastro.msfc.nasa.gov/xrs/

ates sufficient luminosity to be observed throughout the Milky Way, the percentage of observable systems is

$$f_c = \frac{\int_{1M_\odot}^{100M_\odot} T_c(M)\Phi_M(M)dM}{\int_{0.07M_\odot}^{100M_\odot} T_H\Phi_M(M)dM} \, , \tag{8.56}$$

where Φ_M is the stellar IMF, $T_H \sim 1.4 \times 10^{10}$ yr is the Hubble time, and T_c is the main sequence lifetime of the companion star, given by the broken power law (Laughlin et al. 1997; Salaris & Cassisi 2006; Loeb et al. 2016)

$$T_c = \tau m^{-\Gamma} \, , \tag{8.57}$$

where $(\tau, \Gamma) = (10^{10} \text{ years}, \ 2.5)$ for stars less massive than $3M_\odot$ and $(\tau, \Gamma) = (7.6 \times 10^9 \text{ years}, \ 3.5)$ for more massive stars. The ratio in equation (8.56) takes into account both the stellar IMF and the fact that more massive stars live a shorter amount of time. Substituting the Chabrier IMF for Φ_M, we obtain,

$$f_c \sim 6 \times 10^{-2} \, . \tag{8.58}$$

This implies that out of the $\sim$ 300 black holes with $a \leq 10R_\odot$ predicted by equation (8.8), only a few systems would host the appropriate companion to be observable throughout the entirety of the Milky Way. This number is further diminished by the fact that only a fraction of all triple systems have the stars at a close enough distance, as the signal scales as $\rho_w \propto l^{-2}$. We therefore conclude that the most efficient method

to detect these binaries is through their gravitational wave emission with LISA.

8.4.2 Tidal disruption flares from planets and asteroids

Another source of electromagnetic activity could be associated with the tidal disruption of planets and asteroids by the black holes. White dwarfs and neutron stars are known to host rocky debris around them (Vanderburg et al. 2015; Zuckerman et al. 2010; Farihi et al. 2009; Koester et al. 2014; Wolszczan & Frail 1992; Podsiadlowski 1993; Phinney & Hansen 1993). Orbits around binary black holes can be chaotic and are subject to Kozai-Lidov oscillations, leading to an enhanced tidal disruption rate (Ivanov et al. 2005; Chen et al. 2009; Li et al. 2015).

For a planet or asteroid of mass m_p and radius r_p being tidally disrupted by a black hole of mass M, the length of the flare is defined as the time it takes for the emission to drop under the Eddington limit. This is given by (Ulmer 1998),

$$t_f \approx 1.9 \left(\frac{l_p}{l_t}\right)^{6/5} \left(\frac{r_p}{R_\odot}\right)^{3/5} \left(\frac{m_p}{M_\odot}\right)^{1/5} \times \left(\frac{\epsilon}{0.1}\right)^{3/5} \left(\frac{M_{tot}}{10^6 M_\odot}\right)^{-2/5} \text{ yrs} , \tag{8.59}$$

where l_p the pericenter distance and l_t the tidal radius. Assuming a Neptune-like planet with $m_p \sim 10^{29}$ g and $r_p \sim 10^{29}$ cm, the flare time becomes $t_f \sim 1.4$ years.

Since this timescale is much longer than the orbital timescale, lightcurves from these events will possess amplitude modulation due to the Doppler effect, as described

in section 8.4.1. The Doppler modulation of such systems is bright enough to be detectable from throughout the Milky Way by existing telescopes such as the XMM-Newton and the Chandra X-ray Observatory. As the number of sources in the sky per unit time will depend on the duty cycle of such flares, a monitoring campaign of a large patch of the sky is required to find such flaring sources. Confusion with other sources would make the identification of such binaries difficult.

8.5 Conclusions

By calibrating the population of binary black holes based on the merger rate infered by LIGO, we have found that LISA could detect a handful of such binaries in the Milky Way galaxy (see Figure 8.2). A lack of detections will set constraints on the binary production mechanisms.

We also considered electromagnetic flags of these tight binary black holes in the Milky way, and found them to have weaker observational prospects. Gravitational wave signals could be leveraged to provide both the system's masses and semimajor axis.

8.6 Acknowledgements

The authors thank Josh Grindlay for comments on the manuscript. This work was supported in part by the Black Hole Initiative at Harvard University, funded by the

John Templeton Foundation.

8.7 Power law sources

8.7.1 Power law source functions without a minimum or maximum scale

Consider a nonzero, time-independent power-law source term $S(a) \propto a^n$ that extends all the way from $a = 0$ to ∞. Unlike the example considered in the main text, we consider a case without a smallest injection scale or an upper cutoff scale. The binary black hole population with this source term obeys

$$\frac{\partial \rho(a,t)}{\partial t} - \frac{\partial}{\partial a}\left[K(M_1, M_2)\frac{\rho(a,t)}{a^3}\right] = K_2 a^n \,, \tag{8.60}$$

where K_2 and m are constants that in principe can be either derived or estimated from observations. The general solution to this equation is given by

$$\rho(a,t) = a^3 F\left[\frac{a^4}{4K} + t\right] - \frac{K_2 a^{4+n}}{K(1+n)} \,, \tag{8.61}$$

where F is an arbitrary function. As before, we search for a steady state solution by setting the function F to be the constant C, giving

$$\rho(a) = a^3 C - \frac{K_2 a^{4+n}}{K(1+n)} \,. \tag{8.62}$$

In this case, the merger rate R is equal to the flux in a-space at $a = a_m$ plus a term corresponding to the source term,

$$\rho(a_m)\frac{K}{a_m^3} + \sigma = R \,, \tag{8.63}$$

where σ is the rate of binary black holes created per year with semimajor axis $a \leq a_m$, given by

$$\sigma = \int_0^{a_m} K_2 a^m da = \frac{K_2}{n+1} a_m^{1+n} \,. \tag{8.64}$$

In this case,

$$\rho(a_m) = \frac{a_m^3 R}{K} - \frac{K_2 a_m^{4+n}}{K(1+n)} \,, \tag{8.65}$$

which allows us to deduce that $C = R/K$. Therefore, the number of Galactic binary black holes with semimajor axis $\leq a$ is given by

$$N(\leq a) = \frac{a^4 R}{4K} - \frac{K_2 a^{5+n}}{K(1+n)(5+n)} \tag{8.66}$$

$$= N_{\rm hom}(\leq a) - \frac{K_2 a^{5+n}}{K(1+n)(5+n)} \,, \tag{8.67}$$

where $N_{\rm hom}(\leq a)$ is the number of Galactic binary black holes in the source-less case. Note that when we set the source term to zero by using $K_2 = 0$, we will recover the sourceless solution. The effect of such a source term with $n > 0$, i.e. where there is a higher rate of binary black hole production at large semimajor axis, is paradoxically

a suppression of the number of binary black holes in the steady state solution due to the requirement that the rate R be kept unchanged. Since a source function that does not have a maximum injection scale is unphysical, the solution we obtain is also unphysical. In this case, there is a scale, $a_{\rm crit}$, above which $N(\leq a)$ becomes negative. This calculation should be viewed only as a pedagogical toy model to illustrate an example of the ramifications of modifying one of our assumptions.

8.7.2 Population analysis for varying black hole masses: Power law source

We can repeat the analysis for the case of a power law source term. In this case we have,

$$\rho_K(a,K) = a^3\frac{C}{K} - \frac{K_2 a^{4+n}}{K(1+n)}\,, \tag{8.68}$$

where, inspired by our previous solutions, we have explicitly written out the $1/K$ dependency of C so that it is now a constant with respect to K. The merger rate is therefore given by,

$$\begin{aligned} R &= \int_{K_{min}}^{\infty} K_3 K^m \left[a_m^3\frac{C}{K} - \frac{K_2 a_m^{4+n}}{K(1+n)}\right]\frac{K}{a_m^3}dK + \sigma \\ &= \sigma + \left[CK_3\frac{K^{m+1}}{(m+1)} - \frac{K_3 K_2 a_m^{1+n}K^{m+1}}{(1+n)(1+m)}\right]_{K_{min}}^{\infty}\,, \end{aligned} \tag{8.69}$$

which converges when $(m+1) < 0$ to

$$R = \sigma + \left[-C\frac{K_3 K_{min}^{m+1}}{(m+1)} + \frac{K_3 K_2 a_m^{1+n} K_{min}^{m+1}}{(1+n)(1+m)} \right] . \tag{8.70}$$

Here σ is again the rate of binary black holes created per year with semimajor axis $a \leq a_m$. However, in order to be consistent with our choice of the black hole mass function, we need to take into account the fact that different amounts of binary black holes are created for different black hole masses. Equivalently, binary black holes with different K's are produced at different abundances. As a result, σ has to include an extra integral over K,

$$\begin{aligned} \sigma &= \int_{K_{min}}^{\infty} f_K \frac{K_2}{n+1} a_m^{1+n} dK \\ &= \int_{K_{min}}^{\infty} K_3 K^m \frac{K_2}{n+1} a_m^{1+n} dK \\ &= K_3 \frac{K_2}{(1+n)(1+m)} a_m^{1+n} \left[K^{m+1} \right]_{K_{min}}^{\infty} . \end{aligned} \tag{8.71}$$

When $m+1 < 0$, this integral converges to,

$$\sigma = -\frac{K_3 K_2 a_m^{1+n} K_{min}^{m+1}}{(1+n)(1+m)} . \tag{8.72}$$

Following through, this gives the number of binary black holes per unit semimajor axis to be,

$$\rho(a,K) = -\frac{R(m+1)}{K_3 K_{min}^{m+1}}\frac{a^3}{K} - \frac{K_2 a^{4+n}}{K(1+n)} \,, \tag{8.73}$$

when $m < 0$. Note that when we set the source term to zero through $K_2 = 0$, we will recover the sourceless solution. The number of binary black holes per unit semimajor axis is therefore,

$$\rho(a) = \rho_{\rm hom}(a) + \frac{K_3 K_2 a^{4+n} K_{min}^m}{(1+n)m} \,, \tag{8.74}$$

where $\rho_{\rm hom}(a)$ is the solution in the sourceless case and the number of binary black holes with semimajor axis $\leq a$ is given by,

$$N(\leq a) = N_{\rm hom} + \frac{K_3 K_2 a^{5+n} K_{min}^m}{(1+n)(5+n)m} \,. \tag{8.75}$$

where as before $N_{\rm hom}$ is the sourceless solution. This solution is again pathological due to the presence of a critical semimajor axis above which $N(\leq a)$ becomes negative.

9

Evolution of the black hole mass function in star clusters from multiple mergers

We investigate the effects of black hole mergers in star clusters on the black hole mass function. As black holes are not produced in pair-instability supernovae, it is suggested that there is a dearth of high mass stellar black holes. This dearth generates

a gap in the upper end of the black hole mass function. Meanwhile, parameter fitting of X-ray binaries suggests the existence of a gap in the mass function under 5 solar masses. We show, through evolving a coagulation equation, that black hole mergers can appreciably fill the upper mass gap, and that the lower mass gap generates potentially observable features at larger mass scales. We also explore the importance of ejections in such systems and whether dynamical clusters can be formation sites of intermediate mass black hole seeds.

9.1 Introduction

The discovery of merging black holes (BHs) by the Laser Interferometer Gravitation-Wave Observatory (LIGO) signaled the beginning of gravitational wave astrophysics (Abbott et al. 2016b,a, 2017b,d,c). The masses of these binaries are much larger than those previously discovered as X-ray binaries (Özel et al. 2010; Farr et al. 2011; Kreidberg et al. 2012). The existence of these massive BHs was anticipated by previous calculations of BH mergers (Belczynski et al. 2010b,c; Dominik et al. 2015), and their detection spurred a growing interest on their formation mechanisms. One promising mechanism that allows binary BHs of such masses to form is the dynamical merger scenario, where BHs in dense star clusters gravitationally interact with each other to produce very hard binaries (O'Leary et al. 2006; Rodriguez et al. 2015, 2016a,b; Sukhbold et al. 2016; Samsing et al. 2018).

In such systems BHs borne out of mergers can merge again, producing second generation BHs (Antonini & Rasio 2016; Gerosa & Berti 2017; Fishbach et al. 2017; Rodriguez et al. 2017). These multiple mergers necessarily increase the number of massive BHs while simultaneously lowering the number of less massive BHs, making the BH mass function (BHMF) more top-heavy in the process.

Supernova theory also predicts the existence of a mass gap in the BH initial mass function (IMF) between $50 - 130 M_{\odot}$ because the stellar progenitors of BHs in this mass range undergo pair-instability supernovae (Belczynski et al. 2016a; Woosley 2017). Recently, parameter fitting of four LIGO data points suggests the existence of a cutoff at $M \sim 40 M_{\odot}$, bolstering the validity of this theoretical calculation (Fishbach & Holz 2017). Further, more massive binary BHs can be observed by LIGO to a greater distance, and so the absence of LIGO events at $M \gtrapprox 40 M_{\odot}$ within the increased survey volume can be used to set an upper limit on the BHMF. Analysis on the redshift distribution of LIGO events corroborates the existence of this mass gap (Bai et al. 2018).

In the dynamical merger scenario, multiple merger events might be able to appreciably fill the upper mass gap. In addition, while binary BHs in isolated binaries can merge to produce BHs in the upper mass gap, the lack of multiple merger events results in a very different BHMF within the upper mass gap. As such, the BHMF within the upper mass gap could be an effective test for the dynamical merger scenario.

Finally, parameter fitting of X-ray binaries suggests the existence of a lower mass gap in the BHMF between the most massive neutron stars and the least massive BHs (Özel et al. 2010; Farr et al. 2011). Under certain scenarios, supernova explosions can naturally produce this gap (Belczynski et al. 2012). According to Ref. Belczynski et al. (2012), Rayleigh-Taylor instabilities could appear early after the initial bounce of a supernova, and drive explosions $\lesssim 100-200$ ms after the collapse. In such rapid explosions, stars of mass $\sim 14-20M_{\odot}$ are thought to produce strong explosions that result in high mass neutron stars ($M \sim 1.5-2M_{\odot}$). However, stars of mass $\sim 20-40M_{\odot}$ fail to explode in this scenario, forming BHs of mass $M \sim 5-10M_{\odot}$.

This gap has also been successfully reproduced by numerical simulations of neutrino-driven supernova explosions (Sukhbold et al. 2016). Neutrino-driven explosions suggests that smaller stars never implode to form BHs, a prediction that has also been corroborated by the observed BH and neutron star distributions (Raithel et al. 2017). If multiple mergers are allowed, the lack of BHs in this range will have repercussions to the BHMF even at larger mass scales, as heavier BHs cannot merge with BHs in the lower mass gap to produce more massive BHs.

To answer such questions, a method to quickly compute the evolution of the BHMF is needed. In this work, we will employ the Smoluchowski coagulation equation Smoluchowski (1916), a rate equation describing the time evolution of the number of particles of a certain size as the particles are allowed to interact and 'coagulate', merging to form larger particles. The calculations performed in this formalism are much faster

than those required in N-body simulations of dynamical clusters, allowing a large parameter space to be covered efficiently.

This paper is organized as follows: in §9.2 we describe the Smoluchowski coagulation equation formalism, and in §9.3 we discuss our results for the evolution of the BHMF assuming constant kernel. Subsequently, §9.4 presents our results with top-heavy kernels. Finally, §9.5 summarizes our conclusions.

9.2 Methods

The evolution of the BH mass function due to mergers can be modeled by a coagulation equation,

$$\frac{\partial N(M,t)}{\partial t} = \frac{1}{2}\int_0^M K(M-M',M')N(M-M',t)N(M',t)\mathrm{d}M' - \int_0^\infty K(M,M')N(M,t)N(M',t)\mathrm{d}M' - S(M,t)\ , \tag{9.1}$$

where $N(M,t)\mathrm{dM}$ is the number of black holes in the star cluster of mass $\in [M, M+\mathrm{dM})$ at time t, $K(x,y)$ – the coagulation kernel – is the rate of two BHs of masses x and y to merge, and $S(M,t)$ represents possible source or sink terms. The first term of this equation describes BHs of mass $< M$ merging to form BHs of mass M, while the second term describes removal of BHs of mass M merging to form BHs with mass

N_{BH}	$R_{\rm tot}$ [100 Gpc^{-3} yr^{-1}]	N_C	$f_{\rm ej}$	Kernel	Figure Number
1000	100	100	0	Constant	Figure 9.1 (top)
1000	300	33	0	Constant	Figure 9.1 (bottom)
100	100	100	0	Constant	Figure 9.3
1000	300	33	0.5	Constant	Figure 9.4 (top)
1000	300	33	0.9	Constant	Figure 9.4 (middle)
1000	300	1	0.9	Constant	Figure 9.4 (bottom)
1000	100	100	0.9	Equation (9.7)	Figure 9.5
1000	10	100	0.5	Equation (9.8)	Figure 9.6

Table 9.1: List of parameters for the different scenarios under consideration in this paper. N_{BH} is the number of BHs per cluster, $R_{\rm tot}$ is the cosmological LIGO rate, N_C is the number of clusters per galaxy, $f_{\rm ej}$ is the ejection fraction, and Kernel denotes the coagulation kernel we used.

$> M$.

Equation (9.1) is called the Smoluchowski (1916) coagulation equation, a general integro-differential equation that describes the statistical time-evolution of the distribution (as a function of mass, size, etc.) of a coagulating population of objects. The detailed physics of the coagulation process is encoded in the coagulation kernel, allowing one to just evolve the statistical ensemble. The numerical method used to solve Equation (9.1) is described in §9.6.

We solve the coagulation equation for a variety of physical scenarios, and study its evolution over 10 Gyrs. Our IMF follows the Salpeter function ($N \propto M^{\alpha}$, $\alpha = -2.35$; Salpeter 1955) with an upper mass gap for $50M_{\odot} < M < 130M_{\odot}$ and a lower mass gap for $M < 5M_{\odot}$. The different scenarios considered in this paper are summarized in Table 9.1.

9.3 Constant kernel evolution

First we study the evolution of the BHMF assuming that the kernel $K(M, M') = K$ is a constant. This assumption is equivalent to the statement that the merger probability of two BHs is independent of their masses. In order to calibrate the constant K, we enforce the condition that the merger rate is equal to the LIGO merger rate per cluster, $R_{\rm LIGO}$. This is done by noting that the total number of mergers per unit time is

$$\begin{aligned} R_{\rm LIGO} &= \int_0^\infty \int_0^\infty K(x,y) n(x,t) n(y,t) {\rm d}x{\rm d}y \\ &= K \times N_{\rm BH}^2 \, , \end{aligned} \tag{9.2}$$

where $N_{\rm BH}$ is the number of BHs in the cluster. To estimate the LIGO rate per cluster, we adopt $\sim 10^{-2}$ per comoving Mpc^3 as the number density of Milky Way-Like Galaxies (MWEG) (Montero-Dorta & Prada 2009). Adopting 100 Gpc^{-3} yr^{-1} as a fiducial LIGO inferred merger rate gives the LIGO Galactic merger rate as $N_{\rm MWEG} \sim 10^{-5} R_{100}$ mergers per galaxy per year. For $R_{\rm tot}$ being the reported LIGO rate, the LIGO rate per cluster is therefore given by

$$\begin{aligned} R_{\rm LIGO} &= \frac{R_{\rm tot}}{N_C N_{\rm MWEG}} \\ &= 10^{-5} \left[\frac{R_{\rm tot}}{100 \ {\rm Gpc}^{-3} \ {\rm yr}^{-1}} \right] \left[\frac{1}{N_C} \right] \ {\rm yr}^{-1} \, , \end{aligned} \tag{9.3}$$

where N_C is the number of star clusters per galaxy.

9.3.1 No ejections

The simplest system that we can study using this formalism is obtained by setting $S(M,t) = 0$ in Equation (9.1). This is equivalent to saying that the BHs exist in a closed system, and that no mergers are violent enough to eject BHs out of the system. This situation is expected in cases where the star cluster is massive enough that the merger kick velocities are small compared to the escape velocity, e.g. for a star cluster at the core of a galaxy. Regardless of its limited usability, this simple case illustrates many of the general features that are also present in more complicated cases.

Effects of the mass gaps on the BHMF

The lower mass gap (LG), and the upper mass gap (UG; see Figure 9.1) affect the mass function evolution and produce features at various scales. First, the absence of BHs in the LG reduces the number of BHs of all scales. This is because no BH beyond the LG can merge with BHs in the LG to produce a more massive BH. The size of this reduction depends on the size of the LG, but is degenerate with the normalization of the IMF. As such, it is difficult to conclude anything about the LG, or even infer its existence, through this phenomenon.

Due to the self-similar nature of the constant coagulation kernel, one might expect that the resulting BHMF to also be self similar. However, the gaps in the IMF spoils

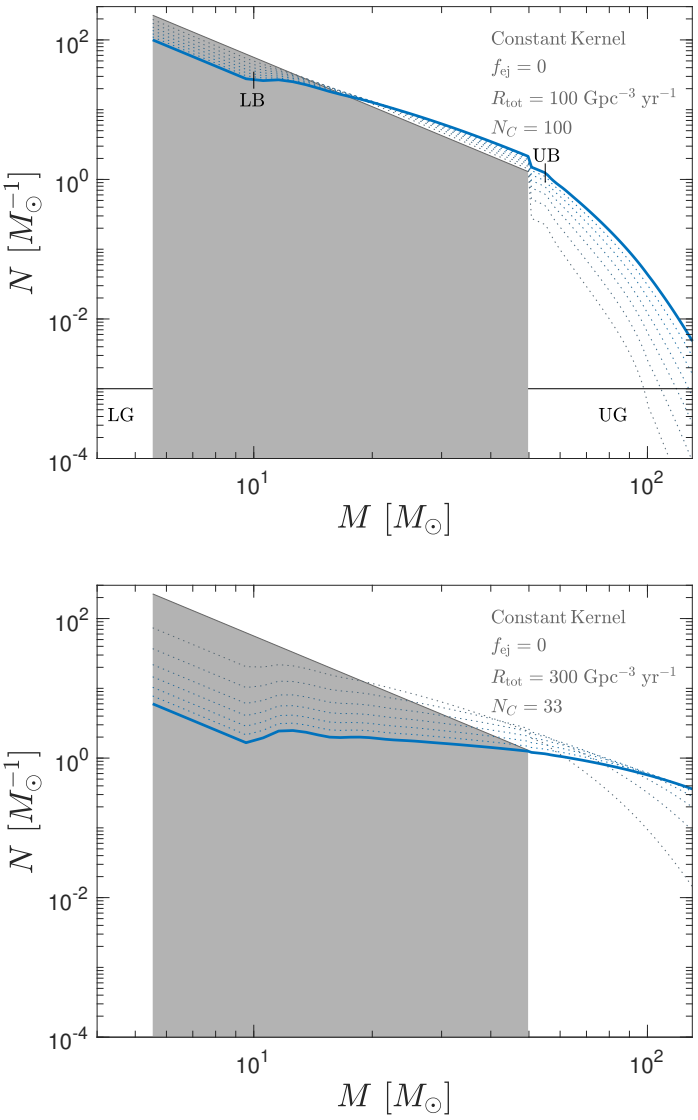

Figure 9.1: The evolution of the BHMF starting from the IMF (black) to 10 Gigayears (solid blue) for a cluster with 1000 BHs. Dotted blue lines represent the BHMF at intervening times. The top figure shows evolution of the mass function with a LIGO rate of 100 Gpc^{-3} yr^{-1} and the number of clusters per MWEG to be $N_C = 100$, while the lower figure shows evolution of the mass function with a LIGO rate of 300 Gpc^{-3} yr^{-1} and $N_C = 33$, i.e. a LIGO rate per cluster that is $\sim$10 times higher. Varying N_C is equivalent to changing the LIGO rate by the reciprocal factor.

this self-similarity. The plots of Figure 9.1 display a break at $M \sim 10M_{\odot}$, which we call the lower break (LB). This break is caused because the BH formation channel where two BHs within the LG merge to form a BH beyond the LG is missing. Because the largest BH that could be formed by this channel is twice the largest BH in the LG, the LB is located at $M = 2M_{\max \mathrm{LG}}$, where the largest BH in the LG, $M_{\max \mathrm{LG}} = 5M_{\odot}$. Changing $M_{\max \mathrm{LG}}$ results in pushing the LG to larger masses. If detected, the existence of the LB can be used to diagnose both the existence and size of the LG.

The interaction of the LG and the UG generates a break at $M \sim 60M_{\odot}$ in Figure 9.1. Because the most massive BHs in the IMF cannot merge with BHs in the LG, there is a dearth of BHs of mass $M_{\min \mathrm{UG}} < M < (M_{\min \mathrm{UG}} + M_{\max \mathrm{LG}})$, where $M_{\min \mathrm{UG}}$ is the most massive BHs in the IMF (the start of the UG). As the mass scale of the UB encodes the mass scale of the LG, an observation of the UB can be used to indirectly measure the size of LG.

The dearth of BHs that caused the LB and UB is also responsible to generating many more weaker breaks. Through a similar mechanism as was discussed in the previous paragraphs, anytime there is a dearth of BHs over a certain mass scale, there is a break due to there being fewer mergers than if the dearth is not present. However, these successive breaks are very weak, and are most probably not observable. Figure 9.2 depicts all of the missing channels discussed in this section.

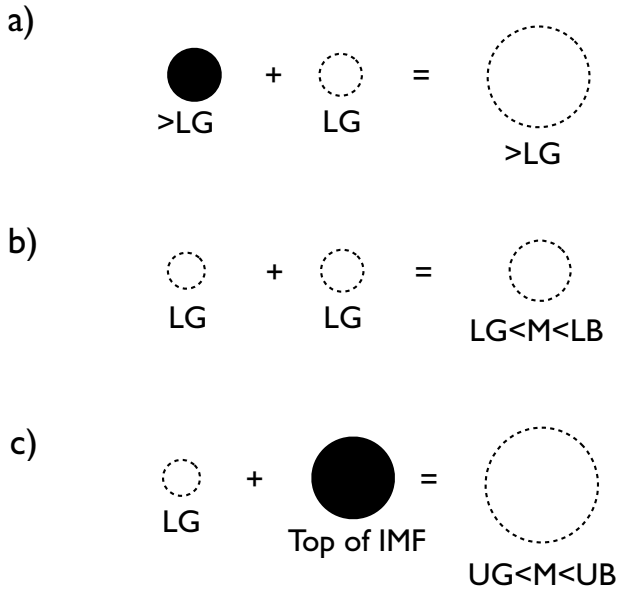

Figure 9.2: Missing BH formation channels due to the existence of the lower mass gap (LG) and the upper mass gap (UG). Case (a) shows that the number of BHs at all scales are lowered because no BH can merge with BHs in the LG to form a larger BH. Case (b) depicts the missing channel responsible for the break at $M = 10M_\odot$ in Figure 9.1, which we call the lower break (LB). Because BHs generated by the mergers of two BHs within the LG is missing, there is a dearth of BH of mass $5M_\odot < M < 10M_\odot$. Case (c) shows the missing channel that results from the interaction of LG and UG. Because BHs from the top of the IMF cannot merge with BHs within LG, there is a dearth of BHs with mass $50M_\odot < M < 60M_\odot$, causing the break at $M = 60M_\odot$ in Figure 9.1.

Effects of varying the number of BHs per cluster

Because the merger rate is calibrated to the observed LIGO rate, clusters containing fewer BHs need to have more efficient mergers than clusters containing more BHs. This is manifested in Equation (9.2) as

$$K \propto \frac{1}{N_{\rm BH}^2} \, . \tag{9.4}$$

Due to this increase in efficiency, for the same LIGO rate clusters can develop a flat BHMF if they contain few BHs. Figure 9.3 shows the evolution of the BHMF over 10 Gyr with the same $R_{\rm LIGO}$ as the first plot of Figure 9.1 with $N_{\rm BH} = 100$. If one assumes that the BHMF is a power law, then situations as shown in Figure 9.3 have to be excluded. Assuming a $R_{\rm LIGO}$ of 10^{-5} yr^{-1} and $N_C = 10$ requires each cluster to contain at minimum ~ 1000 BHs.

9.3.2 Evolution with ejections

In the process of assembling a dynamical binary, or due to the merger kicks experienced by a merged BH, a star cluster is continuously losing BHs. We model the ejection of BHs from the system by introducing a source function, $S(M, t)$, that reduces the number of BHs of mass M by a number that is proportional to the amount of

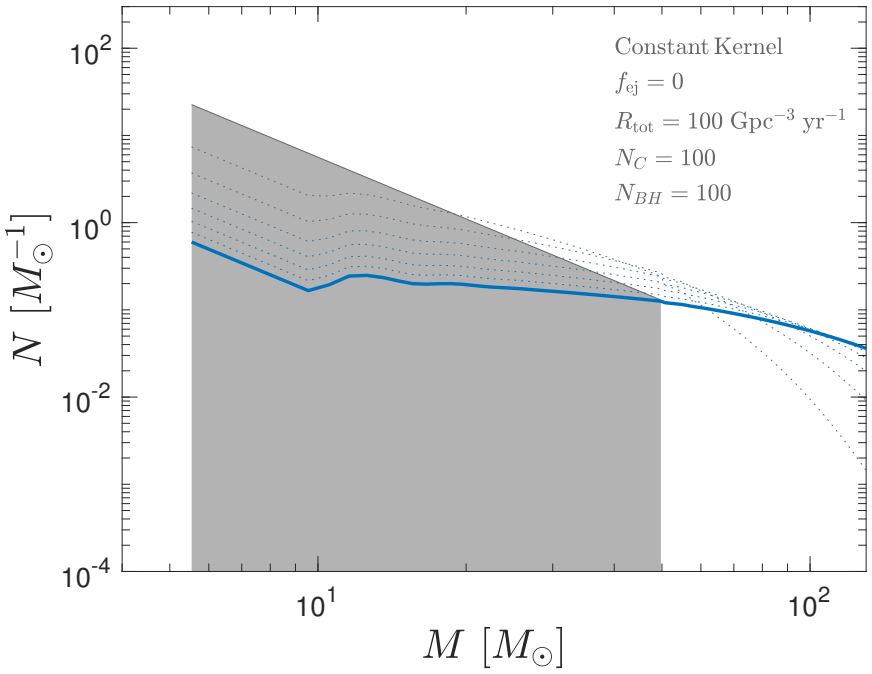

Figure 9.3: The evolution of the BHMF starting from the IMF (black) to 10 Gigayears (solid blue) for a cluster with 100 BHs. Dotted blue lines represent the BHMF at intervening times. The LIGO rate is taken to be 100 Gpc^{-3} yr^{-1}, and the number of clusters per MWEG is taken to be $N_C = 100$. Lowering the number of BHs per cluster flattens the BHMF in a similar way as increasing the LIGO rate.

mergers that produce BHs of mass M,

$$S(M,t) = \\ -\frac{f_{\rm ej}}{2}\int_0^M K(M-M',M')N(M-M',t)N(M',t)\mathrm{d}M' \,, \tag{9.5}$$

where $f_{\rm ej}$ is the ejected fraction. In effect, this source function parameterizes the phenomenon that for every merger, a fraction $f_{\rm ej}$ of the BHs are ejected. While we kept the parameter $f_{\rm ej}$ as a single number, in reality the recoil kicks of binary BHs depend on the spins of the individual BHs. For simplicity, we will neglect the spin dependence of $f_{\rm ej}$.

Note that this parameterization is agnostic toward the actual ejection mechanism. For a given merger, the two BHs that participate in the merger event can be kicked out during their assembly process, or the two BHs can merge, producing a gravitational wave recoil that ejects the merged BH from the cluster. Figure 9.4 shows the evolution of the BHMF for a cluster with an ejection fraction of $f_{\rm ej} = 0.5$ and $f_{\rm ej} = 0.9$.

There are a few main differences between a cluster without ejections and a cluster with efficient ejections. First, ejections lower the normalization of the BHMF, as there are less BHs at all scales. Next, ejections prevent the BHMF from being flattened. Indeed, as shown in the bottom plot of Figure 9.4, even a scenario with a merger rate at the top of the LIGO range ($R_{\rm tot} = 300$ Gpc^{-3} yr^{-1}) fails to flatten the BHMF if

$f_{\rm ej}$ is allowed to be very high. This allows clusters with a low number of BHs ($N_{\rm BH} < 100$), or scenarios with very high merger rate per cluster, to be consistent with the cutoff at $\sim 40 M_\odot$.

In addition to the global properties described in the previous paragraph, efficient ejections also change the properties of the BHMF at certain scales. The LB turns into a step function when ejections are efficient, which might make its detection in the BHMF difficult. As seen in Figure 9.4, for the first few Gigayears there is now a discontinuity at the end of the UB. Because channel (c) in Figure 9.2 is missing, BHs with masses $50 M_\odot < M < 60 M_\odot$ (those between the start of the UG and the UB) are generally formed by fewer mergers than BHs generated beyond the UB. As for every merger, there is a chance to be ejected out of the systems, BHs beyond the UB suffer more ejections than those below the UB. This discontinuity is a signature that the system is efficiently ejecting their BHs, and the drop is larger for higher $f_{\rm ej}$. However, the evolution of the coagulation equation tends to smooth out discontinuities, and the magnitude of the drop is heavily suppressed after 10 Gyr.

9.4 Evolution with top-heavy kernels

Many phenomena responsible for dynamical mergers, such as gravitational capture, mass segregation, and three-body relaxation are mass dependent. Therefore, we would expect that the coagulation kernel in equation (9.1) is in reality a function of mass,

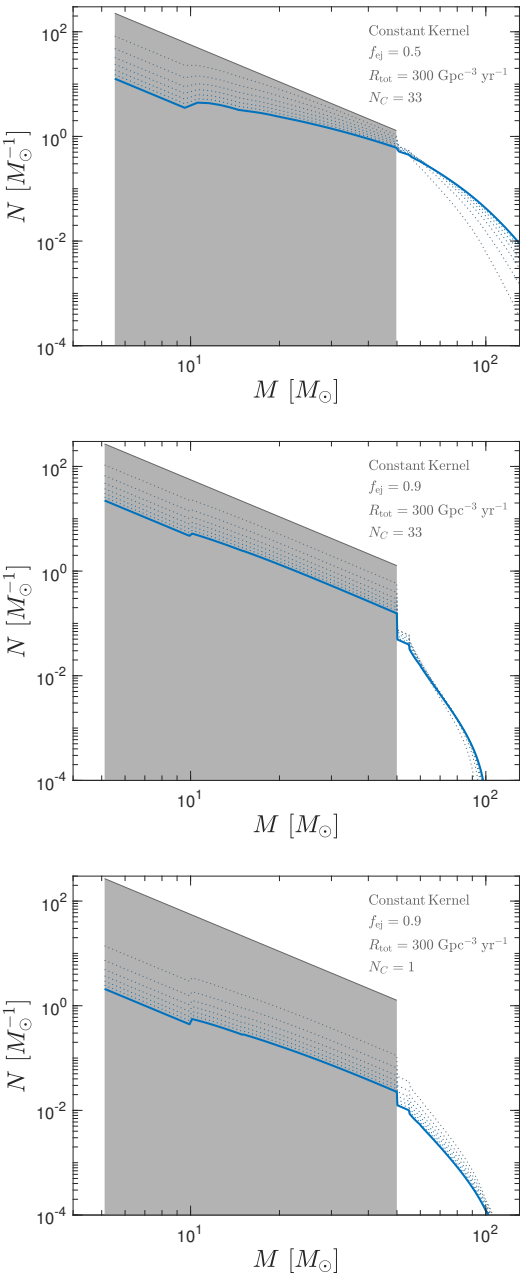

Figure 9.4: The evolution of the BHMF starting from the IMF (black) to 10 Gigayears (solid blue) for a cluster with 1000 BHs. Dotted blue lines represent the BHMF at intervening times. The LIGO rate is taken to be 300 Gpc^{-3} yr^{-1}, and the number of clusters per MWEG is taken to be $N_C = 33$ (top, middle) and $N_C = 1$ (bottom). The ejection fraction is taken to be $f_{\rm ej} = 0.9$. Even for a LIGO rate per cluster of 300 Gpc^{-3} yr^{-1}, the BHMF fails to flatten in 10 Gigayears.

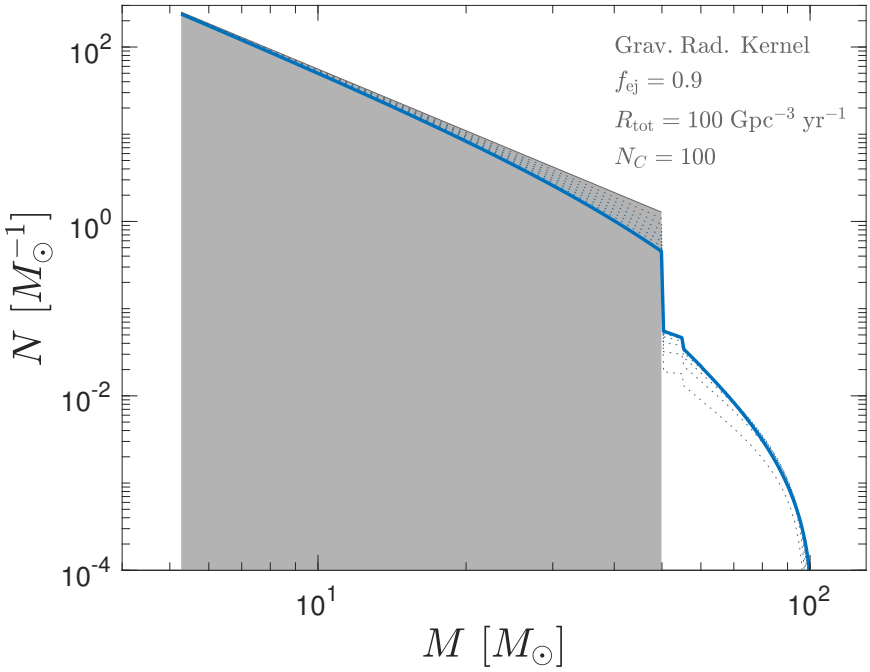

Figure 9.5: The evolution of the BHMF starting from the IMF (black) to 10 Gigayears (solid blue) for a cluster with 1000 BHs for the top-heavy coagulation kernel given by equation (9.7). Dotted blue lines represent the BHMF at intervening times.. The LIGO rate is taken to be 100 Gpc^{-3} yr^{-1}, and the number of clusters per MWEG is taken to be $N_C \sim 100$. The ejection fraction is taken to be $f_{\rm ej} = 0.9$.

$K = K(M, M')$. While the actual form of the coagulation kernel depends on the dominant merging mechanism, it has to be symmetrical with respect to M and M'. In general, this symmetry along with physical considerations forces the functional form of the coagulation kernel to be

$$K \propto (MM')^{\alpha}(M + M')^{\beta}\ , \tag{9.6}$$

with power-law indices α and β. The effectiveness of gravitational processes increases with increasing mass. Gravitational capture, for example, is more efficient for larger M and M'. This implies that heavier BHs merge preferentially, and that K is top-heavy. For example, the coagulation kernel due to gravitational radiation capture scales as (Mouri & Taniguchi 2002)

$$K_{\rm cap} \propto (MM')^{15/14}(M+M')^{9/14} \, . \tag{9.7}$$

Figure 9.5 shows the evolution of the BHMF with the coagulation kernel given by equation (9.7). While the specific values of α and β would matter for the numerical values of f, the salient features of the calculation are valid for general top-heavy kernels. The most important change introduced by the top-heavy kernel is the loss of the power-law behavior in the mass range $5M_\odot < M < 50M_\odot$.

Another example is the coagulation kernel from three-body relaxation, which is computed through numerical simulations to scale as (O'Leary et al. 2016)

$$K_{3-\rm body} \propto (M+M')^4 \, . \tag{9.8}$$

However, Ref. O'Leary et al. (2016) did not fit for the $(MM')^\alpha$ component. In the coagulation equation, the $(MM')^\alpha$ term acts as a regularizer, and its absence generates a runaway growth of BHs that concentrates most of the cluster's mass in a single BH

of extremely large mass $M \gtrsim 1000 M_\odot$. Observationally, we do not see such runaway growth. Thus, in order for this kernel to be consistent with observational bounds in the absence of the $(MM')^\alpha$ term, there must be some maximum $M_{\rm max}$ above which this kernel is suppressed. We impose this regularization by setting the kernel to be $(M_{\rm max} + M')^4$ for $M > M_{\rm max}$. While this introduces a new parameter to the problem, Figure 9.6 shows that even with a very conservative choice of $M_{\rm max} = 100 M_\odot$, a significant population of BHs can be formed within the UG. Indeed, the use of this kernel does not change the main qualitative features of the other kernels, which is the possibility of intermediate mass BH seed formation in dynamical clusters. This echoes a previous result showing that in nuclear star clusters it is possible to obtain BHs in the intermediate mass ranges through multiple mergers (Antonini & Rasio 2016). Our calculations extend this conclusion to the statement that globular clusters are also capable of producing intermediate mass BHs.

9.5 Conclusion

Through evolving a coagulation equation, we have shown that the BHMF in clusters could evolve to fill the gap in the IMF of BHs at $50 M_\odot < M < 130 M_\odot$. Furthermore, we have found that the upper range of the LIGO rate is not consistent with the dearth of BHs with masses $M > 40 M_\odot$ reported by Fishbach & Holz (2017) unless ejection is efficient. The coagulation equation also implies that the mass gap between

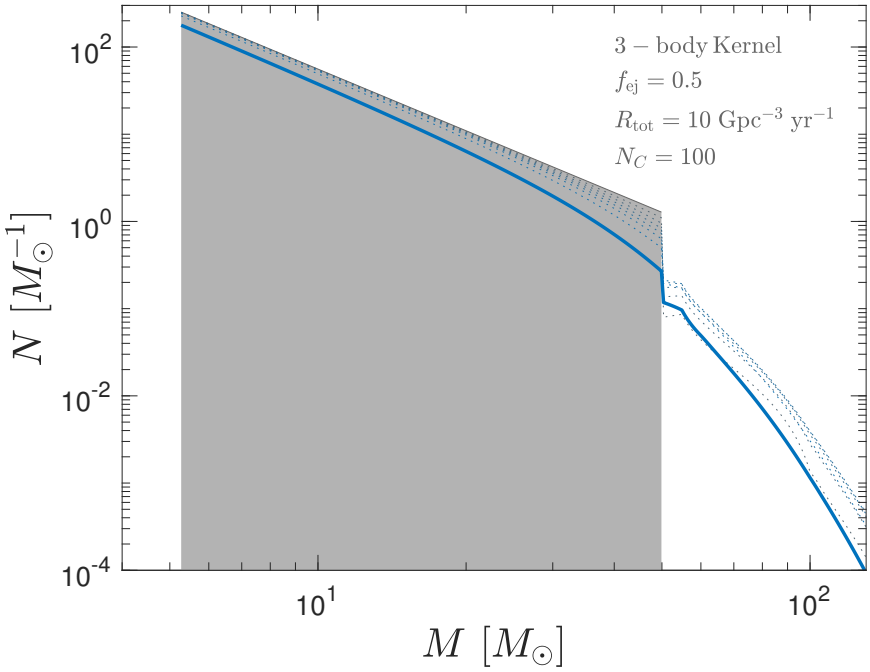

Figure 9.6: The evolution of the BHMF starting from the IMF (black) to 10 Gigayears (solid blue) for a cluster with 1000 BHs for the 3-body coagulation kernel given by equation (9.8). Dotted blue lines represent the BHMF at intervening times.. The LIGO rate is taken to be 10 Gpc^{-3} yr^{-1}, and the number of clusters per MWEG is taken to be $N_C \sim 100$. The ejection fraction is taken to be $f_{\rm ej} = 0.5$ and $M_{\rm max} = 100 M_\odot$.

the most massive neutron stars and the least massive BHs produces potentially observable features at larger scales. In addition, we show that that for top-heavy kernels, the mass function between $5M_\odot < M < 50M_\odot$ is driven away from self-similarity, and that a power-law will not be sufficient to fit the BHMF in this regime. With parameters that are consistent with realistic globular clusters, we showed that it is possible to form intermediate BH seeds through mergers of smaller BHs.

Acknowledgements

The authors would like to thank the anonymous referee, Chris Belczynski, and Tugul-dur Sukhbold for comments on the manuscript. Support (PM) for this work was provided by NASA through Einstein Postdoctoral Fellowship grant number PF7-180164 awarded by the Chandra X-ray Center, which is operated by the Smithsonian Astrophysical Observatory for NASA under contract NAS8-03060. This work was supported in part by Harvard's Black Hole Initiative, which is funded by a grant from the John Templeton Foundation.

9.6 Coagulation equation numerical solver

The coagulation equation is solved using a finite volume method based on Keck & Bortz (2013). The coagulation equation can be written in conservative form as a function of $G(M,t) \equiv M \times N(M,t)$:

$$\partial_t G + \partial_M J(G) = MS \tag{9.9}$$

where

$$J(G) = \int_0^M \int_{M-u}^{M_{\max}} \frac{K(u,v)}{v} G(t,u)G(t,v)\, dv\, du \tag{9.10}$$

is the mass flux across mass bins. G is a conserved quantity in the absence of source terms and conserved by our numerical finite-volume method.

The solution is discretized into mass bins and in time as $G_i^N(t_k)$ which represents the mean value of $G(t_k, M)$ in the mass bin $[M_i, M_{i+1})$ at time t_k. The mass bin has center $M_{\text{mid(i)}}$. The left boundary flux is zero: $J_1^N(t_k) = 0$. In general, the flux $J_r^N(t_k)$ across each discrete boundary x_r can be computed as follows, by considering the aggregation of $M_{\text{mid(i)}}$ and $M_{\text{mid(j)}}$. For each fixed r, and a fixed i such that $M_{\text{mid(i)}} < M_r$, then each j such that $M_{\text{mid(j)}} \geq M_r - M_{\text{mid(i)}}$ gives a contribution to the flux of:

$$\Delta x G_i^N(t_k) \int_{M_j}^{M_{j+1}} \frac{K(M_{\text{mid(i)}}, y)}{y} G_j^N(t_k)\, dy \tag{9.11}$$

A small exception occurs for the lowest j, where the lower limit of integration is $M_{\text{mid(j)}}$ instead of M_j. The integral is evaluated for an arbitrary kernel numerically using a quadrature rule.

The equations are explicitly evolved from time step t_k to t_{k+1} as:

$$G_i^{N\prime} = G_i^N(t_k) + (\Delta t/2) \times M_i S_i(t_k, G_i^N(t_k)) \tag{9.12}$$

$$G_i^{N\prime\prime} = G_i^{N\prime} + \Delta t \frac{J_{i+1}^N - J_i^N(t_k)}{\Delta x} \tag{9.13}$$

$$G_i^N(t_{k+1}) = G_i^{N\prime\prime} + (\Delta t/2) \times M_i S_i(t_k, G_i^{N\prime\prime}) \tag{9.14}$$

that is, adding the source term in two half-steps that sandwich the flux term to result in a second-order method.

10

Detecting gravitational wave lensing with ground-based observatories

We investigate the ability of ground based gravitational wave observatories to detect gravitational wave lensing events caused by stellar mass lenses. We show that LIGO and Virgo possess the sensitivities required to detect lenses with masses as small as

$\sim 30M_\odot$ provided that the gravitational wave is observed with a signal-to-noise ratio of $\sim$ 30. Third generation observatories will allow detection of gravitational wave lenses with masses of $\sim 1M_\odot$. Finally, we discuss the possibility of lensing by multiple stars, as is the case if the gravitational radiation is passing through galactic nucleus or a dense star cluster.

10.1 Introduction

The recent Laser Interferometer Gravitation-Wave Observatory (LIGO) discoveries of gravitational waves from black hole binaries (Abbott et al. 2016c,a) opened a new frontier for the study of astrophysical objects using gravitational radiation. Much like electromagnetic (EM) radiation in classical astrophysics, gravitational radiation can be lensed by massive objects. Lensing of gravitational radiation in linearized General Relativity can be computed with the same techniques as those employed in the familiar lensing of EM waves.

Much of the previous literatures on gravitational lensing of gravitational waves (GWs) focused on lensing in the geometric optics limit (Sereno et al. 2010; Piórkowska et al. 2013), where the wavelength of gravitational waves is small compared to the spatial scale of the lenses and ray optics is sufficient. The lenses responsible for much of the optical depth in this regime are galaxies, which split the gravitational wave signal into copies separated by a time delay of order a few months.

In the wave-optics regime, the Laser Interferometer Space Antenna (LISA) possesses the necessary sensitivities to extract the lens' mass from a lensed signal (Takahashi & Nakamura 2003). The goal of our study is to show that such observations can also be achieved by ground based observatories.

The sensitivities of advanced LIGO (LIGO Scientific Collaboration et al. 2015) and advanced Virgo (Acernese et al. 2015) to lensing by intermediate mass black holes (IMBH) are explored in Ref (Lai et al. 2018), which found that current generation observatories are capable of detecting the lensing IMBH with 98% confidence. Further, Ref (Lai et al. 2018) found that LIGO and Virgo can distinguish between a point mass lens and a singular isothermal lens provided that the redshifted lens mass is $200M_{\odot}$.

In this work, we focus on the capabilities of ground based GW detectors to detect stellar mass lenses. While stellar mass lenses are more numerous than IMBHs, the amplitude of their lensing signal is much smaller. This require us to extend our study to include upcoming third generation gravitational wave detectors.

This paper is organized as follows: in §10.2 we describe our lensing formalism, in §10.3 we discuss our method for inferring the sensitivities of the GW detectors to lensing events. Subsequently §10.4 presents our results. In §10.5 we discuss the possibility of lensing by multiple lenses. Finally §10.6 summarizes our conclusions.

10.2 Background and notations

We consider GWs in the perturbed Friedmann-Lema tre-Robertson-Walker (FLRW) metric, written in terms of the conformal time η,

$$ds^2 = a^2 \left[-(1+2U)\, d\eta^2 + (1-2U)\, d\mathbf{r}^2 \right] \ , \tag{10.1}$$

where $\mathbf{r}$ is the spatial coordinate, U is the gravitational potential of the lenses, and a encodes the universal scale factor. Considering linear perturbation on this metric,

$$g_\alpha \beta = g^B_{\alpha\beta} + h_{\mu\nu}, \tag{10.2}$$

where $h_{\mu\nu}$ is separated into its amplitude ϕ and polarization $e_{\mu\nu}$,

$$h_{\mu\nu} = \phi e_{\mu\nu} \ , \tag{10.3}$$

one can obtain that the equation of motion for ϕ is simply given by the wave equation,

$$\partial_\mu \left(\sqrt{-g^B} g_B^{\mu\nu} \partial_\nu \phi \right) = 0 \ , \tag{10.4}$$

where g^B is the determinant of the metric. In Fourier space, $\tilde{\phi}(f, \mathbf{r})$, the equation reads

$$\left(\nabla^2 + \tilde{\omega}^2\right) \tilde{\phi} = 4\tilde{\omega}^2 U \tilde{\phi} \,, \tag{10.5}$$

where $\tilde{\omega} = 2\pi f$ is the GW frequency. Following (Takahashi & Nakamura 2003), we define the amplification factor $F(\omega, \mathbf{r})$ as the ratio between the lensed and unlensed $\tilde{\phi}$.

The setup of our problem consists of three parallel planes, called the source, lens, and observer planes. The angular diameter distances along the normal from the observer plane to the source and lens planes are labelled D_S and D_L, respectively, while the distance between the source and lens planes is labelled as D_{LS}. GWs are emitted by a point in the source plane, travel freely to the lens plane, where they are lensed by a gravitational potential U that is assumed to be localized in the thin (width $\ll c/f$) lens plane, before reaching the telescope at the observer plane.

Coordinates can be set up on the three planes. We use the notation of Ref (Nambu 2013; Takahashi & Nakamura 2003), where ξ is the coordinate at the source plane, η is the coordinate at the lens plane, and δ is the coordinate in the observer plane. We

also employ the following dimensionless coordinates,

$$\begin{aligned}
\mathbf{x} &= \frac{\xi}{\xi_0} \,, \\
\mathbf{y} &= \frac{D_L}{D_S}\frac{\eta}{\xi_0} \,, \\
\mathbf{d} &= \left(1 - \frac{D_L}{D_S}\right)\frac{\mathbf{\Delta}}{\xi_0} \,,
\end{aligned}$$

where ξ_0 is some characteristic length-scale defined by $\xi_0 = D_L\theta_E$ where θ_E is the Einstein angle for a point mass lens,

$$\theta_E^2 = \frac{4GM}{c^2}\frac{D_{LS}}{D_L D_S} \,. \tag{10.6}$$

Furthermore, we will work with the dimensionless frequency,

$$\omega = \frac{D_S \xi_0^2}{D_{LS} D_L}\tilde{\omega} \,. \tag{10.7}$$

Note that for the point mass lens, $\omega = 4M_L(1+z)\tilde{\omega}$, where M_L and z are the lens' mass and redshift, respectively, and we adopt units where $G = c = 1$ from now on.

Using this setup, the solution of Equation (10.5) is given by the Fresnel-Kirchhoff integral,

$$F(\omega, \mathbf{y}) = \frac{\omega}{2\pi i}\int d^2x \exp\left[i\omega T(\mathbf{x}, \mathbf{y})\right] \,, \tag{10.8}$$

where the time delay function, $T(\mathbf{x}, \mathbf{y})$ is given by

$$T(\mathbf{x}, \mathbf{y}) = \frac{1}{2} (\mathbf{x} - \mathbf{y} - \mathbf{d})^2 - \Psi(\mathbf{x}) \ , \tag{10.9}$$

with Ψ being the lensing potential.

10.2.1 Wave optics lensing

Integrating Equation (10.8) with the stationary phase method is valid when the wavelength is much smaller compared to the characteristic scale of the lens. For a point mass, this condition requires,

$$\omega = \frac{4GM_L(1+z)}{c^3}\tilde{\omega} \gg 1 \ , \tag{10.10}$$

where we have reintroduced factors of G and c just in this equation. A detector operating in the frequency band of LIGO, with a characteristic frequency of $f \sim 100$ Hz, is capable of detecting lenses where $\omega \ll 1$. In this regime, the geometric optics approximation breaks down and one has to integrate Equation (10.8) in full.

For a point mass lens located at $\eta = 0$, $\psi(\mathbf{x}) = \log|\mathbf{x}|$, and Equation (10.8) inte-

grates to (Peters 1974; Takahashi & Nakamura 2003),

$$F(\omega) = \exp\left\{\frac{\pi\omega}{4} + i\frac{\omega}{2}\left[\log\left(\frac{\omega}{2}\right) - 2\phi_m(y)\right]\right\}\Gamma\left(1 - \frac{i}{2}\omega\right) \times_1 F_1\left(\frac{i}{2}\omega, 1; \frac{i}{2}\omega y^2\right) , \tag{10.11}$$

where

$$\phi_m(y) = (x_m - y)^2/2 - \log x_m , \tag{10.12}$$

and

$$x_m = \frac{y + \sqrt{y^2 + 4}}{2} . \tag{10.13}$$

The amplification for $\omega \sim 0.01 - 0.1$ and a variety of y values is plotted in Figure 10.1. For a frequency of 100Hz, this corresponds to lenses of mass $1 - 10 M_\odot$. If the projected separation between the source and the lens is small, the amplification is approximately linear in ω. For large separations, the amplification factor hovers around 1, as expected from the notion that distant lenses with large impact parameter should not affect the GW signal.

10.3 Method

To verify if and to which extent the presence of stellar-mass lenses can be inferred from GW measurements, we have modified the parameter estimation algorithm currently used by the LIGO and Virgo collaborations Veitch et al. (2015); Abbott et al.

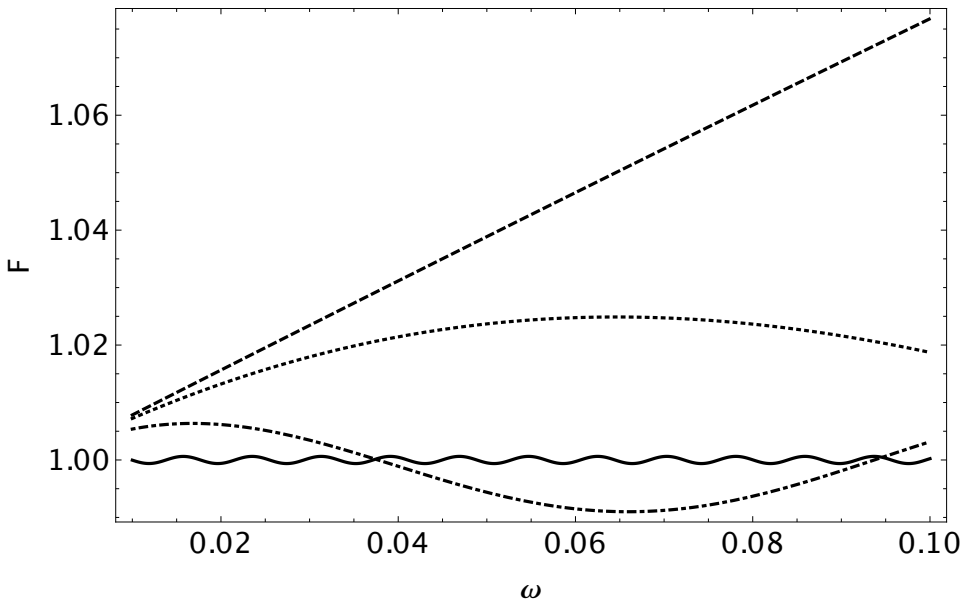

Figure 10.1: The amplification as a function of ω for a point mass lens where $y = 1, 5, 10, 40$ (dashed, dotted, dot-dashed, and solid). When the position of the source projected to the lens plane is small ($y \sim 1$), one can obtain amplification that is $\sim$linear in ω. In the LIGO band ($\omega \sim 0.01 - 0.1$ for a solar mass lens) this results in a deviation from the unlensed signal of a few percent. As the distance increases, the amplitude of the deviation becomes smaller.

(LIGO and Virgo Scientific Collaboration) (2016) to allow for the presence of a lens along the line of sight to the source. This is a stochastic sampler that explores the parameter space and produces posterior distributions for the unknown parameters on which the gravitational-wave signal depends. In absence of a lens, these include masses and spins of the two compact objects, the sky position, distance, orientation and polarization of the source, as well as the time and phase at coalescence Abbott et al. (LIGO and Virgo Scientific Collaboration) (2016). Throughout this work, we use the effective-precession waveform IMRPhenomPv2 Hannam et al. (2014).

Our lens model allows for two extra parameters: the mass of the lens, M_L, and the parameter $y' \equiv yM_L$, which are sampled together along the other. Once a waveform corresponding to the unlensed signal is generated, $h_{\rm Unlensed}(\vec{\theta})$, the two lens parameters are used to calculate Eq. (10.11), which yield the lensed signal $h_{\rm Lensed}(\vec{\theta}, M_{\rm lens}, y') = F(M_{\rm lens}, y')h_{\rm Unlensed}(\vec{\theta})$, where $\vec{\theta}$ are the Compact Binary Coalescence (CBC) parameters in absence of lens.

Given a GW signal (real or simulated) the algorithm can be run with the lens parameters ("Lens" model) to measure or put an upper bound on the lens mass. After the evidence Jaynes (2003) for both the "Lens" and "No lens" model is calculated, one can compute the odds ratio defined as

$$\text{Odds} = \frac{\text{P(lens|data)}}{\text{P(no lens|data)}} \,. \tag{10.14}$$

For sources with an odds ratio much larger than unity, the lensed model is preferred over the model without lensing.

10.4 Results

10.4.1 Current Generation Observatories

We ran our code on simulated signals observed by LIGO and Virgo with signal-to-noise (SNR) values of $15, 30$, and 60, where we injected lenses of $0, 1, 10, 20, 30, 60$ and $100 M_{\odot}$ with an impact parameter of an Einstein angle, θ_E. The masses of the simulated CBC signal are compatible with heavy binary source similar to GW150914.

The results are plotted in Figure (10.2). At a SNR ratio of 30, which is moderately high for current generation observatories, lenses can be detected at $> 3\sigma$ when they possess masses larger than $\sim 30 M_{\odot}$. Higher SNR events allowed smaller lenses to be detected. At SNR$= 60$, lenses as small as $\sim 10 M_{\odot}$ can be detected. LIGO and Virgo can potentially detect smaller lenses if the impact parameter is significantly smaller than an Einstein radius, but such cases are expected to be rare.

The GW SNR scales as

$$\text{SNR} \propto \frac{M_c^{5/3}}{D_s} \, , \tag{10.15}$$

where M_c is the chirp mass and D_s the source angular diameter distance. Requiring a high SNR amounts to either limiting the search volume to small D_s or requiring mergers of massive black holes. Explicitly, if lenses are uniformly distributed in space,

the number of lensing events, $N_{\rm lens}$, scales as D_s^3, which results in

$$\mathrm{SNR} \propto \frac{M_c^{5/3}}{N_{\rm lens}^{1/3}} \,. \tag{10.16}$$

Furthermore, while the explicit form of the binary black hole mass function is still uncertain, it is expected to inherit the bottom-heavy characteristic of the mass function of massive stars. Therefore, requiring a high chirp mass will further reduce the number of detectable lensing events.

As a straightforward application, we ran our algorithm on the stretch of public LIGO data containing the gravitational wave event GW150914 Abbott et al. (2016); LIGO Collaboration (2016). We found that the waveform detected for GW150914 is consistent with a lens mass of $M = 0$, i.e. GW150914 is most probably not a lensed event with an upper bound 90% confidence interval for the lens mass of $50 M_\odot$.

10.4.2 Third Generation Observatories

Proposed ground based third-generation (3G) GW observatories, such as the Einstein Telescope Punturo et al. (2010) and the Cosmic Explorer Abbott et al. (2017a), allow detections of BBH events from high redshift Abbott et al. (2017a); Vitale & Evans (2017); Team (2011), and will detect nearby events with SNR of hundreds or thousands Vitale (2016). Such high SNR events can potentially allow much smaller lenses to be detected. To show this, we ran our algorithm on a simulated GW150914-like

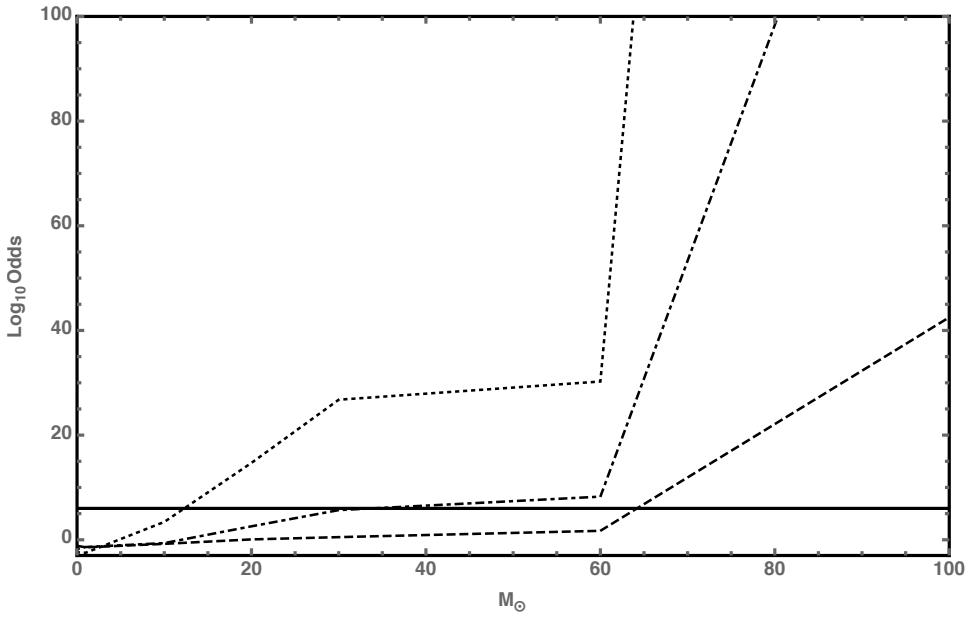

Figure 10.2: The odds ratio computed as defined by Equation (10.14). The dashed, dot-dashed, and dotted lines denote SNR values of $10, 30$, and 60, respectively. Odds values > 1 indicate that the lensed model is preferred over the unlensed model. The dashed line indicates the 3σ line.

source as observed by a third generation observatory, with an injected lens of $1M_\odot$. Figure 10.3 shows the resulting posterior distribution for the lens mass. As seen in Figure 10.3, 3G observatories can detect lenses as small as $1M_\odot$. As there are much more lenses with such masses than those with masses of $\sim 30M_\odot$, we expect that detection of lensing events by stellar mass lenses will be mostly confined to 3G detectors. If the lenses obey the mass function for stars, the number of events that we can expect from a 3G detector is greater than that of current generation detectors by a factor q, where

$$q = \frac{R_{\rm 3G}}{R_{\rm CG}} \frac{\int_{1M_\odot}^{\infty} m^{-2.3} dm}{\int_{30M_\odot}^{\infty} m^{-2.3} dm} \approx \frac{R_{\rm 3G}}{R_{\rm CG}} 100 \ , \tag{10.17}$$

where $R_{\rm 3G}$ is the rate of gravitational wave detection by 3G observatories, $R_{\rm CG}$ is the rate of gravitational wave detection by current generation observatories, and we have taken the stellar mass function to be of the Salpeter form (Salpeter 1955). Note that we have not fully explored the lower limit of the masses of the lenses that is still detectable by third generation observatories. It is likely that these observatories will detect lenses with masses even smaller than $1M_\odot$.

10.5 Wave optics lensing by multiple masses

The centers of galaxies are dense enough that the Einstein ring of stars (on an angular scale of $\sim 1\mu$arcsecond) can overlap. Indeed, the probability for there to be another

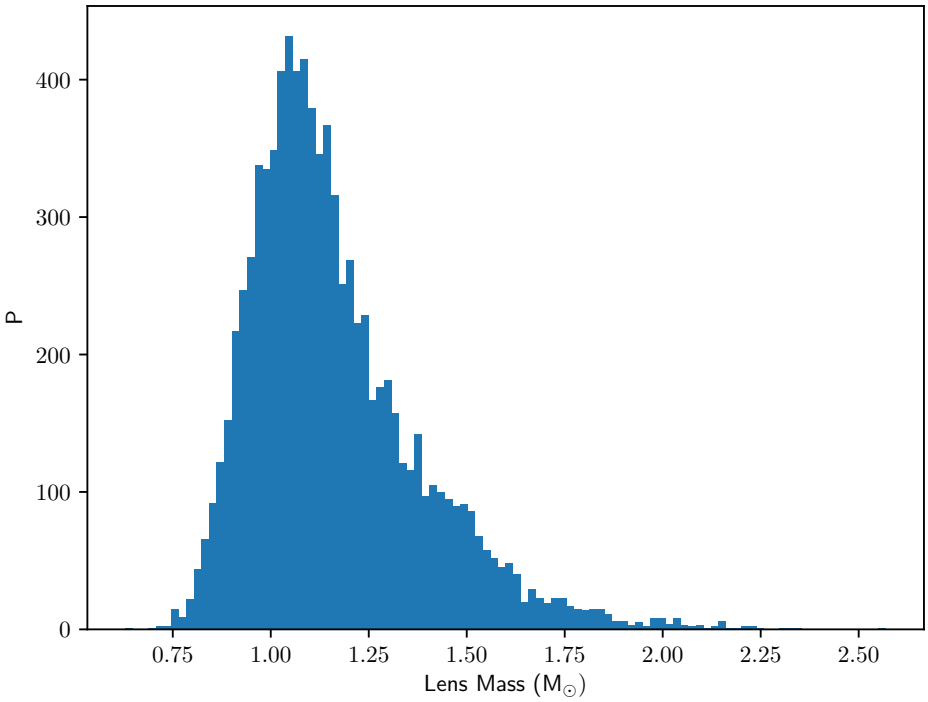

Figure 10.3: The resulting posterior distribution of lens mass for an event with an $M = 1M_\odot$ lens observed by a third generation observatory. SNR is set to 3000 and impact parameter is an Einstein radius. Note that a vanishing lens mass is clearly excluded.

star an Einstein radius, ξ_0, away from a particular star is (Phinney 1993; Christian & Loeb 2015)

$$P \approx 1 - \exp\left[-\sigma\pi\xi_0^2\right] , \tag{10.18}$$

which approaches unity for a stellar mass density, σ, corresponding to ~ 1 g cm^{-2}.

In this regime, it is important to understand the effects of lensing by multiple masses. Assuming that the lensing happened in a thin plane, the lensing potential by N point masses is given by

$$\psi(\mathbf{x}) = \sum_i^N \log|\mathbf{x} - \mathbf{x_i}| . \tag{10.19}$$

To simplify our calculation, we employ the fact that distant lenses do not affect the signal by imposing a cutoff on $\psi(\mathbf{x})$. In particular, we will ignore any lenses that are more than an Einstein radius away from the source,

$$\psi(\mathbf{x}) \approx \sum_i^N H(|\mathbf{x} - \mathbf{x_i}|) \log|\mathbf{x} - \mathbf{x_i}| , \tag{10.20}$$

where $H(|\mathbf{x} - \mathbf{x_i}|)$ is a tophat kernel that is unity when $|\mathbf{x} - \mathbf{x_i}|$ is less than an Einstein radius, and zero otherwise. In doing so, we do not need to include all the point masses in the lensing galaxy in $\psi(\mathbf{r})$, but only the lenses whose Einstein rings intersect. Obviously, this number depends on the surface density number of stars in the lensing galaxy.

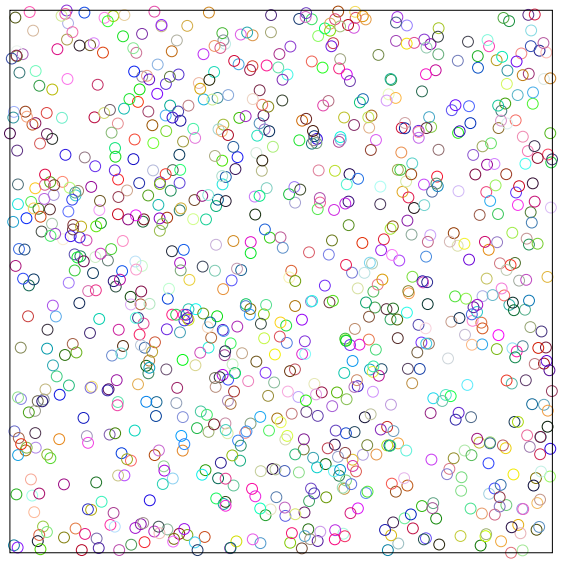

Figure 10.4: The lensing plane of a galactic nucleus within $\sim$ 100 Einstein radii. The circles correspond to the Einstein rings of $\sim 1 M_{\odot}$ stars randomly distributed in the plane. The number of stars in the field corresponds to the upper limit of Ref (Hopkins et al. 2010). For this extremely dense system, the probability of intersections of Einstein rings is only a few tenths of a percent.

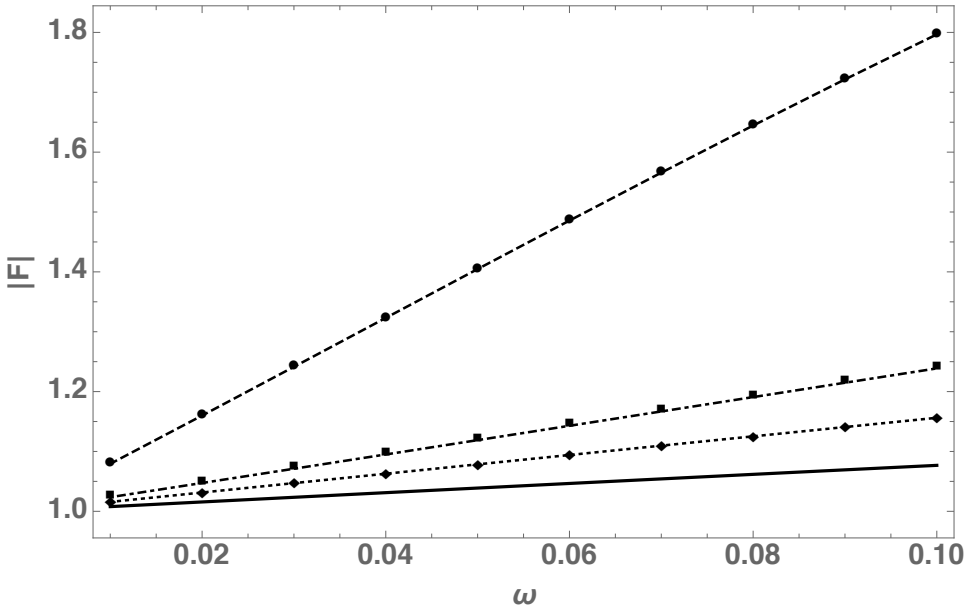

Figure 10.5: The amplification factor due to lensing as a function of ω for 1 (analytical solid line), 2, 3, and 10 (dotted, dot-dashed, and dashed, respectively) point mass lenses. For $1M_{\odot}$ lenses, the ω range corresponds to the LIGO frequency range. The lenses are distributed randomly, but consistently in the lens plane, so that the two lens case corresponds to the single lens case plus a randomly distributed second lens, and similarly for the 3 and 10 lenses cases. The position of the source in the source plane is $(0, 1)$, and the position of the observer in the observer plane is $(0, 0)$ in Einstein angle units. In this regime where $F(\omega) \propto \omega$, more lenses generally generate a larger lensing effect.

The upper limit on the stellar surface mass density in a dense system is $\Sigma_{\rm max} \sim 10^{11} M_\odot/{\rm kpc}^2$ (Hopkins et al. 2010). Assuming that most of the stellar mass is in stars of mass $\sim 1 M_\odot$, this gives a surface number density of $\sim 10^5$ pc^{-2}. Using the fact that at cosmological distances, the Einstein angle of such stars are $\sim 1\mu$arcsecond, and that stars are randomly distributed in the lensing plane, we created realizations of star fields in the lensing plane. One such realization is shown in Figure 10.4. Even for such a dense system, the number of Einstein ring intersections is of order a few. The expected number of overlapping Einstein rings, N_O, can be estimated as follows. If $A_1 = 1/\sigma$ is the area where only one star is expected, then

$$N_O = \frac{\pi(2\xi_0)^2}{A_1} = \pi(2\xi_0)^2\sigma \tag{10.21}$$

$$= 4.3 \times \left(\frac{\sigma}{10^5/{\rm pc}^2}\right) . \tag{10.22}$$

We therefore expect GWs to be significantly lensed by only a few lenses. However, as a Poisson process, N_O is Poisson distributed. Therefore, for a $\sigma = 10^5$ pc^{-2} system, there is a $\sim 1\%$ chance for the beam to interact with ~ 10 lenses.

To this end we calculate the lensing amplitude $F(\omega)$ by numerically integrating Equation (10.8) using a Levin method integrator (Moylan et al. 2008). The resulting magnification amplitudes for 2, 3, and 10 lenses are plotted in Figure (10.5). For $1 M_\odot$ lenses in the LIGO band, $F(\omega)$ scales linearly with ω. The general trend is that more lenses yield a larger deviation in amplitude. This means that if a lensing event is de-

tected at low ω, it might be difficult to distinguish between lensing by a single point mass or lensing by multiple point masses. However, if a larger range of ω is observed, these two models will differ significantly.

10.6 Conclusions

We have shown that in order for current generation GW observatories to detect gravitational wave lensing events, a lens mass of at least $\sim 30M_{\odot}$ is required, provided that the gravitational waveform is detected at a signal to noise of ~ 30. If the gravitational wave source is weaker or is located further away, this number will increase correspondingly.

Furthermore, we have shown that 3G detectors can detect lenses of masses as small as $1M_{\odot}$. Since $1M_{\odot}$ lenses are much more numerous than $\sim 30M_{\odot}$ lenses, many more lensing events will be detected by third generation detectors than current generation detectors.

Finally, we discussed the possibility that a GW signal can be lensed by multiple stars. We have shown that when detected at small ω, multiple lenses can masquerade as a larger lens.

10.7 Acknowledgements

This work was supported in part by the Black Hole Initiative at Harvard University, which is funded by a grant from the John Templeton Foundation.

11

Conclusions

In this dissertation, we have proposed methods to peel back the mystery behind black holes through a variety of astronomical observations. In this chapter we conclude this dissertation with a synopsis of its results and a description of future work that could be done to extend said results.

In Chapters 2 and 3, we have shown that the effects of the supermassive black hole

Sgr A* at the center of the Milky Way on its surroundings can be probed by astronomical observations. Following that, Chapter 4 showed that the effects of such supermassive black holes on the trajectory of hot plasma close to their horizons could be used to constraint their spacetime parameters.

Chapter 5 and 6 questioned whether we have the correct understanding of gravity to model astrophysical black holes. In these chapters we proposed some astronomical tests that could address such queries. We showed that a "perturbation" of Einstein's General Relativity could lead to modifications in both the electromagnetic fields surrounding a black hole, as well as in signals of pulsars orbiting close to a black hole.

The next three chapters in this dissertation are concerned with gravitational radiation. Chapters 8 and 9 proposed that the population and distribution of black holes can be constrained by gravitational observables. In Chapter 8, we showed that the merger rate measured by LIGO is consistent with a LISA detection of a binary black hole in the Milky Way. In Chapter 9, we demonstrated that this merger rate is large enough that the black hole mass function in dynamical clusters can be heavily modified by mergers. Finally, Chapter 10 proposed the possibility of detecting gravitational lensing events of gravitational waves. Such events could be used to probe both the structure and population of the lenses, as well as provide a novel way to study gravitational radiation themselves.

11.1 Future outlook

I intend to build on the line of research presented in Chapters 2 and 3. In particular, the black hole influence on the GC region causes it to possess extreme levels of density and temperature. In addition, the orbits of stars and gas in the GC are also heavily modified by the black hole gravity. I intend to study the GC region to better understand how the black hole affects astrophysical phenomena such as star formation and stellar migration. One way to accomplish this is to have a direct comparison between theoretical models and 21-cm observation of the neutral gas in the GC. As neutral disks are hotbeds of star formation, the effects of the black hole on the neutral disk will modify the resulting star formation at the GC. I plan to expand our previous calculations to facilitate these comparisons. In particular, numerical simulations of the photosphere are required in lieu of the simple model used in previous works, and gravitational instabilities of the neutral disk need to be further explored through both analytical and numerical computations to properly understand the black hole effects on star formation.

Further, the interaction of Sgr A* with its surrounding plasma generates highly variable emissions at a vast range of wavelengths (e.g Yusef-Zadeh et al. 2006; Hora et al. 2014; Capellupo et al. 2017), and I intend to improve theoretical models of these variabilities. Popular models describing these emissions include the expanding plasmon model (Yusef-Zadeh et al. 2006) and the orbiting hotspot model (Broderick

& Loeb 2005). In the expanding plasmon model, a plasma blob of relativistic electrons emits via synchrotron radiation. This blob expands adiabatically, producing the temporal variability observed in Sgr A* flares. In the orbiting hotspot model, the existence of bright inhomogeneities, called hotspots, in the black hole accretion disk is posited. These hotspots move along with the accretion flow, and the observed flux variabilities result from a combination of the Doppler effect and gravitational lensing as the bright hotspots orbit the black hole.

Currently, the effects of the black hole tidal field are neglected in these models. However, in the expanding plasmon model, the black hole tidal field can strongly modify the expansion of the plasma blob. Similarly, the tidal shear can shred orbiting hotspots as they travel around the black hole. I intend to add this crucial element to these models. The tidal field of the black hole can be computed in GR through the geodesic deviation formalism. In Chapter 4, we had used this method to study the expansion of generic blobs as it is ejected from the black hole. I intend to further apply this formalism to the expanding plasmon and orbiting hotspot systems. This calculation will include the magnetic forces in the plasma as well as relativistic computations of the radiation field. Linking this project with my interest on tests of strong gravity, I also plan to explore the effects of violations of the no-hair theorem on the black hole tidal field. These studies will culminate in better theoretical models of Sgr A* variabilities that can be tested against observations across multiple wavebands.

Further, the study in Chapters 5 was conducted in an idealized system where the

magnetic field is produced by faraway sources that are not affected by the black hole gravity. In contrast, realistic magnetic fields are flux-frozen to the plasma in the black hole accretion disk, requiring us to solve the plasma equations subject to the black hole gravitational field in addition to the Maxwell's equations. I intend to follow this work with more sophisticated computations that allow evolution of the black hole plasma. A first step will be to utilize the equations of force-free electrodynamics, valid in regions of strong magnetic fields. In the past, geometric methods had been employed to study force-free electrodynamics around no-hair compliant black holes (Gralla & Jacobson 2014; Lupsasca et al. 2014), and I intend to apply the technique to black holes with arbitrary quadrupoles.

In addition to studies of the magnetosphere, I also plan to explore previously unexamined signatures of violations of the no-hair theorem. In particular, a non-Kerr quadrupole can modify both the spectral signature and rates of tidal disruption events. In addition, I also intend to study the production of high energy particles through both plasma effects and the Bañados-Silk-West effect (Bañados et al. 2009) around no-hair violating black holes.

These studies will facilitate comparisons with observational data, including the submillimeter polarimetric images taken by the Event Horizon Telescope, signals of X-ray outbursts detectable by the Chandra X-ray Observatory, and variabilities in the infrared observable by the Spitzer Space Telescope or the upcoming James Webb Space Telescope.

On the gravitational waves front, I plan to use detections from Advanced LIGO and Virgo, 2nd generation gravitational wave observatories that have just started taking data, to markedly improve these constraints presented in Chapter 8. Further, the current formalism does not take into account the possibility of particular formation mechanisms that produce extremely eccentric binary BHs. Through further analytical study aided with some numerical simulations, I intend to generalize the formulation to allow for these possibilities, as well as extend the analysis to cosmological distances. The computations in Chapter 9 can also be improved by considering more realistic prescriptions for the coagulation kernel and ejection efficiency. With such realistic parameters in place, one can then use the coagulation formalism to investigate the possibility of forming intermediate mass black hole seeds through black hole mergers.

Finally, now that Chapter 10 has established the possibility of detecting gravitational waves lensing events, the next step is to ask what could be learned from events. Historically, the gravitational lensing of light was used as a test of gravity (Dyson et al. 1920). In similar veins, the signal from a gravitational wave lensing event could be used to test the validity of our gravitational wave solutions. If it is observed that gravitational waveforms are lensed differently than predicted by general relativity, then we will know that either our knowledge of gravity or the propagation of spacetime perturbations is flawed. In addition, as with the gravitational lensing of light, a gravitational wave lensing event will also carry information about the lensing mass, allowing us to study the nature of these lenses. In this ironic way, merging black holes

will illuminate the cosmos.

REFERENCES

Abbott, B. P., Abbott, R., Abbott, T. D., Abernathy, M. R., Acernese, F., Ackley, K., Adams, C., Adams, T., Addesso, P., Adhikari, R. X., & et al. (2016a). GW151226: Observation of Gravitational Waves from a 22-Solar-Mass Binary Black Hole Coalescence. Physical Review Letters, 116(24), 241103.

Abbott, B. P., Abbott, R., Abbott, T. D., Abernathy, M. R., Acernese, F., Ackley, K., Adams, C., Adams, T., Addesso, P., Adhikari, R. X., & et al. (2016b). Observation of Gravitational Waves from a Binary Black Hole Merger. Physical Review Letters, 116(6), 061102.

Abbott, B. P., Abbott, R., Abbott, T. D., Abernathy, M. R., Acernese, F., Ackley, K., Adams, C., Adams, T., Addesso, P., Adhikari, R. X., & et al. (2016c). Observation of Gravitational Waves from a Binary Black Hole Merger. Phys. Rev., 116(6), 061102.

Abbott, B. P., Abbott, R., Abbott, T. D., Abernathy, M. R., Acernese, F., Ackley, K., Adams, C., Adams, T., Addesso, P., Adhikari, R. X., & et al. (2016d). The Rate of Binary Black Hole Mergers Inferred from Advanced LIGO Observations Surrounding GW150914. ApJ, 833, L1.

Abbott, B. P., Abbott, R., Abbott, T. D., Abernathy, M. R., Ackley, K., Adams, C., Addesso, P., Adhikari, R. X., Adya, V. B., Affeldt, C., & et al. (2017a). Exploring the sensitivity of next generation gravitational wave detectors. Classical and Quantum Gravity, 34(4), 044001.

Abbott, B. P., Abbott, R., Abbott, T. D., Acernese, F., Ackley, K., Adams, C., Adams, T., Addesso, P., Adhikari, R. X., Adya, V. B., & et al. (2017b). GW170104: Observation of a 50-Solar-Mass Binary Black Hole Coalescence at Redshift 0.2. Physical Review Letters, 118(22), 221101.

Abbott, B. P., Abbott, R., Abbott, T. D., Acernese, F., Ackley, K., Adams, C., Adams, T., Addesso, P., Adhikari, R. X., Adya, V. B., & et al. (2017c). GW170608: Observation of a 19 Solar-mass Binary Black Hole Coalescence. ApJ, 851, L35.

Abbott, B. P., Abbott, R., Abbott, T. D., Acernese, F., Ackley, K., Adams, C., Adams, T., Addesso, P., Adhikari, R. X., Adya, V. B., & et al. (2017d). GW170814: A Three-Detector Observation of Gravitational Waves from a Binary

Black Hole Coalescence. Physical Review Letters, 119(14), 141101.

Abbott, B. P., Abbott, R., Abbott, T. D., et al. (2016). Observation of gravitational waves from a binary black hole merger. Physical Review Letters, 116, 061102.

Abbott et al. (LIGO and Virgo Scientific Collaboration), B. P. (2016). Properties of the Binary Black Hole Merger GW150914. Physical Review Letters, 116(24), 241102.

Abdujabbarov, A. & Ahmedov, B. (2010). Test particle motion around a black hole in a braneworld. Phys. Rev. D, 81, 044022.

Abdujabbarov, A., Ahmedov, B., & Hakimov, A. (2011). Particle motion around black hole in hořava-lifshitz gravity. Phys. Rev. D, 83, 044053.

Abdujabbarov, A. A., Ahmedov, B. J., & Jurayeva, N. B. (2013). Charged-particle motion around a rotating non-kerr black hole immersed in a uniform magnetic field. Phys. Rev. D, 87, 064042.

Acernese, F. et al. (2015). Advanced Virgo: a second-generation interferometric gravitational wave detector. Class. Quant. Grav., 32(2), 024001.

AlGendy, M. & Morsink, S. M. (2014). Universality of the Acceleration due to Gravity on the Surface of a Rapidly Rotating Neutron Star. ApJ, 791, 78.

Amaro-Seoane, P., Aoudia, S., Babak, S., Binétruy, P., Berti, E., Bohé, A., Caprini, C., Colpi, M., Cornish, N. J., Danzmann, K., Dufaux, J.-F., Gair, J., Jennrich, O., Jetzer, P., Klein, A., Lang, R. N., Lobo, A., Littenberg, T., McWilliams, S. T., Nelemans, G., Petiteau, A., Porter, E. K., Schutz, B. F., Sesana, A., Stebbins, R., Sumner, T., Vallisneri, M., Vitale, S., Volonteri, M., & Ward, H. (2012). Low-frequency gravitational-wave science with eLISA/NGO. Classical and Quantum Gravity, 29(12), 124016.

Antonini, F. & Rasio, F. A. (2016). Merging Black Hole Binaries in Galactic Nuclei: Implications for Advanced-LIGO Detections. ApJ, 831, 187.

Azreg-Aïnou, M. (2016). Vacuum and nonvacuum black holes in a uniform magnetic field. European Physical Journal C, 76, 414.

Bañados, M., Silk, J., & West, S. M. (2009). Kerr Black Holes as Particle Accelerators

to Arbitrarily High Energy. Physical Review Letters, 103(11), 111102.

Babu, A. (2014). Coronal Mass Ejections from the Sun - Propagation and Near Earth Effects. ArXiv e-prints.

Bai, Y., Barger, V., & Lu, S. (2018). Measuring the Black Hole Mass Spectrum from Redshifts of aLIGO Binary Merger Events. ArXiv e-prints.

Begelman, M. C., Volonteri, M., & Rees, M. J. (2006). Formation of supermassive black holes by direct collapse in pre-galactic haloes. Monthly Notices of the Royal Astronomical Society, 370(1), 289–298.

Belczynski, K., Benacquista, M., & Bulik, T. (2010a). Double Compact Objects as Low-frequency Gravitational Wave Sources. ApJ, 725, 816–823.

Belczynski, K., Bulik, T., Fryer, C. L., Ruiter, A., Valsecchi, F., Vink, J. S., & Hurley, J. R. (2010b). On the Maximum Mass of Stellar Black Holes. ApJ, 714, 1217–1226.

Belczynski, K., Dominik, M., Bulik, T., O'Shaughnessy, R., Fryer, C., & Holz, D. E. (2010c). The Effect of Metallicity on the Detection Prospects for Gravitational Waves. ApJ, 715, L138–L141.

Belczynski, K., Heger, A., Gladysz, W., Ruiter, A. J., Woosley, S., Wiktorowicz, G., Chen, H.-Y., Bulik, T., O'Shaughnessy, R., Holz, D. E., Fryer, C. L., & Berti, E. (2016a). The effect of pair-instability mass loss on black-hole mergers. A&A, 594, A97.

Belczynski, K., Holz, D. E., Bulik, T., & O'Shaughnessy, R. (2016b). The first gravitational-wave source from the isolated evolution of two stars in the 40-100 solar mass range. Nat, 534, 512–515.

Belczynski, K., Wiktorowicz, G., Fryer, C. L., Holz, D. E., & Kalogera, V. (2012). Missing Black Holes Unveil the Supernova Explosion Mechanism. ApJ, 757, 91.

Bird, S., Harris, W. E., Blakeslee, J. P., & Flynn, C. (2010). The inner halo of M 87: a first direct view of the red-giant population. A&A, 524, A71.

Blandford, R. D. & Znajek, R. L. (1977). Electromagnetic extraction of energy from Kerr black holes. MNRAS, 179, 433–456.

Bondi, H. & Hoyle, F. (1944). On the mechanism of accretion by stars. MNRAS, 104, 273.

Bower, G. C., Deller, A., Demorest, P., Brunthaler, A., Eatough, R., Falcke, H., Kramer, M., Lee, K. J., & Spitler, L. (2014a). The Angular Broadening of the Galactic Center Pulsar SGR J1745-29: A New Constraint on the Scattering Medium. ApJ, 780, L2.

Bower, G. C., Markoff, S., Brunthaler, A., Law, C., Falcke, H., Maitra, D., Clavel, M., Goldwurm, A., Morris, M. R., Witzel, G., Meyer, L., & Ghez, A. M. (2014b). The Intrinsic Two-dimensional Size of Sagittarius A*. ApJ, 790, 1.

Broderick, A. E. & Loeb, A. (2005). Imaging bright-spots in the accretion flow near the black hole horizon of Sgr A*. MNRAS, 363, 353–362.

Bromm, V. & Loeb, A. (2003). Formation of the First Supermassive Black Holes. ApJ, 596, 34–46.

Brumberg, V. A. (1987). Kinematics and Physics of Celestial Bodies, volume 3.

Butterworth, E. M. & Ipser, J. R. (1975). Rapidly rotating fluid bodies in general relativity. ApJ, 200, L103–L106.

Capellupo, D. M., Haggard, D., Choux, N., Baganoff, F., Bower, G. C., Cotton, B., Degenaar, N., Dexter, J., Falcke, H., Fragile, P. C., Heinke, C. O., Law, C. J., Markoff, S., Neilsen, J., Ponti, G., Rea, N., & Yusef-Zadeh, F. (2017). Simultaneous Monitoring of X-Ray and Radio Variability in Sagittarius A*. ApJ, 845, 35.

Carroll, S. M. (2004). Spacetime and geometry. An introduction to general relativity.

Carter, B. (1968). Global Structure of the Kerr Family of Gravitational Fields. Physical Review, 174, 1559–1571.

Carter, B. (1971). Axisymmetric Black Hole Has Only Two Degrees of Freedom. Physical Review Letters, 26, 331–333.

Chabrier, G. (2003). Galactic Stellar and Substellar Initial Mass Function. PASP, 115, 763–795.

Champion, D. J., Lorimer, D. R., McLaughlin, M. A., Xilouris, K. M., Arzoumanian, Z., Freire, P. C. C., Lommen, A. N., Cordes, J. M., & Camilo, F. (2005). Arecibo timing and single-pulse observations of 17 pulsars. MNRAS, 363, 929–936.

Chanamé, J. & Gould, A. (2002). Millisecond Pulsars as Probes of Mass Segregation in the Galactic Center. ApJ, 571, 320–325.

Chandrasekhar, S. (1983). The mathematical theory of black holes.

Chatterjee, S., Brisken, W. F., Vlemmings, W. H. T., Goss, W. M., Lazio, T. J. W., Cordes, J. M., Thorsett, S. E., Fomalont, E. B., Lyne, A. G., & Kramer, M. (2009). Precision Astrometry with the Very Long Baseline Array: Parallaxes and Proper Motions for 14 Pulsars. ApJ, 698, 250–265.

Chen, X., Madau, P., Sesana, A., & Liu, F. K. (2009). Enhanced Tidal Disruption Rates from Massive Black Hole Binaries. ApJ, 697, L149–L152.

Chennamangalam, J. & Lorimer, D. R. (2014). The Galactic Centre pulsar population. MNRAS, 440, L86–L90.

Chou, Y. & Grindlay, J. E. (2001). Binary and Long-Term (Triple?) Modulations of 4U 1820-30 in NGC 6624. ApJ, 563, 934–940.

Christian, P. & Loeb, A. (2015). Pulsar Timing Constraints on Cumulative and Individual Mass of Stars in the Galactic Center. ApJ, 798, 78.

Christian, P., Psaltis, D., & Loeb, A. (2015). Shapiro Delays at the Quadrupole Order for Tests of the No-Hair Theorem Using Pulsars around Spinning Black Holes. ArXiv e-prints.

Ciufolini, I., Kopeikin, S., Mashhoon, B., & Ricci, F. (2003). On the gravitomagnetic time delay. Physics Letters A, 308, 101–109.

Corbet, R. H. D. & Krimm, H. A. (2013). Superorbital Periodic Modulation in Wind-accretion High-mass X-Ray Binaries from Swift Burst Alert Telescope Observations. ApJ, 778, 45.

Cordes, J. M., Kramer, M., Lazio, T. J. W., Stappers, B. W., Backer, D. C., & Johnston, S. (2004). Pulsars as tools for fundamental physics and astrophysics. New Astronomy Reviews, 48, 1413–1438.

Cordes, J. M. & Lazio, T. J. W. (2002). NE2001.I. A New Model for the Galactic Distribution of Free Electrons and its Fluctuations. ArXiv Astrophysics e-prints.

Cordes, J. M. & Lazio, T. J. W. (2003). NE2001. II. Using Radio Propagation Data to Construct a Model for the Galactic Distribution of Free Electrons. ArXiv Astrophysics e-prints.

Cutler, C. & Flanagan, É. E. (1994). Gravitational waves from merging compact binaries: How accurately can one extract the binary's parameters from the inspiral waveform? Phys. Rev. D, 49, 2658–2697.

Davis, S. W., Done, C., & Blaes, O. M. (2006). Testing Accretion Disk Theory in Black Hole X-Ray Binaries. ApJ, 647, 525–538.

de Gouveia dal Pino, E. M. & Lazarian, A. (2005). Production of the large scale superluminal ejections of the microquasar GRS 1915+105 by violent magnetic reconnection. A&A, 441, 845–853.

de Mink, S. E. & Mandel, I. (2016). The chemically homogeneous evolutionary channel for binary black hole mergers: rates and properties of gravitational-wave events detectable by advanced LIGO. MNRAS, 460, 3545–3553.

Dexter, J. & Agol, E. (2009). A Fast New Public Code for Computing Photon Orbits in a Kerr Spacetime. ApJ, 696, 1616–1629.

Dexter, J. & O'Leary, R. M. (2014). The Peculiar Pulsar Population of the Central Parsec. ApJ, 783, L7.

Doeleman, S. S., Fish, V. L., Schenck, D. E., Beaudoin, C., Blundell, R., Bower, G. C., Broderick, A. E., Chamberlin, R., Freund, R., Friberg, P., Gurwell, M. A., Ho, P. T. P., Honma, M., Inoue, M., Krichbaum, T. P., Lamb, J., Loeb, A., Lonsdale, C., Marrone, D. P., Moran, J. M., Oyama, T., Plambeck, R., Primiani, R. A., Rogers, A. E. E., Smythe, D. L., SooHoo, J., Strittmatter, P., Tilanus, R. P. J., Titus, M., Weintroub, J., Wright, M., Young, K. H., & Ziurys, L. M. (2012). Jet-Launching Structure Resolved Near the Supermassive Black Hole in M87. Science, 338, 355.

Dominik, M., Berti, E., O'Shaughnessy, R., Mandel, I., Belczynski, K., Fryer, C., Holz, D. E., Bulik, T., & Pannarale, F. (2015). Double Compact Objects III: Gravitational-wave Detection Rates. ApJ, 806, 263.

D'Orazio, D. J., Haiman, Z., & Schiminovich, D. (2015). Relativistic boost as the cause of periodicity in a massive black-hole binary candidate. Nat, 525, 351–353.

D'Orazio, D. J. & Levin, J. (2013). Big black hole, little neutron star: Magnetic dipole fields in the Rindler spacetime. Phys. Rev. D, 88(6), 064059.

D'Orazio, D. J., Levin, J., Murray, N. W., & Price, L. (2016). Bright transients from strongly-magnetized neutron star-black hole mergers. Phys. Rev. D, 94(2), 023001.

Du, Y., Yang, J., Campbell, R. M., Janssen, G., Stappers, B., & Chen, D. (2014). Very Long Baseline Interferometry Measured Proper Motion and Parallax of the γ-Ray Millisecond Pulsar PSR J0218+4232. ApJ, 782, L38.

Dyson, F. W., Eddington, A. S., & Davidson, C. (1920). A Determination of the Deflection of Light by the Sun's Gravitational Field, from Observations Made at the Total Eclipse of May 29, 1919. Philosophical Transactions of the Royal Society of London Series A, 220, 291–333.

Eatough, R. P., Falcke, H., Karuppusamy, R., Lee, K. J., Champion, D. J., Keane, E. F., Desvignes, G., Schnitzeler, D. H. F. M., Spitler, L. G., Kramer, M., Klein, B., Bassa, C., Bower, G. C., Brunthaler, A., Cognard, I., Deller, A. T., Demorest, P. B., Freire, P. C. C., Kraus, A., Lyne, A. G., Noutsos, A., Stappers, B., & Wex, N. (2013a). A strong magnetic field around the supermassive black hole at the centre of the Galaxy. Nat, 501, 391–394.

Eatough, R. P., Kramer, M., Klein, B., Karuppusamy, R., Champion, D. J., Freire, P. C. C., Wex, N., & Liu, K. (2013b). Can we see pulsars around Sgr A*? The latest searches with the Effelsberg telescope. In J. van Leeuwen (Ed.), Neutron Stars and Pulsars: Challenges and Opportunities after 80 years, volume 291 of IAU Symposium (pp. 382–384).

Eisenhauer, F., Schödel, R., Genzel, R., Ott, T., Tecza, M., Abuter, R., Eckart, A., & Alexander, T. (2003). A Geometric Determination of the Distance to the Galactic Center. ApJ, 597, L121–L124.

Eisenstein, D. J. & Loeb, A. (1995). Origin of quasar progenitors from the collapse of low-spin cosmological perturbations. ApJ, 443, 11–17.

Farihi, J., Jura, M., & Zuckerman, B. (2009). Infrared Signatures of Disrupted Minor Planets at White Dwarfs. ApJ, 694, 805–819.

Farmer, A. J. & Phinney, E. S. (2003). The gravitational wave background from cosmological compact binaries. MNRAS, 346, 1197–1214.

Farr, W. M., Sravan, N., Cantrell, A., Kreidberg, L., Bailyn, C. D., Mandel, I., & Kalogera, V. (2011). The Mass Distribution of Stellar-mass Black Holes. ApJ, 741, 103.

Farrell, S. A., Sood, R. K., & O'Neill, P. M. (2006). Super-orbital period in the high-mass X-ray binary 2S 0114+650. MNRAS, 367, 1457–1462.

Fishbach, M. & Holz, D. E. (2017). Where Are LIGO's Big Black Holes? ApJ, 851, L25.

Fishbach, M., Holz, D. E., & Farr, B. (2017). Are LIGO's Black Holes Made from Smaller Black Holes? ApJ, 840, L24.

Genzel, R., Eisenhauer, F., & Gillessen, S. (2010). The Galactic Center massive black hole and nuclear star cluster. Reviews of Modern Physics, 82, 3121–3195.

Gerosa, D. & Berti, E. (2017). Are merging black holes born from stellar collapse or previous mergers? Phys. Rev. D, 95(12), 124046.

Ghez, A. M., Salim, S., Weinberg, N. N., Lu, J. R., Do, T., Dunn, J. K., Matthews, K., Morris, M. R., Yelda, S., Becklin, E. E., Kremenek, T., Milosavljevic, M., & Naiman, J. (2008). Measuring Distance and Properties of the Milky Way's Central Supermassive Black Hole with Stellar Orbits. ApJ, 689, 1044–1062.

Giddings, S. B. (2014). Possible observational windows for quantum effects from black holes. Phys. Rev. D, 90(12), 124033.

Gillessen, S. (2014). Observations of the gas cloud G2 in the Galactic Center. In 40th COSPAR Scientific Assembly, volume 40 of COSPAR Meeting.

Gillessen, S., Eisenhauer, F., Trippe, S., Alexander, T., Genzel, R., Martins, F., & Ott, T. (2009). Monitoring Stellar Orbits Around the Massive Black Hole in the Galactic Center. ApJ, 692, 1075–1109.

Glampedakis, K. & Babak, S. (2006). Mapping spacetimes with LISA: inspiral of a test body in a 'quasi-Kerr' field. Classical and Quantum Gravity, 23, 4167–4188.

Gold, R., McKinney, J. C., Johnson, M. D., & Doeleman, S. S. (2017). Probing the Magnetic Field Structure in Sgr A* on Black Hole Horizon Scales with Polarized Radiative Transfer Simulations. ApJ, 837, 180.

Gralla, S. E. & Jacobson, T. (2014). Spacetime approach to force-free magnetospheres. MNRAS, 445, 2500–2534.

Grindlay, J. E., Bailyn, C. D., Cohn, H., Lugger, P. M., Thorstensen, J. R., & Wegner, G. (1988). Discovery of a possible X-ray triple - 4U 1915-05. ApJ, 334, L25–L29.

Haehnelt, M. G. & Rees, M. J. (1993). The formation of nuclei in newly formed galaxies and the evolution of the quasar population. MNRAS, 263, 168–178.

Hannam, M., Schmidt, P., Bohé, A., Haegel, L., Husa, S., Ohme, F., Pratten, G., & Pürrer, M. (2014). Simple Model of Complete Precessing Black-Hole-Binary Gravitational Waveforms. Physical Review Letters, 113(15), 151101.

Hawking, S. W. (1972). Black holes in general relativity. Communications in Mathematical Physics, 25, 152–166.

Hawking, S. W. & Ellis, G. F. R. (1973). The large-scale structure of space-time.

Herrnstein, J. R., Moran, J. M., Greenhill, L. J., & Trotter, A. S. (2005). The Geometry of and Mass Accretion Rate through the Maser Accretion Disk in NGC 4258. ApJ, 629, 719–738.

Hopkins, P. F., Murray, N., Quataert, E., & Thompson, T. A. (2010). A maximum stellar surface density in dense stellar systems. mnras, 401, L19–L23.

Hora, J. L., Witzel, G., Ashby, M. L. N., Becklin, E. E., Carey, S., Fazio, G. G., Ghez, A., Ingalls, J., Meyer, L., Morris, M. R., Smith, H. A., & Willner, S. P. (2014). Spitzer/IRAC Observations of the Variability of Sgr A* and the Object G2 at 4.5 μm. ApJ, 793, 120.

Hoyle, F. & Lyttleton, R. A. (1939). The effect of interstellar matter on climatic variation. Proceedings of the Cambridge Philosophical Society, 35, 405.

Israel, W. (1967). Event Horizons in Static Vacuum Space-Times. Physical Review, 164, 1776–1779.

Israel, W. (1968). Event Horizons in Static Electrovac Space-Times. Communications in Mathematical Physics, 9, 245–260.

Ivanov, P. B., Polnarev, A. G., & Saha, P. (2005). The tidal disruption rate in dense galactic cusps containing a supermassive binary black hole. MNRAS, 358, 1361–1378.

Jaynes, E. T. (2003). Probability Theory: The Logic of Science. CUP.

Johannsen, T. (2012). Testing General Relativity in the Strong-Field Regime with Observations of Black Holes in the Electromagnetic Spectrum. PASP, 124, 1133.

Johannsen, T. (2013). Systematic study of event horizons and pathologies of parametrically deformed kerr spacetimes. Phys. Rev. D, 87, 124017.

Johannsen, T. & Psaltis, D. (2010). Testing the No-hair Theorem with Observations in the Electromagnetic Spectrum. II. Black Hole Images. ApJ, 718, 446–454.

Johannsen, T. & Psaltis, D. (2011). Metric for rapidly spinning black holes suitable for strong-field tests of the no-hair theorem. Phys. Rev. D, 83, 124015.

Johannsen, T. & Psaltis, D. (2013). Testing the No-hair Theorem with Observations in the Electromagnetic Spectrum. IV. Relativistically Broadened Iron Lines. ApJ, 773, 57.

Johnson, M. D., Fish, V. L., Doeleman, S. S., Broderick, A. E., Wardle, J. F. C., & Marrone, D. P. (2014). Relative Astrometry of Compact Flaring Structures in Sgr A* with Polarimetric Very Long Baseline Interferometry. ApJ, 794, 150.

Kaplan, D. L., Chatterjee, S., Gaensler, B. M., & Anderson, J. (2008). A Precise Proper Motion for the Crab Pulsar, and the Difficulty of Testing Spin-Kick Alignment for Young Neutron Stars. ApJ, 677, 1201–1215.

Kaspi, V. M., Archibald, R. F., Bhalerao, V., Dufour, F., Gotthelf, E. V., An, H., Bachetti, M., Beloborodov, A. M., Boggs, S. E., Christensen, F. E., Craig, W. W., Grefenstette, B. W., Hailey, C. J., Harrison, F. A., Kennea, J. A., Kouveliotou, C., Madsen, K. K., Mori, K., Markwardt, C. B., Stern, D., Vogel, J. K., & Zhang, W. W. (2014). Timing and Flux Evolution of the Galactic Center Magnetar SGR J1745-2900. ApJ, 786, 84.

Keck, D. D. & Bortz, D. M. (2013). Numerical simulation of solutions and moments of the smoluchowski coagulation equation. ArXiv e-prints.

Kennea, J. A., Burrows, D. N., Kouveliotou, C., Palmer, D. M., Göğüş, E., Kaneko, Y., Evans, P. A., Degenaar, N., Reynolds, M. T., Miller, J. M., Wijnands, R., Mori, K., & Gehrels, N. (2013). Swift Discovery of a New Soft Gamma Repeater, SGR J1745-29, near Sagittarius A*. ApJ, 770, L24.

Kerr, R. P. (1963). Gravitational Field of a Spinning Mass as an Example of Algebraically Special Metrics. Physical Review Letters, 11, 237–238.

Klioner, S. A. & Kopeikin, S. M. (1992). Microarcsecond astrometry in space - Relativistic effects and reduction of observations. AJ, 104, 897–914.

Koester, D., Gänsicke, B. T., & Farihi, J. (2014). The frequency of planetary debris around young white dwarfs. A&A, 566, A34.

Kopeikin, S., Korobkov, P., & Polnarev, A. (2006). Propagation of light in the field of stationary and radiative gravitational multipoles. Classical and Quantum Gravity, 23, 4299–4322.

Kopeikin, S. M. (1997). Propagation of light in the stationary field of multipole gravitational lens. Journal of Mathematical Physics, 38, 2587–2601.

Kopeikin, S. M. & Makarov, V. V. (2007). Gravitational bending of light by planetary multipoles and its measurement with microarcsecond astronomical interferometers. Phys. Rev. D, 75(6), 062002.

Kopeikin, S. M., Schäfer, G., Gwinn, C. R., & Eubanks, T. M. (1999). Astrometric and timing effects of gravitational waves from localized sources. Phys. Rev. D, 59(8), 084023.

Kramer, M., Backer, D. C., Cordes, J. M., Lazio, T. J. W., Stappers, B. W., & Johnston, S. (2004). Strong-field tests of gravity using pulsars and black holes. New Astronomy Reviews, 48, 993–1002.

Kreidberg, L., Bailyn, C. D., Farr, W. M., & Kalogera, V. (2012). Mass Measurements of Black Holes in X-Ray Transients: Is There a Mass Gap? ApJ, 757, 36.

Kuo, C. Y., Braatz, J. A., Condon, J. J., Impellizzeri, C. M. V., Lo, K. Y., Zaw, I.,

Schenker, M., Henkel, C., Reid, M. J., & Greene, J. E. (2011). The Megamaser Cosmology Project. III. Accurate Masses of Seven Supermassive Black Holes in Active Galaxies with Circumnuclear Megamaser Disks. ApJ, 727, 20.

Lai, D. & Rafikov, R. R. (2005). Effects of Gravitational Lensing in the Double Pulsar System J0737-3039. ApJ, 621, L41–L44.

Lai, K. H., Hannuksela, O. A., Herrera-Martín, A., Diego, J. M., Broadhurst, T., & Li, T. G. F. (2018). Discovering intermediate-mass black hole lenses through gravitational wave lensing. in prep.

Landau, L. D. & Lifshitz, E. M. (1975). The classical theory of fields.

Laughlin, G., Bodenheimer, P., & Adams, F. C. (1997). The End of the Main Sequence. ApJ, 482, 420–432.

Leloudas, G., Fraser, M., Stone, N. C., van Velzen, S., Jonker, P. G., Arcavi, I., Fremling, C., Maund, J. R., Smartt, S. J., Krìhler, T., Miller-Jones, J. C. A., Vreeswijk, P. M., Gal-Yam, A., Mazzali, P. A., De Cia, A., Howell, D. A., Inserra, C., Patat, F., de Ugarte Postigo, A., Yaron, O., Ashall, C., Bar, I., Campbell, H., Chen, T.-W., Childress, M., Elias-Rosa, N., Harmanen, J., Hosseinzadeh, G., Johansson, J., Kangas, T., Kankare, E., Kim, S., Kuncarayakti, H., Lyman, J., Magee, M. R., Maguire, K., Malesani, D., Mattila, S., McCully, C. V., Nicholl, M., Prentice, S., Romero-Cañizales, C., Schulze, S., Smith, K. W., Sollerman, J., Sullivan, M., Tucker, B. E., Valenti, S., Wheeler, J. C., & Young, D. R. (2016). The superluminous transient ASASSN-15lh as a tidal disruption event from a Kerr black hole. Nature Astronomy, 1, 0002.

Levin, Y. & Beloborodov, A. M. (2003). Stellar Disk in the Galactic Center: A Remnant of a Dense Accretion Disk? ApJ, 590, L33–L36.

Li, G., Naoz, S., Kocsis, B., & Loeb, A. (2015). Implications of the eccentric Kozai-Lidov mechanism for stars surrounding supermassive black hole binaries. MNRAS, 451, 1341–1349.

LIGO Collaboration (2016). https://losc.ligo.org/events/GW150914.

LIGO Scientific Collaboration, Aasi, J., Abbott, B. P., Abbott, R., Abbott, T., Abernathy, M. R., Ackley, K., Adams, C., Adams, T., Addesso, P., & et al. (2015). Advanced LIGO. Classical and Quantum Gravity, 32(7), 074001.

Liu, K., Wex, N., Kramer, M., Cordes, J. M., & Lazio, T. J. W. (2012). Prospects for Probing the Spacetime of Sgr A* with Pulsars. ApJ, 747, 1.

Löckmann, U. & Baumgardt, H. (2008). Tracing intermediate-mass black holes in the Galactic Centre. MNRAS, 384, 323–330.

Loeb, A. (2008). 21 cm absorption by compact hydrogen discs around black holes in radio-loud nuclei of galaxies. JCAP, 5, 008.

Loeb, A. (2016). Electromagnetic Counterparts to Black Hole Mergers Detected by LIGO. ApJ, 819, L21.

Loeb, A., Batista, R. A., & Sloan, D. (2016). Relative likelihood for life as a function of cosmic time. JCAP, 8, 040.

Loeb, A. & Rasio, F. A. (1994). Collapse of primordial gas clouds and the formation of quasar black holes. ApJ, 432, 52–61.

Lorimer, D. R. (2008). Binary and Millisecond Pulsars. Living Reviews in Relativity, 11.

Lorimer, D. R. & Kramer, M. (2004). Handbook of Pulsar Astronomy.

Lu, R.-S., Broderick, A. E., Baron, F., Monnier, J. D., Fish, V. L., Doeleman, S. S., & Pankratius, V. (2014). Imaging the Supermassive Black Hole Shadow and Jet Base of M87 with the Event Horizon Telescope. ApJ, 788, 120.

Lupsasca, A., Rodriguez, M. J., & Strominger, A. (2014). Force-free electrodynamics around extreme Kerr black holes. Journal of High Energy Physics, 12, 185.

Lyne, A. G. & Manchester, R. N. (1988). The shape of pulsar radio beams. MNRAS, 234, 477–508.

Maeder, A. (1987). Evidences for a bifurcation in massive star evolution. The ON-blue stragglers. A&A, 178, 159–169.

Manchester, R. N., Hobbs, G. B., Teoh, A., & Hobbs, M. (2005). The Australia Telescope National Facility Pulsar Catalogue. AJ, 129, 1993–2006.

Mandel, I. & de Mink, S. E. (2016). Merging binary black holes formed through chem-

ically homogeneous evolution in short-period stellar binaries. MNRAS, 458, 2634–2647.

Manko, V. S. & Novikov, I. D. (1992). Generalizations of the Kerr and Kerr-Newman metrics possessing an arbitrary set of mass-multipole moments. Classical and Quantum Gravity, 9, 2477–2487.

Masooma, A. (2011). PhD thesis, Bonn University.

Miller, M. C. & Hamilton, R. J. (1993). Reliability of magnetic inclination angle determinations for pulsars. ApJ, 411, 298–301.

Mirabel, I. F. (2003). Microquasars as Sources of High Energy Phenomena. In X. D. Li, V. Trimble, & Z. R. Wang (Eds.), High Energy Processes and Phenomena in Astrophysics, volume 214 of IAU Symposium (pp. 201).

Mirabel, I. F. (2004). Microquasar-AGN-GRB Connections. In V. Schoenfelder, G. Lichti, & C. Winkler (Eds.), 5th INTEGRAL Workshop on the INTEGRAL Universe, volume 552 of ESA Special Publication (pp. 175).

Mirabel, I. F., Rodriguez, L. F., Cordier, B., Paul, J., & Lebrun, F. (1992). A double-sided radio jet from the compact Galactic Centre annihilator 1E1740.7-2942. Nat, 358, 215–217.

Miyoshi, M., Moran, J., Herrnstein, J., Greenhill, L., Nakai, N., Diamond, P., & Inoue, M. (1995). Evidence for a black hole from high rotation velocities in a sub-parsec region of NGC4258. Nat, 373, 127–129.

Montero-Dorta, A. D. & Prada, F. (2009). The SDSS DR6 luminosity functions of galaxies. MNRAS, 399, 1106–1118.

Moran, J. M., Humphreys, E., Greenhill, L., Reid, M., & Argon, A. (2007). The structure of the accretion disk in NGC 4258. In J. M. Chapman & W. A. Baan (Eds.), Astrophysical Masers and their Environments, volume 242 of IAU Symposium (pp. 391–398).

Mori, K., Gotthelf, E. V., Zhang, S., An, H., Baganoff, F. K., Barrière, N. M., Beloborodov, A. M., Boggs, S. E., Christensen, F. E., Craig, W. W., Dufour, F., Grefenstette, B. W., Hailey, C. J., Harrison, F. A., Hong, J., Kaspi, V. M., Kennea, J. A., Madsen, K. K., Markwardt, C. B., Nynka, M., Stern, D., Tomsick,

J. A., & Zhang, W. W. (2013). NuSTAR Discovery of a 3.76 s Transient Magnetar Near Sagittarius A*. ApJ, 770, L23.

Morozova, V. S., Rezzolla, L., & Ahmedov, B. J. (2014). Nonsingular electrodynamics of a rotating black hole moving in an asymptotically uniform magnetic test field. Phys. Rev. D, 89, 104030.

Mouri, H. & Taniguchi, Y. (2002). Runaway Merging of Black Holes: Analytical Constraint on the Timescale. ApJ, 566, L17–L20.

Moylan, A. J., McClelland, D. E., Scott, S. M., Searle, A. C., & Bicknell, G. V. (2008). Numerical Wave Optics and the Lensing of Gravitational Waves by Globular Clusters. In H. Kleinert, R. T. Jantzen, & R. Ruffini (Eds.), The Eleventh Marcel Grossmann Meeting On Recent Developments in Theoretical and Experimental General Relativity, Gravitation and Relativistic Field Theories (pp. 807–823).

Nambu, Y. (2013). Wave Optics and Image Formation in Gravitational Lensing. International Journal of Astronomy and Astrophysics, 3, 1–7.

Nelemans, G., Yungelson, L. R., & Portegies Zwart, S. F. (2001). The gravitational wave signal from the Galactic disk population of binaries containing two compact objects. A&A, 375, 890–898.

Newman, E. T., Couch, E., Chinnapared, K., Exton, A., Prakash, A., & Torrence, R. (1965). Metric of a Rotating, Charged Mass. Journal of Mathematical Physics, 6, 918–919.

Newman, E. T. & Janis, A. I. (1965). Note on the Kerr Spinning-Particle Metric. Journal of Mathematical Physics, 6, 915–917.

O'Leary, R. M., Meiron, Y., & Kocsis, B. (2016). Dynamical Formation Signatures of Black Hole Binaries in the First Detected Mergers by LIGO. ApJ, 824, L12.

O'Leary, R. M., Rasio, F. A., Fregeau, J. M., Ivanova, N., & O'Shaughnessy, R. (2006). Binary Mergers and Growth of Black Holes in Dense Star Clusters. ApJ, 637, 937–951.

Oppenheimer, J. R. & Snyder, H. (1939). On continued gravitational contraction. Phys. Rev., 56, 455–459.

Özel, F., Psaltis, D., Narayan, R., & McClintock, J. E. (2010). The Black Hole Mass Distribution in the Galaxy. ApJ, 725, 1918–1927.

Pappas, G. & Apostolatos, T. A. (2012). Revising the multipole moments of numerical spacetimes and its consequences. Phys. Rev. Lett., 108, 231104.

Penrose, R. (1969). Gravitational Collapse: the Role of General Relativity. Nuovo Cimento Rivista Serie, 1.

Peters, P. C. (1964). Gravitational Radiation and the Motion of Two Point Masses. Physical Review, 136, 1224–1232.

Peters, P. C. (1974). Index of refraction for scalar, electromagnetic, and gravitational waves in weak gravitational fields. Phys. Rev. D, 9, 2207.

Peters, P. C. & Mathews, J. (1963). Gravitational Radiation from Point Masses in a Keplerian Orbit. Physical Review, 131, 435–440.

Pfahl, E. & Loeb, A. (2004). Probing the Spacetime around Sagittarius A* with Radio Pulsars. ApJ, 615, 253–258.

Phinney, E. S. (1993). Pulsars as Probes of Globular Cluster Dynamics. In S. G. Djorgovski & G. Meylan (Eds.), Structure and Dynamics of Globular Clusters, volume 50 of Astronomical Society of the Pacific Conference Series (pp. 141).

Phinney, E. S. & Hansen, B. M. S. (1993). The pulsar planet production process. In J. A. Phillips, S. E. Thorsett, & S. R. Kulkarni (Eds.), Planets Around Pulsars, volume 36 of Astronomical Society of the Pacific Conference Series (pp. 371–390).

Piórkowska, A., Biesiada, M., & Zhu, Z.-H. (2013). Strong gravitational lensing of gravitational waves in Einstein Telescope. JCAP, 10, 022.

Podsiadlowski, P. (1993). Planet formation scenarios. In J. A. Phillips, S. E. Thorsett, & S. R. Kulkarni (Eds.), Planets Around Pulsars, volume 36 of Astronomical Society of the Pacific Conference Series (pp. 149–165).

Poisson, E. (2004). A relativist's toolkit : the mathematics of black-hole mechanics.

Pretorius, F. (2005). Evolution of Binary Black-Hole Spacetimes. Physical Review Letters, 95(12), 121101.

Prodan, S. & Murray, N. (2015). On the Dynamics of Ultra Compact X-Ray Binaries: 4U 1850-087, 4U 0513-40, and M15 X-2. ApJ, 798, 117.

Psaltis, D. & Johannsen, T. (2011). Sgr A*: The Optimal Testbed of Strong-Field Gravity. In Journal of Physics Conference Series, volume 283 of Journal of Physics Conference Series (pp. 012030).

Psaltis, D. & Johannsen, T. (2012). A Ray-tracing Algorithm for Spinning Compact Object Spacetimes with Arbitrary Quadrupole Moments. I. Quasi-Kerr Black Holes. ApJ, 745, 1.

Psaltis, D., Özel, F., Chan, C.-K., & Marrone, D. P. (2015). A General Relativistic Null Hypothesis Test with Event Horizon Telescope Observations of the Black Hole Shadow in Sgr A*. ApJ, 814, 115.

Psaltis, D., Wex, N., & Kramer, M. (2016). A Quantitative Test of the No-hair Theorem with Sgr A* Using Stars, Pulsars, and the Event Horizon Telescope. ApJ, 818, 121.

Punturo, M., Abernathy, M., Acernese, F., Allen, B., Andersson, N., Arun, K., Barone, F., Barr, B., Barsuglia, M., Beker, M., Beveridge, N., Birindelli, S., Bose, S., Bosi, L., Braccini, S., Bradaschia, C., Bulik, T., Calloni, E., Cella, G., Chassande Mottin, E., Chelkowski, S., Chincarini, A., Clark, J., Coccia, E., Colacino, C., Colas, J., Cumming, A., & Cunningham, L. (2010). The Einstein Telescope: a third-generation gravitational wave observatory. Classical and Quantum Gravity, 27(19), 194002.

Rafikov, R. R. & Lai, D. (2006). Effects of gravitational lensing and companion motion on the binary pulsar timing. Phys. Rev. D, 73, 063003.

Raghavan, D., McAlister, H. A., Henry, T. J., Latham, D. W., Marcy, G. W., Mason, B. D., Gies, D. R., White, R. J., & ten Brummelaar, T. A. (2010). A Survey of Stellar Families: Multiplicity of Solar-type Stars. ApJS, 190, 1–42.

Raithel, C. A., Sukhbold, T., & Özel, F. (2017). Confronting Models of Massive Star Evolution and Explosions with Remnant Mass Measurements. ArXiv e-prints.

Rankin, J. M. (1990). Toward an empirical theory of pulsar emission. IV - Geometry of the core emission region. ApJ, 352, 247–257.

Rea, N., Esposito, P., Pons, J. A., Turolla, R., Torres, D. F., Israel, G. L., Possenti, A., Burgay, M., Viganò, D., Papitto, A., Perna, R., Stella, L., Ponti, G., Baganoff, F. K., Haggard, D., Camero-Arranz, A., Zane, S., Minter, A., Mereghetti, S., Tiengo, A., Schödel, R., Feroci, M., Mignani, R., & Götz, D. (2013). A Strongly Magnetized Pulsar within the Grasp of the Milky Way's Supermassive Black Hole. ApJ, 775, L34.

Rees, M. J. (1966). Appearance of Relativistically Expanding Radio Sources. Nat, 211, 468–470.

Reid, M. J., Readhead, A. C. S., Vermeulen, R. C., & Treuhaft, R. N. (1999). The Proper Motion of Sagittarius A*. I. First VLBA Results. ApJ, 524, 816–823.

Richter, G. W. & Matzner, R. A. (1982a). Second-order contributions to gravitational deflection of light in the parametrized post-Newtonian formalism. Phys. Rev. D, 26, 1219–1224.

Richter, G. W. & Matzner, R. A. (1982b). Second-order contributions to gravitational deflection of light in the parametrized post-Newtonian formalism. II. Photon orbits and deflections in three dimensions. Phys. Rev. D, 26, 2549–2556.

Richter, G. W. & Matzner, R. A. (1983). Second-order contributions to relativistic time delay in the parametrized post-Newtonian formalism. Phys. Rev. D, 28, 3007–3012.

Robinson, D. C. (1975). Uniqueness of the kerr black hole. Phys. Rev. Lett., 34, 905–906.

Rodriguez, C. L., Amaro-Seoane, P., Chatterjee, S., & Rasio, F. A. (2017). Post-Newtonian Dynamics in Dense Star Clusters: Highly-Eccentric, Highly-Spinning, and Repeated Binary Black Hole Mergers. ArXiv e-prints.

Rodriguez, C. L., Chatterjee, S., & Rasio, F. A. (2016a). Binary black hole mergers from globular clusters: Masses, merger rates, and the impact of stellar evolution. Phys. Rev. D, 93(8), 084029.

Rodriguez, C. L., Haster, C.-J., Chatterjee, S., Kalogera, V., & Rasio, F. A. (2016b). Dynamical Formation of the GW150914 Binary Black Hole. ApJ, 824, L8.

Rodriguez, C. L., Morscher, M., Pattabiraman, B., Chatterjee, S., Haster, C.-J., & Ra-

sio, F. A. (2015). Binary Black Hole Mergers from Globular Clusters: Implications for Advanced LIGO. Physical Review Letters, 115(5), 051101.

Salaris, M. & Cassisi, S. (2006). Evolution of Stars and Stellar Populations.

Salpeter, E. E. (1955). The Luminosity Function and Stellar Evolution. ApJ, 121, 161.

Samsing, J., D'Orazio, D. J., Askar, A., & Giersz, M. (2018). Black Hole Mergers from Globular Clusters Observable by LISA and LIGO: Results from post-Newtonian Binary-Single Scatterings. ArXiv e-prints.

Sana, H., de Mink, S. E., de Koter, A., Langer, N., Evans, C. J., Gieles, M., Gosset, E., Izzard, R. G., Le Bouquin, J.-B., & Schneider, F. R. N. (2012). Binary Interaction Dominates the Evolution of Massive Stars. Science, 337, 444.

Savani, N. P., Davies, J. A., Davis, C. J., Shiota, D., Rouillard, A. P., Owens, M. J., Kusano, K., Bothmer, V., Bamford, S. P., Lintott, C. J., & Smith, A. (2012). Observational Tracking of the 2D Structure of Coronal Mass Ejections Between the Sun and 1 AU. Solar Physics, 279, 517–535.

Schwarzschild, K. (1916). Über das Gravitationsfeld einer Kugel aus inkompressibler Flüssigkeit nach der Einsteinschen Theorie. In Sitzungsberichte der Königlich Preussischen Akademie der Wissenschaften zu Berlin, Phys.-Math. Klasse, 424-434 (1916).

Sereno, M., Sesana, A., Bleuler, A., Jetzer, P., Volonteri, M., & Begelman, M. C. (2010). Strong Lensing of Gravitational Waves as Seen by LISA. Physical Review Letters, 105(25), 251101.

Seto, N. (2016). Prospects of eLISA for detecting Galactic binary black holes similar to GW150914. MNRAS, 460, L1–L4.

Shakura, N. I. & Sunyaev, R. A. (1973). Black holes in binary systems. Observational appearance. A&A, 24, 337–355.

Shannon, R. M. & Johnston, S. (2013). Radio properties of the magnetar near Sagittarius A* from observations with the Australia Telescope Compact Array. MNRAS, 435, L29–L32.

Shapiro, I. I. (1964). Fourth Test of General Relativity. Physical Review Letters, 13, 789–791.

Sigurdsson, S. & Hernquist, L. (1993). Primordial black holes in globular clusters. Nat, 364, 423–425.

Smoluchowski, M. (1916). Drei Vortr ge ber Diffusion, Brownsche Molekularbewegung und Koagulation von Kolloidteilchen. Physik. Z., 17, 557–571.

Sobolewska, M. A., Siemiginowska, A., & Gierliński, M. (2011). Simulated spectral states of active galactic nuclei and observational predictions. MNRAS, 413, 2259–2268.

Sukhbold, T., Ertl, T., Woosley, S. E., Brown, J. M., & Janka, H.-T. (2016). Core-collapse Supernovae from 9 to 120 Solar Masses Based on Neutrino-powered Explosions. ApJ, 821, 38.

Takahashi, R. & Nakamura, T. (2003). Wave Effects in the Gravitational Lensing of Gravitational Waves from Chirping Binaries. ApJ, 595, 1039–1051.

Taylor, J. H., Manchester, R. N., & Lyne, A. G. (1993). Catalog of 558 pulsars. ApJS, 88, 529–568.

Team, T. E. T. S. (2011). ET design study document. The Einstein Telescope Science Team, ET design study document.

Teyssandier, P. (2014). New tools for determining the light travel time in static, spherically symmetric spacetimes beyond the order G^2. ArXiv e-prints.

Teyssandier, P. & Le Poncin-Lafitte, C. (2008). General post-Minkowskian expansion of time transfer functions. Classical and Quantum Gravity, 25(14), 145020.

Thorsett, S. E., Arzoumanian, Z., Camilo, F., & Lyne, A. G. (1999). The Triple Pulsar System PSR B1620-26 in M4. ApJ, 523, 763–770.

Tokovinin, A. (2014). From Binaries to Multiples. II. Hierarchical Multiplicity of F and G Dwarfs. AJ, 147, 87.

Ulmer, A. (1998). The tidal disruption of stars by massive black holes. In S. S. Holt & T. R. Kallman (Eds.), American Institute of Physics Conference Series, volume

431 of American Institute of Physics Conference Series (pp. 141–144).

Umemura, M., Loeb, A., & Turner, E. L. (1993). Early Cosmic Formation of Massive Black Holes. ApJ, 419, 459.

Vanderburg, A., Johnson, J. A., Rappaport, S., Bieryla, A., Irwin, J., Lewis, J. A., Kipping, D., Brown, W. R., Dufour, P., Ciardi, D. R., Angus, R., Schaefer, L., Latham, D. W., Charbonneau, D., Beichman, C., Eastman, J., McCrady, N., Wittenmyer, R. A., & Wright, J. T. (2015). A disintegrating minor planet transiting a white dwarf. Nat, 526, 546–549.

Veitch, J., Raymond, V., Farr, B., Farr, W., Graff, P., Vitale, S., et al. (2015). Parameter estimation for compact binaries with ground-based gravitational-wave observations using the LALInference software library. Phys. Rev. D, 91(4), 042003.

Verbiest, J. P. W., Bailes, M., van Straten, W., Hobbs, G. B., Edwards, R. T., Manchester, R. N., Bhat, N. D. R., Sarkissian, J. M., Jacoby, B. A., & Kulkarni, S. R. (2008). Precision Timing of PSR J0437-4715: An Accurate Pulsar Distance, a High Pulsar Mass, and a Limit on the Variation of Newton's Gravitational Constant. ApJ, 679, 675–680.

Vitale, S. (2016). Three observational differences for binary black holes detections with second- and third-generation gravitational-wave detectors. Phys. Rev. D, 94(12), 121501.

Vitale, S. & Evans, M. (2017). Parameter estimation for binary black holes with networks of third-generation gravitational-wave detectors. Phys. Rev. D, 95(6), 064052.

Wald, R. M. (1974). Black hole in a uniform magnetic field. Phys. Rev. D, 10, 1680–1685.

Walsh, J. L., Barth, A. J., Ho, L. C., & Sarzi, M. (2013). The M87 Black Hole Mass from Gas-dynamical Models of Space Telescope Imaging Spectrograph Observations. ApJ, 770, 86.

Wex, N. & Kopeikin, S. M. (1999). Frame Dragging and Other Precessional Effects in Black Hole Pulsar Binaries. ApJ, 514, 388–401.

Wharton, R. S., Chatterjee, S., Cordes, J. M., Deneva, J. S., & Lazio, T. J. W. (2012).

Multiwavelength Constraints on Pulsar Populations in the Galactic Center. ApJ, 753, 108.

Wolszczan, A. & Frail, D. A. (1992). A planetary system around the millisecond pulsar PSR1257 + 12. Nat, 355, 145–147.

Woosley, S. E. (2017). Pulsational Pair-instability Supernovae. ApJ, 836, 244.

Yuan, F., Lin, J., Wu, K., & Ho, L. C. (2009). A magnetohydrodynamical model for the formation of episodic jets. MNRAS, 395, 2183–2188.

Yuan, F. & Narayan, R. (2014). Hot Accretion Flows Around Black Holes. ARA&A, 52, 529–588.

Yusef-Zadeh, F., Roberts, D., Wardle, M., Heinke, C. O., & Bower, G. C. (2006). Flaring Activity of Sagittarius A* at 43 and 22 GHz: Evidence for Expanding Hot Plasma. ApJ, 650, 189–194.

Yusef-Zadeh, F. & Wardle, M. (2012). The Origin of Parsec-Scale Gaseous and Stellar Disks in the Galactic Center and AGNs. In Journal of Physics Conference Series, volume 372 of Journal of Physics Conference Series (pp. 012024).

Zdziarski, A. A., Wen, L., & Gierliński, M. (2007). The superorbital variability and triple nature of the X-ray source 4U 1820-303. MNRAS, 377, 1006–1016.

Zschocke, S. & Klioner, S. A. (2009). Analytical solution for light propagation in Schwarzschild field having an accuracy of 1 micro-arcsecond. ArXiv e-prints.

Zuckerman, B., Melis, C., Klein, B., Koester, D., & Jura, M. (2010). Ancient Planetary Systems are Orbiting a Large Fraction of White Dwarf Stars. ApJ, 722, 725–736.